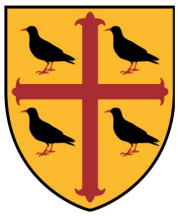


Graphene Nanogaps and Nanoelectronic Devices

John. J. Cully

St. Edmund Hall



University of Oxford

A thesis presented for the degree of
Doctor of Philosophy

October 2021

Abstract

Electronic devices based on single-molecules or single-nanoparticles offer the potential for highly energy-efficient devices with chemically tunable properties for applications in computing, sensing and memory storage. However, numerous challenges pose barriers to the realisation of robust, reproducible and scalable single particle devices: in particular, the fabrication of electrodes of suitable dimensions to contact these particles and the challenge of manipulating the target particles into desired positions. This thesis explores the creation of graphene nanogap electrodes as a platform for single-particle devices and some of the unique properties associated with single-molecule devices. It then goes on to detail efforts to improve the yield of nanogap fabrication and to develop a method based on the phenomenon of dielectrophoresis to manipulate nanoscale particles. Finally, it examines the low-temperature transport physics of hybrid graphene-nanoparticle devices created using the dielectrophoretic method. This thesis highlights key challenges in the creation of single-molecule devices, examines methods to better control the formation of such devices and demonstrates a route towards the creation of a plethora of novel, hybrid devices formed from unique nanomaterials coupled to graphene electrodes with diverse potential applications.

To all my friends, my family and to Katie. This thesis would have not been possible without your friendship, support and love.

All the work in this thesis is original and has not been submitted in support of an application for another degree or qualification, at either this university or any other institute of learning. Total word count ≈ 40,000.

Covid-19 impact statement

The pandemic had considerable impact on my doctoral work, occuring half way through my third year and impacting the remainder of my project. The experimental work in chapters 1, 2 and much of chapter 3 of this thesis was completed prior to the pandemic, while the analysis in chapter 4 was achieved during the lockdown and the experimental work in chapter 5 and §3.3.3 of chapter 3 were undertaken once laboratory access was regained. My laboratory space was closed from 03/2020 - 08/2020, opening with a reduced capacity thereafter, which limited my ability to respond to developments during fabrication and experimental work. The pandemic meant that the collaborative work I was involved in at Imperial College London was no longer viable and I was forced to develop a contingency plan for the remainder of my project which I could run entirely independently. The resulting work constitutes chapter 5. With an original hand-in date of 07/2021 I applied for some extension funding to make up for lost time, however I was not informed of the outcome until 05/2021, at which point I was wrapping up my experimental work. I had hoped to be able to spend more time on the dielectrophoretic trapping of molecules, linking back to the work I did at the beginning of my project, however my collaborators who were synthesising the larger target molecules were also impacted by the pandemic and they were not ready until 06/2021. The three month extension allowed me to take 3 weeks out of my write-up to go back to the lab, but this was unfortunately only enough time to gather some preliminary data. The experimental time I lost to the pandemic exacerbated the impact of an unforeseen movement of our laboratory, associated equipment maintenance and building maintenance which all occurred in early 2021, costing me about a further 2 months of experimental time. Overall, the pandemic had a significant and sustained impact on my ability to carry out my experimental work and restricted the directions in which I could take it.

Contents

Thesis aims and outline **1**

Publications **2**

1 Molecular Electronics **3**
1.1 Introduction . . . 3
1.1.1 Experimental techniques . . . 4
1.1.1.1 Scanning probe microscopy . . . 5
1.1.1.2 Electromigration . . . 7
1.1.1.3 Mechanically controlled break junctions . . . 9
1.1.1.4 Low dimensional carbon devices . . . 11
1.1.2 Theoretical Framework . . . 14
1.1.2.1 Tunnel junctions: the Simmons model . . . 14
1.1.2.2 Single-level model . . . 16
1.1.2.3 Fano resonance . . . 19
1.1.3 Anthraquinone . . . 19
1.1.3.1 Conjugation dependence . . . 20
1.1.3.2 Interference effects . . . 20
1.1.3.3 Connectivity dependence . . . 23
1.2 Methods . . . 24
1.2.1 Graphene transfer . . . 25
1.2.2 Graphene patterning . . . 25
1.2.3 Electroburning . . . 26
1.2.4 Characterisation . . . 27
1.3 Results . . . 29
1.4 Conclusion . . . 34

2 Electroburning **36**
2.1 Introduction . . . 36
2.1.1 Mechanism . . . 37
2.2 Evolution during electroburning . . . 38
2.2.1 Electroburning under different atmospheres . . . 42
2.2.1.1 Switching . . . 44
2.3 Conclusion . . . 48

3 Dielectrophoresis **50**
3.1 Introduction . . . 50
3.1.1 Theory . . . 51
3.1.2 Device design . . . 52
3.2 Modelling . . . 53
3.3 Experimental . . . 56
3.3.1 Latex beads and DNA . . . 56
3.3.2 Gold nanoparticles . . . 58
3.3.3 Molecules . . . 61
3.4 Conclusion . . . 64

4 Gold nanoparticles **66**
4.1 Introduction . . . 66
4.1.1 Gold nanoparticle devices . . . 67
4.1.2 Transport physics . . . 67
4.1.2.1 Two terminal devices . . . 68
4.1.2.2 Three terminal devices . . . 70
4.2 Device preparation . . . 72
4.2.1 Fabrication . . . 72
4.2.2 Deposition . . . 73
4.2.3 Characterisation . . . 73
4.2.4 Annealing . . . 74
4.2.5 Measurement . . . 75
4.3 Results . . . 75
4.4 Discussion . . . 81
4.4.1 Limitations . . . 82
4.5 Conclusion . . . 82

5 Magnetite nanocrystals **84**
5.1 Introduction . . . 84
5.1.1 Formal Structure . . . 85
5.1.2 The Verwey Model . . . 85
5.1.3 Crystal Structure . . . 86
5.1.4 Electronic Spectrum: Theoretical Descriptions . . . 87
5.1.4.1 Mott . . . 87
5.1.4.2 Ihle and Lorenz . . . 87
5.1.4.3 Limitations . . . 88
5.1.4.4 Computational work . . . 88
5.1.5 Electronic Spectrum: Experimental . . . 89
5.1.5.1 Optical Conductivity . . . 89
5.1.5.2 Photo-Emission Spectroscopy . . . 90
5.1.5.3 X-ray Scattering . . . 91
5.1.5.4 Tunnelling Spectroscopy . . . 92
5.1.6 Summary . . . 96
5.2 Methods . . . 96
5.2.1 Nanoparticle selection . . . 96
5.2.2 Dielectrophoresis . . . 97
5.2.3 Annealing . . . 99
5.3 Results and Discussion . . . 100
5.3.1 IV behaviour . . . 100
5.3.2 Gate Dependence . . . 103
5.3.3 IV comparison . . . 105
5.3.4 Magnetic Field Dependence . . . 105
5.3.5 Temperature Dependence . . . 108
5.4 Conclusion . . . 112

Conclusions and outlook **114**

Acknowledgements **115**

Appendices **115**
I Chip designs . . . 116
II PCBs . . . 117
III Orthodox model . . . 118

Bibliography **119**

Thesis aims and outline

This thesis charts the course of a project I began in October 2017 in the group of Dr. J.A. Mol, co-supervised by Prof. G.A.D. Briggs, within the Department of Materials at the University of Oxford. The groups' work centred on the platform of graphene 'nanogaps', two graphene electrodes separated by only a few nanometres which are created via feedback-controlled electrical breakdown, for use in molecular electronics and bio-sensing applications. My role was to continue the investigation of the electronic transport physics in single-molecule devices, formed by bridging target molecules across the graphene nanogaps. Specifically, I was to investigate ways to improve the fabrication of these devices, explore how quantum interference effects may manifest within the transport and to catalogue the conditions, molecular and electrostatic, under which they could be observed. Molecules have well defined conduction pathways, are small and are inherently chemically tunable. The creation of robust and reproducible molecular devices could offer a promising compliment to silicon-based computing, memory and sensing technologies.

I began by exploring a molecule based on an anthraquinone core, an analogue of which had previously been observed to show charge-state dependent quantum interference and was predicted to further show connectivity-dependent transport resonances. In Chapter 1, I first give an in-depth review of common methods used to fabricate nanogap devices, before moving on to discuss literature relating to transport in anthraquinone-based single-molecule devices and presenting the experimental work I undertook towards observing interference phenomena. This work revealed some significant challenges associated with creating molecular devices using graphene nanogaps, namely the low yield of suitable nanogap junctions and the further low yield of bridging the nanogaps with molecules to form molecular devices. This motivated me to attempt to address these challenges before continuing with further molecular experiments. Chapter 2 describes my efforts to improve nanogap yields by studying the electrical breakdown process and exploring the impact of changing the atmosphere under which breakdown is performed. While this work helped improve our understanding of the breakdown mechanism it did not directly lead to an improvement of the yield of nanogap junctions. Chapter 3 moves on to look at how the technique of dielectrophoresis can be applied to our nanogap platform to control the bridging of nanogaps by target particles. I explore the trapping of a variety of nanoparticles and molecules and optimise the trapping parameters for single gold nanoparticles. I discuss the limitations of the technique but also show tantalising evidence for its use in the controlled assem-

bly of molecular devices. Building on Chapter 3, Chapter 4 details the characterisation and understanding of charge transport through gold nanoparticle devices assembled using dielectrophoresis, exhibiting the potential to form hybrid graphene-nanoparticle devices from an array of synthesised nanomaterials. Finally, Chapter 5 explores one such nanomaterial, magnetite nanocrystals, and documents the creation and study of charge transport in devices formed from single or few nanoparticles. I detail my observations of a large transport gap and a temperature-driven phase transition, adding to the growing body of work directed at understanding the transport physics of this, and other, highly-correlated materials.

In summary, this thesis maps my journey from single-molecule to single-nanoparticle electronic devices, exploring various properties and challenges of such devices, with a particular focus on the use of dielectrophoresis to control the formation of novel, hybrid nanoscale devices.

Publications

Chapters 3 and 4 of this thesis are in part based on the published work (1):

- Cully, J. J., Swett, J. L., Willick, K., Baugh, J. & Mol, J. A. *Graphene nanogaps for the directed assembly of single-nanoparticle devices. Nanoscale* **13**, 6513–6520 (2021).

Chapter 1

Molecular Electronics

Overview

In this chapter I will discuss the motivation for and results of the experiments I conducted on molecular electronics, with the specific goal of observing and characterising quantum interference effects in the charge transport properties of anthraquinone-based single-molecule devices. This chapter begins with a review of the techniques used for creating nanogap electrodes suitable for the study of single-molecule electronics, outlining of some of the most significant developments in the field. I will briefly introduce the theoretical models used to describe charge transport through single-molecules, focussing on those most relevant to anthraquinone-based molecules. I will discuss prior experimental and theoretical studies of anthraquinone-based molecular devices to place our work in context. Finally, I will describe the experiments we conducted and present the results of those experiments followed by a discussion of the challenges faced in this research.

1.1 Introduction

Molecular electronics offers the possibility to explore the fundamentals of charge transport at the smallest possible scale. The well-defined conduction pathways in and size of molecules mean that they promise an attractive complement to current CMOS-based technology, which is reaching its limit of miniaturisation. Furthermore, chemical modifications can be used to engineer the electronic structure of molecules, with the possibility of creating highly non-linear transport properties which are desirable for realising a range of functionalities such as rectification and switching (2, 3). These applications, and the desire to understand the underlying physics, have driven the research into single-molecule electronics over the last few decades (4).

Perhaps the first study to report on the electrical transport properties of molecules was performed by Mann *et al.* in 1971 (5). In this paper, the authors prepared a self-assembled monolayer (SAM) of fatty acids

on an aluminium electrode, and made use of a mercury droplet to create a top electrode. Using several SAMs made of fatty acids with different carbon chain lengths, the authors were able to show an exponential relation between between the conductivity of the SAM and the length of the carbon chains. This method offered a powerful technique for probing the properties of thin films and SAMs (6), however, in order to achieve measurement of the current through *single*-molecules it became necessary to first develop methods to produce electrodes separated by gaps of only a few nanometres between which molecules could be inserted - nanogaps. Much of the work in the field so far has been directed towards the production of such devices, with many methods developed using a variety of techniques and materials (7). As such, here I will briefly review the range of methods used to produce them in order to set the context for the rest of this thesis. I will then go on to briefly cover the transport physics and literature relevant to the particular molecule studied in later in this chapter: anthraquinone.

1.1.1 Experimental techniques

An ideal device would:

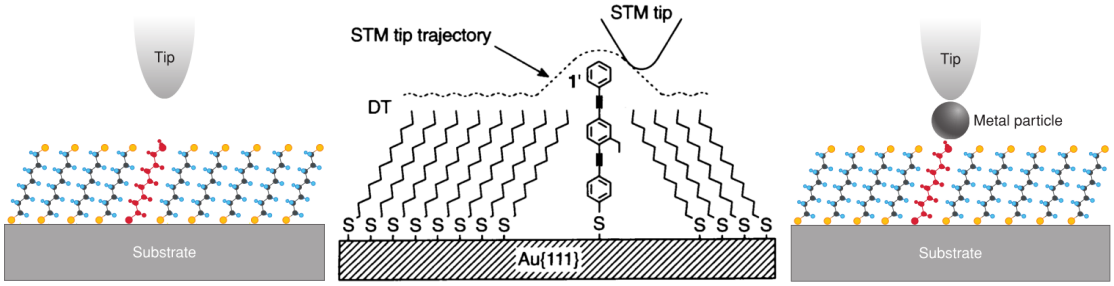
- Be easy to fabricate,
- be highly reproducible,
- be mechanically stable across a broad temperature range,
- have atomically defined electrodes with a controllable gap size,
- be clean and free from contaminants,
- be resilient to strong electric and magnetic fields used for measurements,
- have scalable fabrication for future applications,
- have metallic contacts with high conductivity,
- cause minimal screening of any electrostatic gate, and,
- have a chemistry which allows tunable coupling to target molecules.

Unfortunately, despite the decades of research and a vast array of methods devoted to produce such junctions (8), no one method has yet been found that meets all of these criteria. The next subsections will review three of the most popular methods, developed in the 1980s and 90s, which each match some of these criteria and which still underpin much of the work in the field to this day (9). These techniques all share the use of noble metals, typically gold (10), as the electrode materials due to its ductility, high conductivity and wide chemical inertness. Molecules can be easily connected to the electrodes by exploiting golds' specific affinity

for thiol- or amine-linker groups to form stable chemical bonds (4, 11). Later, in §1.1.1.4 some more contemporary methods, including the method used in this thesis, that utilise low-dimensional carbon electrodes will be discussed.

1.1.1.1 Scanning probe microscopy

The advent of scanning probe microscopy (SPM) techniques such as scanning tunnelling microscopy (STM) and conductive-tip atomic force microscopy (CT-AFM) offered a controlled and highly sensitive methodology to measure the tunnelling current that flows between a given substrate and a nanometre-sized tip under bias. By monitoring the tunnelling current, the separation between tip and surface can be highly tuned.



(a) (b) (c)

Figure 1.1: (a) A schematic showing an STM study of the conductivity of a SAM. Reproduced from (12). (b) An insulating sub-monolayer matrix prepared on a Au(111) substrate, with the molecule of interest inserted into gaps within the matrix and extending above it so that the STM tip can probe the molecule directly without probing the surrounding molecules. Reproduced from (13). (c) An STM or CT-AFM study of molecular conductivity using a nano-particle as a local electrode. Reproduced from (12).

STM was first used to investigate the rectifying behaviour of an oligo-phenylethynyl SAM on a conductive Au substrate (14). As the tip was lowered towards the surface, a sudden increase in the tunnel current was observed when the tip interacted with the SAM (15). Molecules may be better isolated by embedding them into a sub-monolayer coverage of a second short, insulating molecule, as shown in Figure 1.1b. The tip can then access small numbers of target molecules which are supported by the sub-monolayer which has minimal impact on the electrical properties of the target molecule (13). Typically, the interactions between a surface-bound molecule and an STM tip are much weaker van der Waals interactions than those between the chemically bonded molecule and substrate (16) which results in strongly asymmetric junctions and weak molecule-electrode coupling. Stronger coupling may be achieved by depositing a small number of metal nanoparticles on top of the SAM which may chemically bond to the molecules below using the same chemistry that binds the molecule to the substrate, as shown in Figure 1.1c. The tip can then be used to tunnel electrons onto the nanoparticle which then flow through the molecule to the substrate under the applied bias (17, 18), and the transport between the tip and the substrate can be de-convoluted to find the conductance of the molecule (12). Reproducibility can be further improved by using CT-AFM to directly contact the nanoparticle, thereby removing the tip-nanoparticle tunnel junction and offering a much stronger signal

(19). Additionally, unlike in STM, for CT-AFM the positioning of the tip is controlled by the force, not the current, allowing for the sample to be contacted prior to any electrical measurements resulting in a more stable electrical contact (20).

These methods, however, do not truly address *single*-molecules as control over the number of molecules between the tip and the substrate remains challenging (21). Furthermore, it is likely that interactions between neighbouring molecules have a strong impact on the transport properties of both the molecules and the tip (22). SAM-based studies remain a good option for long molecules with low conductivities, but the convolution between small topographical features and molecular signals makes results difficult to interpret (23).

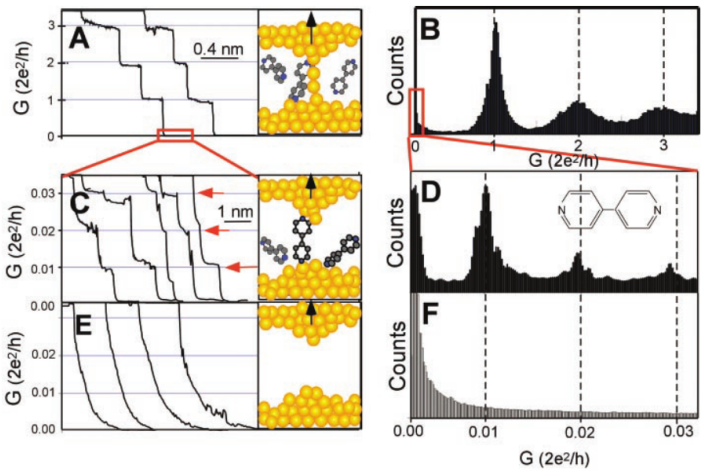
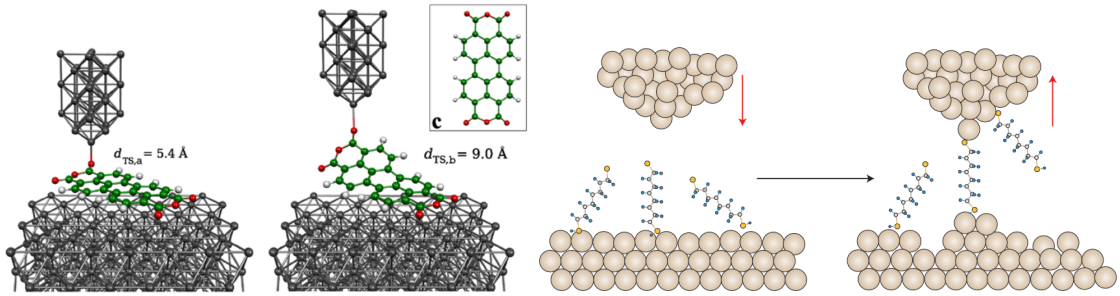


Figure 1.2: (a) Conductance steps observed for a gold bridge formed between a STM tip and the substrate as the tip is pulled away from the substrate. (b) A conductance histogram for 1000 curves like those in (a), showing well defined peaks at multiples of G_0, the conductance quantum which correlates with the number of conduction channels in the bridge. (c) After the gold bridge is broken ($G < G_0$), a series of smaller conductance steps can be seen when a molecular solution is introduced to the gap. These steps are interpreted to arise from formation of stable molecular junctions with one or more molecules bridging the gap. (d) The corresponding conductance histogram for (c), showing clear peaks at multiples of $0.01\,G_0$. Sub-figures (e) and (f) show the conductance profiles for gaps opened in the absence of any molecular solution, with no conductance steps seen. Figure reproduced from (24).

An SPM setup can also be used to create 'break-junctions' in which a Au tip is brought into contact with an Au surface and then slowly withdrawn. This results in a small filament of gold atoms forming as the bonding between the Au atoms in the substrate and those in the tip is equivalent. As the tip is retracted the conductance becomes quantised into integer multiples of the quantum conductance, G_0, and decreases in a step-like fashion (see Figure 1.2). This is the conductance of a single ballistic quantum point contact, and is usually interpreted as the number of parallel atom-wide filaments between the tip and the substrate (25, 26). Eventually, this filament breaks leaving a tunnelling junction with atomically defined contacts and a conductance much less than G_0, as shown in Figure 1.2. This technique may also be performed in a dilute solution of target molecules (24), which results in molecules diffusing into and out of the gap, registering as sub-G_0 plateaus in the conductance. Although these contacts are short lived and the junctions are unstable, thousands of measurements can be performed sequentially, forming and reforming the break-junction, in each

experiment allowing for significant statistical conclusions to be drawn (11). A related 'peel-off' process has also been used to image molecules adsorbed on a surface in a dry environment (27, 28). By taking advantage of tip-molecule chemical interactions and carefully controlling the position of the tip, individual molecules may be peeled off of the surface as shown in Figure 1.3a. However, care must be taken with both of these approaches as some electrode-molecule bonds, in particular the thiol-Au bond, can be stronger than the inter-Au bonds. This can result in deformation of the tip and the substrate as the tip is retracted, making it difficult to interpret the data (29) .



(a) (b)

Figure 1.3: (a) An STM being used to perform a 'peel-off' experiment where molecules are lifted off the substrate and into the gap by a single bond to the tip. Reproduced from (27). (b) A schematic showing an STM tip being used to contact a sub-monolayer coverage of molecules. Once a bond has been made the tip can be retracted to observe electromechanical behaviour. Steps in the conductance can arise from the deformation of the tip and substrate. Reproduced from (30).

Both STM and CT-AFM have proven to be very powerful techniques for performing molecular conductance measurements, offering speed and versatility and providing some valuable insights into the physics of charge transport at the molecular scale (31). However, despite the benefits, the short lifetimes of the junctions and the lack of device scalability exclude them from producing any kind of functional technology. Furthermore, the lack of any kind of gate electrode (with the notable exception of electrochemical gating (21, 29)) excludes these techniques from providing a rich amount of spectroscopic information, and therefore they can provide only limited information on molecular conduction (9).

1.1.1.2 Electromigration

Electromigration describes a process where, under an electrical bias, metallic atoms can be transported due to a significant momentum transfer between conduction electrons and the atomic nuclei. In 1999, Park *et al.* (32) were able to harness this effect to create tunnel junctions by applying a controlled direct current to a lithographically defined gold nano-constriction. Under a large bias a combination of Joule heating and electromigration lead to the nanowires thinning, reducing the conductance, and ultimately breaking as the effects were compounded by the reduced radii leading to a broad range of electrode separations (33). This process could be better controlled by decreasing the total series resistance of the system, allowing for heat to be more effectively dissipated and thereby slowing the migration process sufficiently to allow for >90% yield of tunnel

junctions (34). An alternative scheme employs a feedback-controlled methodology for active engineering of the voltage-current characteristics of the gaps (35–37). In this method, sequential voltage ramps are applied across the device while the current is monitored for any sudden drop, indicating a breakdown of the constriction. The voltage is quickly ramped to zero and the resistance is measured. If the resistance of the device is below a set target resistance, corresponding to the desired electrode separation (see §1.1.2.1), then the cycle repeats until the threshold is met (see Figure 1.4).

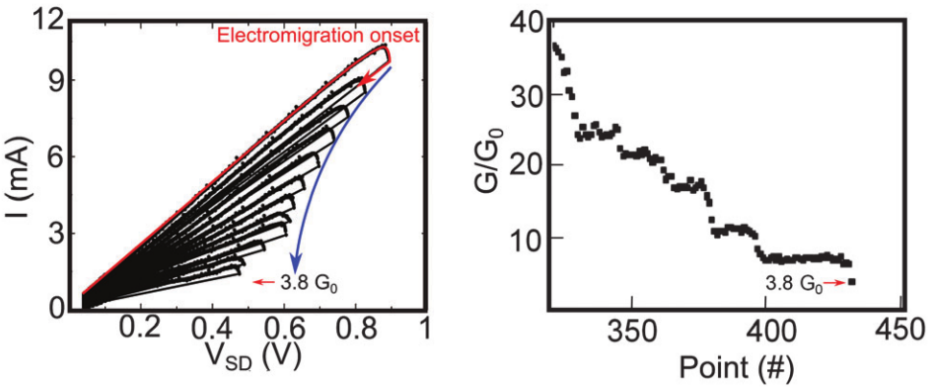


Figure 1.4: Feed-back controlled electromigration of a gold nanoconstriction. The left figure shows sequential voltage ramps across the wire, progressing with the blue arrow as the constriction thins. The right figure shows the same data, plotting the maximum conductance of each sweep as a function of cycle number. Figure reproduced from (9).

A major advantage of the electromigration scheme is the ability to include a global gate electrode under the insulating substrate, as shown in Figure 1.5, allowing for any molecules within the junction to be electrostatically gated. The first 'molecular transistor' was reported by Park *et al.* in 2000 (38), which consisted of a single C_{60} molecule adsorbed between two electromigrated gold electrodes. Using the electrostatic gate, the authors were able to shift the molecular energy levels through the Fermi level of the electrodes. Single-electron tunnelling and Coulomb blockade were observed due to the weak coupling between the molecule of interest and the electrodes. They also reported on a coupling between the single-electron tunnelling and mechanical oscillations of the C_{60} molecule. The authors went on to show Coulomb blockade physics in redox active molecules chemically bonded between the electrodes (39) and to demonstrate Kondo physics in magnetic molecules (40).

A caveat to this scheme is that electromigrated junctions are prone to forming small gold clusters in the gap, which exhibit transport properties such as Coulomb blockade in much the same way that molecules might be expected to, making them difficult to distinguish even with a gate electrode (41, 42). These procedures are often performed at cryogenic temperatures for better control and stability, however the temperature of the environment was shown to have little impact on the local temperatures reached during migration (34), and a method for reliable migration under ambient conditions was also developed (43). However, when forming molecular junctions it is essential that the junctions remain clean and chemically pure so for these experiments migration must be performed in a high vacuum and at low temperature. This requires that the target molecules

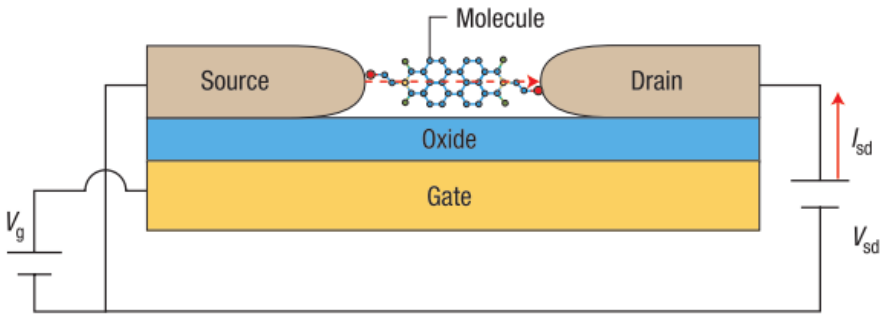


Figure 1.5: A schematic of the geometry of back-gated electromigrated junctions, with the substrate typically made from doped silicon or a metal with an insulating oxide layer on top. Reproduced from (30).

are deposited onto the constriction prior to electromigration. Once a gap has been formed, the molecules can then be allowed to diffuse into the gap by slowly increasing the temperature, which is indicated by a sudden increase in the devices conductance. However, this method exposes any molecules in the vicinity of the constriction to temperatures of several hundred Kelvin (34), which may cause chemical damage. Alternative deposition methods such as evaporation (44) and electrospray ionisation (45) do exist, but the former requires extremely stable molecules, while the latter is highly complex.

A counter to both of the problems was found in the 'self-breaking' phenomena, where constrictions that have been pre-narrowed through feedback-controlled electromigration down to only a few conductance quanta will favourably reconfigure into nanometre sized gaps over time, without the need for applying further bias. By exploiting this slow relaxation of the constriction, the self-breaking scheme manages to almost completely avoid the formation of metallic clusters (46). Furthermore, these nanogaps can be prepared at room temperature and thus in solution, allowing target molecules to self-assemble into the freshly formed, clean gap. These junctions may then be dried, cooled and electrically characterised (9).

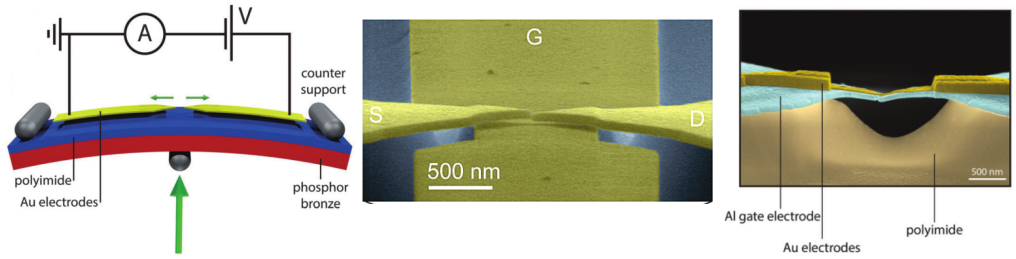
Electromigrated nanogaps are a pivotal technique in the field of single molecule electronics. Their scalability and ease of integration with external fields has meant that they remain an area of active interest (47). They are not without their drawbacks however, and in particular their short lifetimes and lack of tunability once the gap has been formed has led to the pioneering of further methods.

1.1.1.3 Mechanically controlled break junctions

Coincident to the development of electromigrated junctions, mechanically controlled break junctions (MCBJs) were devised for studying the tunnelling properties of metal alloys without the presence of oxide barriers (48). These junctions consist of a metallic wire on top of an insulating and flexible substrate. The wire and substrate are etched to form a local constriction suspended above the substrate. Application of a mechanical load on the backside of the substrate leads to bending, which stretches the wire until it fails under the stress, resulting in clean, atomically sharp electrodes, the separation of which can be adjusted by changing the applied mechanical load. This method was quickly refined to yield highly stable junctions with drifts smaller

than 0.2 picometres per hour (49) at cryogenic temperatures, the size of which could then be adjusted with picometre precision using piezoelectric motors (50).

The first single molecule measurements with these devices were performed by Reed *et al.* (51). The authors coated the wire in a SAM of target molecules with anchoring groups at both ends and performed the breaking in solution to allow the SAM to reform over the freshly broken contacts. After the gap had been formed the solvent has evaporated, the gap can be opened and closed repeatedly until a step like structure is observed in the conductance indicating that molecule(s) have bridged the gap. MCBJs also allow for molecules to be studied without the need for a SAM in much the same way as an SPM break-junction, where the breaking is performed in a dilute solution of molecules which can diffuse in and out of the gap. The control over gap size allows for histograms to be collected by sweeping the bias voltage for each electrode separation over thousands of cycles of closing and opening of the gap. These results can be amassed into a conductance histogram, with the peaks identifying molecular conductance values (52). Waitz *et al.* (53) went on to integrate MCBJs into conventional rigid silicon devices by patterning the electrodes over a local flexible membrane incorporated into the silicon chips. While early MCBJs were more stable than their SPM break-junction equivalents, they too were limited by the lack of a gate electrode.



(a) (b) (c)

Figure 1.6: (a) A schematic representation of an MCBJ (9). (b) A false-colour electron micrograph of a gated MCBJ, where the electrodes are suspended 45nm above the gate. Reproduced from (54). (c) A false-colour electron micrograph of an MCBJ with both the gate and electrodes suspended above the substrate. Reproduced from (9).

The first attempt to incorporate a gate electrode into a MCBJ came from Champagne *et al.* in 2005 (55). They patterned a gold constriction on top of a doped silicon wafer capped with a thin insulating oxide layer. Prior to breaking, the oxide under the constriction was etched away with hydrofluoric acid, leaving the constriction suspended and insulated from the back gate by vacuum. Due to the limited flexibility of the doped silicon, the authors first narrowed the constriction down to a few conductance quanta using electromigration so that only minimal mechanical stress was required to break it. This method boasted the advantage of being compatible with conventional silicon substrates, however the use of electromigration remained problematic. Martin *et al.* went on to develop a similar method that avoided electromigration by suspending a gold constriction above a pre-patterned gate electrode on a flexible substrate, shown in Figure 1.6b (54). It was found however that upon application of large gate voltages the suspended electrodes would bend towards the gate until the tip made contact, effectively forming a single-atom switch. The group went on to improve the design

by suspending an aluminium gate electrode alongside the gold constriction, separated by a thin aluminium oxide layer, shown in Figure 1.6c (56). The flexibility of the aluminium was sufficient to allow for breaking of the gold electrodes while the aluminium remained intact. This method was further improved by Ballmann and Weber (57) using a tantalum oxide dielectric layer, which gave access to a larger range of gate voltages before dielectric breakdown and thus a greater range of level shift in the target molecules.

However, notwithstanding the advantages of an integrated gate electrode, the complex fabrication required to build these devices and the instrumentation required to perform and sustain the mechanical breaking means that, while an arguably more powerful technique for single molecule measurements than SPM or electromigration, MCBJs are limited by their lack of scalability and real-world application.

1.1.1.4 Low dimensional carbon devices

With the advent of low dimensional, metallic and highly stable carbon allotropes such as carbon nanotubes and graphene, the possibility of using these organic electrodes as a replacement for noble metals has warranted much research (9, 58). Unlike the noble metals, carbon electrodes are covalently bound offering little to no atomic mobility and therefore high structural stability, even under ambient conditions. Their 2D or 1D nature means that any nanogap can be located closer to a gate electrode than for a 3D metal equivalent, giving stronger gate coupling to bridging molecules and keeping the contacts in the same plane after breaking. However, one caveat to this is that the gaps and molecules are also closer, and therefore more strongly coupled, to any charge traps within the dielectric. Carbon offers a wide selection of coupling chemistries (59) to anchor molecules to the electrodes, with Van der Waals π-π stacking to the bulk and covalent peptide coupling to the edges being among the most popular in single-molecule electronics. The large chemical repertoire of carbon does however mean that it is very difficult to control the edge chemistry of the electrodes and to remove all surface contamination, which can result in large variability between devices. π-π stacking may be used to avoid edge effects but results in an unknown chemical micro-environment for each bond as the anchor groups have no strict bonding preference.

Carbon Nanotubes

Carbon nanotubes (CNTs) are an attractive electrode choice due to their 1-dimensional nature and high conductivities. CNTs can come in several varieties: single-walled and multi-walled, and both semiconducting and metallic. Separation of CNTs with semiconducting and metallic chirality requires extensive processing (8), but is necessary as semiconducting CNTs exhibit gate dependence and spectroscopic features due to their intrinsic band gap, making them unsuitable for single-molecule electronics. Nanogaps can be opened in CNTs using a process similar to that of electromigration in metallic wires (§1.1.1.2), however, due to the covalent nature of their bonding this progresses by rupture of the carbon-carbon bonds rather than migration of metal atoms and is poorly controlled, resulting in large (>10 nm) gaps which depend on the CNT length (60). For

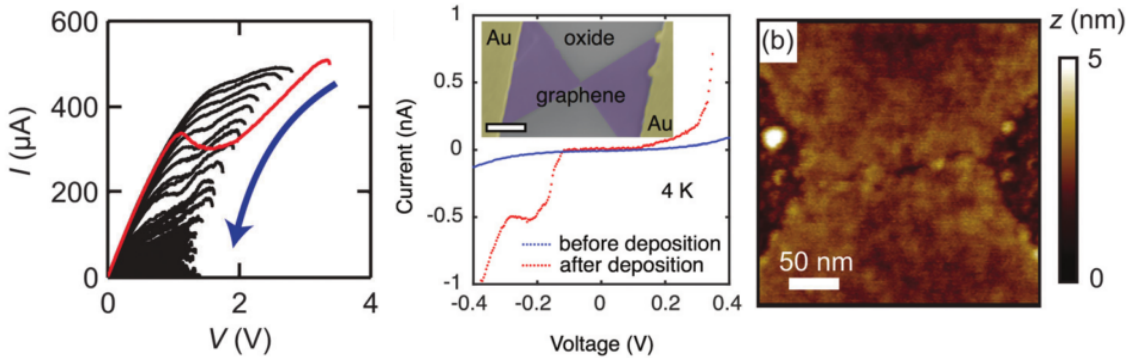
multi-walled CNTs, this gap formation is realised through a sequential breakdown of each carbon shell (61). In order to make these devices suitable for molecular electronics these large gaps can then be 'patched' by depositing organic molecules onto the junction and using an electron beam to decompose the molecules into amorphous carbon, growing the electrodes back to a nanogap (62). However, this method offers no control over the chemical structure of the electrodes. An alternative method for gap formation involves the use of oxygen plasma etching through a lithographically defined polymer mask. The oxygen radicals eat away at the carbon network, leaving carboxylated edge groups which can then be coupled to target molecules through peptide chemistry (63). However, here gap size is limited to the resolution of electron beam lithography systems used to pattern the mask (~10 nm). Perhaps the best method for creating nanometre sized gaps in CNTs is through the use of a helium ion microscope, where nanogaps 2.8 ± 0.6 nm wide have been reported and successfully bridged by small molecules (64).

A major issue with CNTs as electrodes is the difficulty of aligning them with and integrating them into larger circuits and isolating single nanotubes from aggregates. Most studies performed with CNTs create devices through stochastic drop-casting of CNTs over predefined metal contact pads or by a mechanical stamping method which requires CNTs to be grown in-situ with little control over their chirality (65). A method developed by Krupke *et al.* (66) harnessed the technique of dielectrophoresis (see Chapter 3) to selectively deposit metallic CNTs across electrical contacts from a solution of mixed chirality CNTs. This group then went on to achieve single-nanotube deposition across micro-electrodes (67). Recently, CNT-molecule-CNT junctions have been synthesised in solution using peptide chemistry (68). If these junctions can be successfully deposited across electrodes, perhaps using dielectrophoersis, then this could pave a way to reproducibly measure single molecule devices.

Graphene

Graphene, the 2D allotrope of carbon, is another popular choice due to its interesting semi-metallic electronic properties and its planar nature, which allows it to be integrated with current semiconductor technologies (69). Furthermore, unlike CNTs bulk graphene exists as a single structure with uniform electronic properties. Graphene is commercially available in both single and multi-layer sheets grown through CVD (70) or flakes created through mechanical exfoliation of graphite. The flakes, similar to CNTs, must be connected to larger contact electrodes requiring individual manipulation or stochastic deposition. Alternatively, CVD sheets can be transferred over an entire silicon chip, with contact electrodes either pre-patterned or patterned on top of the graphene. This allows for a more controlled device geometry and a much more scalable process, however the graphene is prone to being damaged during transfer (71, 72).

Constrictions may then be patterned onto the graphene sheets or flakes with standard electron beam lithography followed by oxygen plasma etching to remove excess graphene. These constrictions can then be thinned by passing large currents across them in a similar manner to CNTs which results in ultra-narrow



(a) (b) (c)

Figure 1.7: (a) A typical graphene electroburning curve (73). (b) A current-voltage trace obtained for an empty electroburned gap (blue) and for the same gap with a molecule deposited across it (red). The inset shows a false colour SEM image of the device architecture (74). (c) An AFM image of a graphene constriction after it has been electroburned. The gap can be made out to run across the narrowest point of the constriction. Figures reproduced from (73).

constrictions which behave as graphene quantum dots (75). This process was modified to be performed under ambient conditions in the presence of oxygen, which oxidises the graphene as it is heated by the current, allowing for more control over the thinning of the constriction. As such, this method has been dubbed 'electroburning' and can be controlled by a feedback loop in a similar manner to electromigration (76). A sequence of voltage ramps are applied across the constriction while the current is continually monitored. When a sudden decrease in the current is recorded, indicating breakdown of the graphene, the voltage is rapidly swept back to zero to arrest the breakdown. This process is then repeated until a target resistance ($\sim$ 500 MΩ, corresponding to the desired Simmons width) is met (73). Figure 1.7a shows a representative set of current-voltage cycles observed during electroburning. The electroburning method remains an area of active investigation, with much effort being devoted towards better control over the resulting gaps (73, 77–80).

Alternatively, some authors have formed nanogaps in graphene directly through oxygen plasma etching, taking advantage of 'dash-line' lithography to produce ultra-fine features in a polymeric mask and over-etching to achieve narrow nanogaps (81) or narrow constrictions which can then be opened through electroburning (82). Most recently, Bellunato *et al.* demonstrated a novel method for creating graphene junctions by transferring a graphene sheet across two cleaved pieces of silica and etching the central region away with hydrogen plasma (83). Using piezoelectric actuators, the two edges of graphene could then be brought together with subatomic accuracy until the desired tunnel current was registered. By rotating the wafers 15° with respect to each other, a featureless single-point tunnel junction can be formed between the two edges. Later in the same year, Caneva *et al.* (84) demonstrated a graphene MCBJ nanogap, which exhibited pronounced quantum interference effects as when the opposing graphene electrodes overlapped.

Unlike metallic electrodes, graphene's limited density of states does not heavily screen any electrostatic gate voltage, allowing for greater shifting of the molecular levels. However, the discontinuous density of states of single-layer graphene is itself affected by any electrostatic gate and its contribution to the total

conduction of any device must be de-convoluted (85). Multi-layer graphene on the other hand does not show gate dependence (76, 86). Fortunately, any coupling between the gate and the graphene is typically weaker than the coupling between the gate and the target molecule (85).

1.1.2 Theoretical Framework

Here, I will present a simple theoretical description of transport through nanogap and molecular devices in order to aid the discussion of literature and interpretation of results in the following sections of this chapter. For more comprehensive discussions I refer the reader to (3, 87, 88).

1.1.2.1 Tunnel junctions: the Simmons model

Electrons may tunnel through a potential barrier providing that the barrier is sufficiently thin. The separation between nanogap electrodes is small enough that the dominant charge transport mechanism is tunnelling through the thin vacuum gap which acts as a potential barrier. An analytical expression for the tunnel current between such electrodes was first developed by Simmons (89), which, by making several important approximations, enables transport across a tunnel junction to be predicted from the electrode work functions, electrode separation, barrier height and junction area.

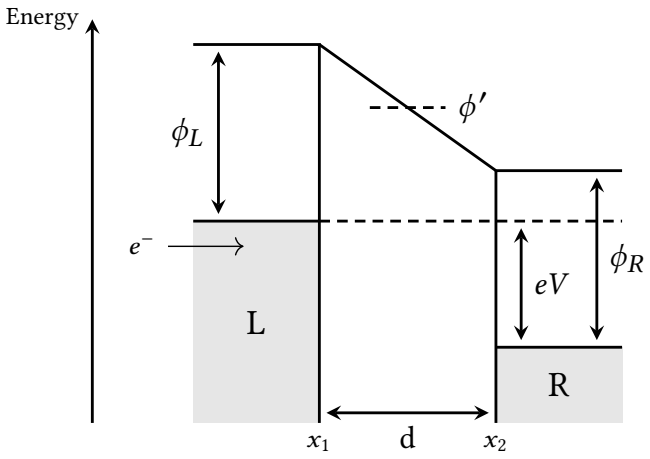


Figure 1.8: A trapezoidal tunnel barrier between a Left (L) and Right (R) electrode, separated by a distance d and an electrical bias V. Here, L and R are of the same material and at zero bias $\phi_L = \phi_R$.

An expression for the current density j flowing through a trapezoidal tunnel barrier of width $d = x_2 - x_1$ between two biased electrodes was derived by Simmons (89):

$$j = e\frac{4\pi m}{h^3}\int_0^\infty d\epsilon[f_L(\epsilon) - f_R(\epsilon)]\int_0^\epsilon d\epsilon_x \mathcal{T}(\epsilon_x) \tag{1.1}$$

where m is the electron mass, $f_{L,R}(\epsilon) = (e^{-(\epsilon-\mu_{L,R})/k_BT}+1)^{-1}$ is the Fermi energy of the left and right leads, respectively, dependent on their chemical potential $\mu_{L,R}$, and $\mathcal{T}(\epsilon_x)$ describes the transmission probability of an electron of energy ϵ_x through the tunnel barrier in the x-direction. An expression for $\mathcal{T}(\epsilon_x)$ can be found

by using the Wentzel-Kramers-Brillouin (WKB) approximation:

$$\mathcal{T}(\epsilon_x) = e^{-\beta \int_{x_1}^{x_2} dx \sqrt{\phi(x) - \epsilon_x}} \tag{1.2}$$

where $\beta = 2\frac{\sqrt{2m}}{\hbar}$ and $\phi(x)$ is the work function at position x. If the work functions of the left and right leads are not equal, but change linearly from ϕ_L at x_1 to ϕ_R at x_2 as the a voltage V is applied symmetrically across the junction then we can write:

$$\phi_{L,R} = (1 \pm a)\phi' \tag{1.3}$$

where $\phi' = \frac{\phi_L - \phi_R}{2}$ is the average barrier height and $a = \frac{\phi_L - \phi_R}{\phi_L + \phi_R}$ is an asymmetry factor, which are used for simplified fitting. Different analytical expressions for the integral $\int_{x_1}^{x_2} dx \sqrt{\phi(x) - \epsilon_x}$ can be found depending on the relative magnitudes of ϕ_L, ϕ_R and ϵ_x (76):

$$\phi_{L,R} < \epsilon_x < \phi_{R,L} : \int_{x_1}^{x_2} dx \sqrt{\phi(x) - \epsilon_x} = \mathrm{d}\frac{2}{3} \frac{(\phi_{R,L} - \epsilon_x)^{3/2}}{\phi_R - \phi_L} \tag{1.4}$$

$$\epsilon_x < \phi_L, \phi_R : \int_{x_1}^{x_2} dx \sqrt{\phi(x) - \epsilon_x} = \mathrm{d}\frac{2}{3} \frac{(\phi_R - \epsilon_x)^{3/2} - (\phi_L - \epsilon_x)^{3/2}}{\phi_R - \phi_L} \tag{1.5}$$

In the low temperature limit where $k_B T \ll \mu_L, \mu_R, \phi(x)$ the Fermi distribution can be treated as a step function and (1.1) becomes:

$$j = e\frac{4\pi m}{h^3} \int_{\mu_R}^{\mu_L} d\epsilon \int_0^{\epsilon} d\epsilon_x \mathcal{T}(\epsilon_x) \tag{1.6}$$

In order to fit (1.6) to the measured current I we must multiply it by the cross sectional area A' of the junction such that $I = A'j$. However, A' is not independent of other variables such as the effective electron mass and so it is incorporated into a prefactor $A = e\frac{4\pi m}{h^3} A'$.

$$I = A \int_{\mu_R}^{\mu_L} d\epsilon \int_0^{\epsilon} d\epsilon_x \mathcal{T}(\epsilon_x) \tag{1.7}$$

Eq. (1.7) is then the expression for the total tunnel current that flows between two electrodes separated by a small gap. Tunnel junctions may be characterised by measuring the tunnel current as a function of applied bias and numerically fitting it to (1.7) in order to extract the parameters ϕ' [eV], a, d [m] and A [eV^{-2}]. Despite the significant approximations made in this theoretical description, which may bring into question the physicality of the extracted parameters across different systems, the Simmons model is used almost universally in the nanogap community to estimate the spacing between nanogap electrodes.

1.1.2.2 Single-level model

Molecules are distinct from macroscopic metallic conductors in that, instead of having a continuous and relatively constant density of states their energy levels exist in discrete orbitals, the energy and shapes of which are determined by their atomic structure. In small molecules energy separation between the highest occupied and lowest unoccupied energy levels ranges from ~1 eV for large conjugated molecules ~10 eV for small, saturated molecules. By placing a molecule in the nanogap and attaching it to the electrodes, we can pass a current through the molecule by applying a finite bias. If a molecular level sits close to the Fermi level then electrons may tunnel from occupied states in the negatively biased electrode to unoccupied states in the positively biased electrode via this molecular level. Given the large energy spacing of molecular orbitals we can assume that the current will be dominated by the one molecular orbital which lies closest to the Fermi energy at any one time, resulting in distinct step-like increases in the current as a molecular level enters the bias window (90). As such, we now need to obtain an expression for transport through a single energy level coupled to two electron reservoirs.

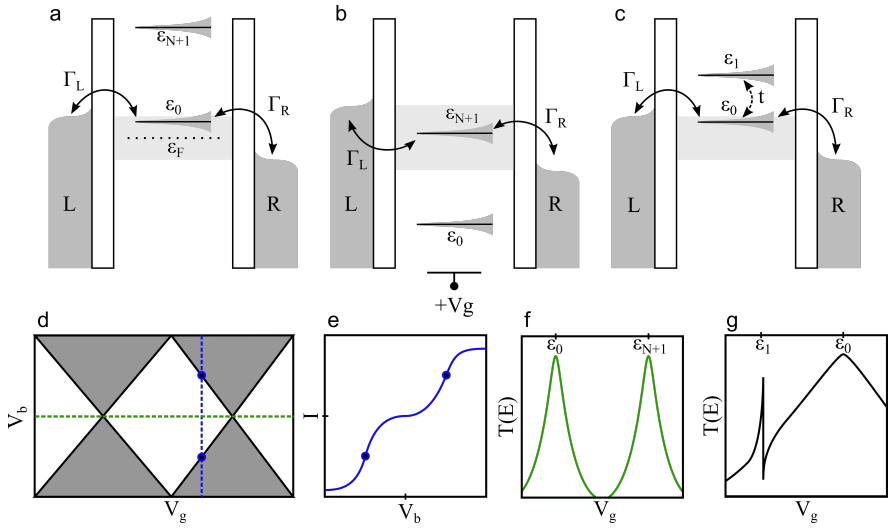


Figure 1.9: (a) A schematic showing a molecular energy level ε_0 coupled to the left and right electrodes by $\Gamma_{L,R}$ which broadens the molecular level. Under bias, if a portion of the broadened level sits within the bias window then electrons can tunnel from occupied states in the left electrode to unoccupied states in the right electrode via the molecular level. (b) Under the application of a gate voltage V_g the positions of the molecular levels can be shifted in relation to the Fermi level. Here, transport is now occurring through the ε_{N+1} level. (c) A representation of the conditions under which a Fano resonance may be observed. Here a local molecular orbital ε_1 is coupled to ε_0 with coupling strength t but is not coupled to the electrodes. (d) A stability diagram showing how the current varies as a function of bias and gate voltages as molecular orbitals are brought into and out of the bias window. (e) A IV_b slice taken along the blue dashed line in (d). The current increases as the bias window overlaps with the molecular level and then saturates as the level is fully incorporated. (f) A transmission function (proportional to dI/dV_g) as a function of gate voltage taken along the green dashed line in (d) showing each molecular level as a broadened Breit-Wigner Lorentzian. (g) A transmission function of the Fano resonance configuration in (c), which consists of a broad Breit-Wigner peak near to ε_0 as well as the antiresonance centred around ε.

By considering the energy required to add/subtract single electrons to/from the single level from/to either of the electrodes we can obtain an expression for the current. Using the Landauer-Büttiker formalism, we can

describe the coherent transport of wave-like particles through an elastic scattering region as:

$$I(V_b) = \frac{2e}{h}\int_{-\infty}^{\infty} dE\ \mathcal{T}(E)\left[f_L(E) - f_R(E)\right] \quad \text{where} \quad f_{L,R}(E) = \frac{1}{e^{\beta(E-(\varepsilon_F \pm eV_b/2))}+1} \tag{1.8}$$

Here, $\mathcal{T}(E)$ describes the transmission function of the scattering region: the molecular energy level, where spin is accounted for by the factor of 2. $f_{L,R}(E)$ are the Fermi-Dirac distributions in the left and right leads, respectively, under a symmetrically applied bias voltage V_b and $\beta = 1/k_BT$. We can write an expression for $\mathcal{T}(E)$ using the Breit-Wigner formula:

$$\mathcal{T}(E) = \frac{4\Gamma_L\Gamma_R}{(E-\varepsilon_0)^2 + (\Gamma_L+\Gamma_R)^2} \tag{1.9}$$

Where ε_0 is the energy of the molecular orbital with respect to the Fermi level ε_F and $\Gamma_{L,R}$ describes the coupling of the molecular orbital to the left and right electrodes, respectively. The wavefunction overlap between the molecule and the electrodes results in some hybridisation occurring between the molecular levels and the local states in the electrodes, the extent of which is described by the magnitude of $\Gamma_{L,R}$. The size of the molecule-electrode coupling also determines the timescale over which an electron resides on the molecule as it tunnels through the junction. Therefore, the molecular levels acquire a lifetime-broadened lineshape - a Lorentzian, described by (1.9), with a full-width half maximum of $\Gamma_L + \Gamma_R$. The coupling also modifies the positions of the molecular levels from those in the gas phase. In (1.9), we have invoked the wide-band approximation in which we neglect any energy dependence of the density of states in the electrodes, and thereby in $\Gamma_{L,R}$. We have also neglected any dependence of the energy of the molecular level ε_0 on the applied bias voltage.

The inclusion of an electrostatic gate electrode enables us to shift the position of the molecular level with respect to the Fermi energy. This allows us to bring molecular levels into alignment with the Fermi energy so that resonant transport can be studied at low biases. We can modify Eq. 1.9 to include the effect of a gate voltage V_g on the position of the molecular level, such that:

$$\mathcal{T}(E, V_g) = \frac{\Gamma_L\Gamma_R}{\frac{1}{4}(\Gamma_L+\Gamma_R)^2 + ((e\alpha V_g - \varepsilon_0) - E)^2} \tag{1.10}$$

Where $\alpha = dE/dV_g$ is the 'lever arm' which describes the relative electrostatic coupling of the molecular level to the gate electrode.

At zero temperature but finite voltage Eq. 1.8 simplifies to:

$$I(V_b, V_g) = \frac{2e}{h}\int_{\varepsilon_F - eV_b/2}^{\varepsilon_F + eV_b/2} \mathcal{T}(E, V_g)dE \tag{1.11}$$

And we can find the conductance $G = dI/dV_b$ by averaging $\mathcal{T}(E)$ over the bias window eV_b. In the opposite limit, of finite temperature and zero bias we can obtain an expression for the conductance by performing a

Taylor expansion on $f(E)$, and by assuming that $\mathcal{T}(E)$ does not vary significantly over the energy range eV_b (91), giving:

$$G(V_b = 0, V_g) = \frac{2e^2}{h} \int_{-\infty}^{\infty} \mathcal{T}(E, V_g) \frac{-\partial f(E)}{\partial E} dE \tag{1.12}$$

The partial derivative of $f(E)$ is given by:

$$\frac{\partial f(E)}{\partial E} = \frac{1}{4k_B T} \cosh^{-2}\left(\frac{E}{2k_B T}\right) \tag{1.13}$$

At 77 K in graphene-based devices such as those described in this chapter $\Gamma \ll k_B T$ (92) and we can neglect the contribution of lifetime broadening. Thus, $G(V_b = 0, V_g)$ takes the form of a purely thermally broadened peak described by:

$$G(V_b = 0, V_g) = \frac{2e^2}{h} \frac{1}{4k_B T} \cosh^{-2}\left(\frac{E}{2k_B T}\right) = G_{\max} \cosh^{-2}\left(\frac{\alpha e V_g - \epsilon_0}{2k_B T}\right) \tag{1.14}$$

where, on resonance, the conductance reaches a maximum value of $G_{\max}$:

$$G(\alpha e V_g = \varepsilon_0) = G_{\max} = \frac{2e^2}{h} \frac{\pi}{4k_B T} \frac{\Gamma_L \Gamma_R}{\Gamma_L + \Gamma_R} \tag{1.15}$$

While Γ_L and Γ_R cannot be uniquely determined from this equation, by setting $\Gamma_L = \Gamma_R$ we can estimate a lower bound for the coupling Γ_{lower}:

$$\Gamma_{\text{lower}} = 4k_B T \frac{2h}{\pi e^2} G_{\max} \tag{1.16}$$

Γ_{lower} can then be determined by fitting experimental conductance traces at zero bias to (1.14). This model may be extended to the case where two or more independent energy levels fall within the bias gap by simply summing their individual contributions to $\mathcal{T}(E)$ which each take the form of that in (1.9). An electrostatic gate can be used to shift energy levels in and out of the bias window, allowing us to build up a stability diagram which maps the current as a function of bias and gate voltage. For weakly coupled molecular junctions these diagrams reveal a characteristic diamond shaped region between neighbouring resonances in which the transport is blocked and the number of electrons on the molecule is fixed: Coulomb blockade, and triangular regions at positive and negative bias in which single electrons may sequentially tunnel through the molecule as the bias window grows to encapsulate the molecular levels. Stability diagrams, particularly as a function of conductance $G = dI/dV_b$, also help to highlight additional higher order processes such as co-tunnelling and the Kondo effect for intermediately coupled junctions (9), but these will not be discussed further here.

1.1.2.3 Fano resonance

Fano resonances arise when a bound state is coupled to a continuum of states. In the case of molecular junctions, the continuum is provided by a delocalised state across the whole electrode-molecule-electrode system while the localised bound state may exists on a portion or pendant of the molecular structure, effectively creating a two state system where the bound state ε_1 is weakly coupled to the core molecular state ε_0 (91, 93). In this case the Breit-Wigner formula in (1.9) is modified to:

$$\mathcal{T}(E) = \frac{4\Gamma_L\Gamma_R}{(E-\tilde{\varepsilon})^2 + (\Gamma_L+\Gamma_R)^2} \tag{1.17}$$

where $\tilde{\varepsilon} = \varepsilon_0 + t^2/(E-\varepsilon_1)$, ε_1 being the energy of the pendant orbital and t describing the coupling between ε_0 and ε_1 (see Figure 1.9c). This transmission function has two maxima when the condition $E - \tilde{\varepsilon} = (E-\varepsilon_0)(E-\varepsilon_1) + t^2 = 0$ is met, as shown in Figure 1.9g. The first, close to $E = \varepsilon_0$ is the standard resonance seen in the single-level model, while a second resonance sits near $E = \varepsilon_1$, the bound orbital energy. But from the expression for $\tilde{\varepsilon}$ we see that the Eq. 1.17 will exhibit a strong anti-resonance at exactly $E = \varepsilon_1$. The close proximity and combination of the anti-resonance at ε_1 and a resonance near ε_1 together are a Fano resonance. As the resonance exists due to couplings within the molecule, it is independent of the coupling between the molecule and the electrodes Γ.

Fano resonances create highly non-linear transmission functions which have the potential to increase the efficiency of switches, the sensitivity of sensors and the performance of thermoelectric devices (94, 95). In 2006, Papadopoulos *et al.* (96) used ab initio calculations on a small molecular wires to show that Fano resonances could be engineered into the molecule by the introduction of specific side groups, and that the position of the resonance could be tuned by changing the chemical nature of these side groups. Furthermore, they found that these resonances had no impact on the nature of the wires' core Breit-Wigner peak. This was in contrast to previous calculations which had shown Fano resonances to be emergent and 'spurious' features of molecular junctions (97), and thereby opened up the possibility of using chemical design to create a molecule with such a resonance close to the Fermi energy.

1.1.3 Anthraquinone

Anthraquinone (AQ) provides an interesting model system for studying quantum interference effects in molecular transport. AQ can be readily and reversibly reduced transforming it from a cross-conjugated to linearly conjugated system (98), and the impact of this change on the electrical transport through the molecule has been reported on experimentally (99, 100). However, a more exotic Fano-type behaviour which has been predicted by some authors to arise from the pendant oxygen groups (101, 102) has yet to be observed experimentally.

A number of compounds which are structurally similar to AQ are discussed in this section, shown in

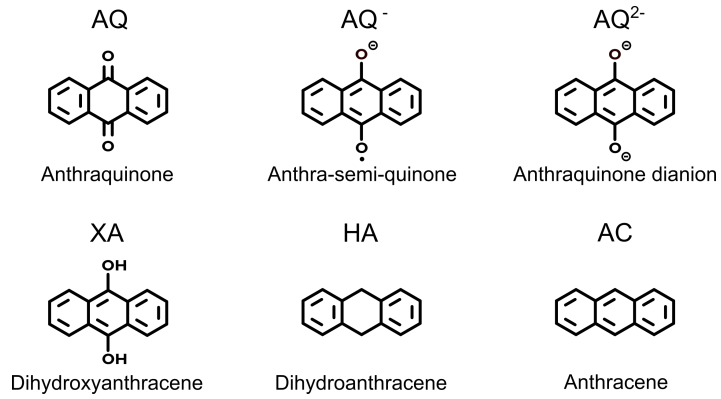


Figure 1.10: Chemical structures of anthraquinone and its structural analogues discussed in this section.

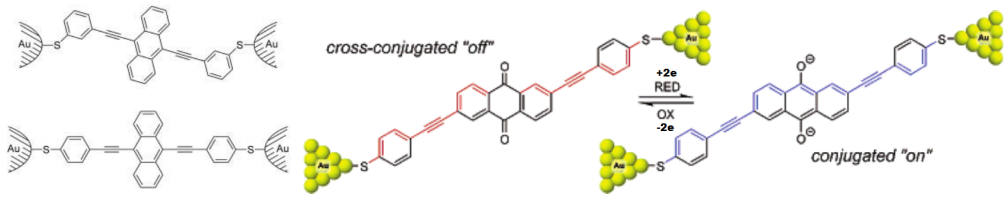
Figure 1.10, which we will briefly cover here. Anthra-semi-quinone (AQ^{-}) and anthraquinone dianion (AQ^{2-}) are the singly and doubly reduced forms of AQ, respectively. Upon reduction, AQ's cross conjugation is lifted and AQ^{-} and AQ^{2-} are linearly-conjugated. In practise, AQ anions are highly reactive and as such AQ^{2-} will rapidly form dihydroxyanthracene (XA) in the presence of any protic solvent such as water. However, for the purposes of transport calculations these molecules are distinct. Dihydroanthracene (HA) is a structural analogue of AQ where each oxygen group has been replaced with two hydrogen atoms. This molecule has broken-conjugation as the central sp^3 carbons cannot participate in conjugation. Finally, anthracene (AC) is a linearly conjugated hydrocarbon analogue of AQ where all carbons are sp^2. In all experiments and most calculations, the core AQ or analogue unit is connected to the electrodes via anchor groups. For the purposes of the discussion here, the transport characteristics for AQ-based molecules are dominated by the core unit and as such the anchor groups will not be explicitly discussed.

1.1.3.1 Conjugation dependence

In 2003 Mayor *et al.* (103) showed experimentally that the electronic transport properties of a conjugated molecule can be strongly influenced by the position of substituted anchor groups: changing from a 'meta' configuration to 'para' configuration of the molecular core and its anchor groups, shown in Figure 1.11a, resulted in a two order-of-magnitude change in the current. This change corresponds to the transition from a linearly-conjugated to a broken-conjugation system. Van Dijk *et al.* (98) went on to synthesise a molecular switch based on anthraquinone (AQ) which could be reversibly switched between a cross- and linearly-conjugated state through the electrochemical addition or subtraction of two electrons, as shown in Figure 1.11b. They showed that the nature of the substituent groups had little effect on the redox behaviour of the core, making AQ a promising candidate for single molecule transport experiments.

1.1.3.2 Interference effects

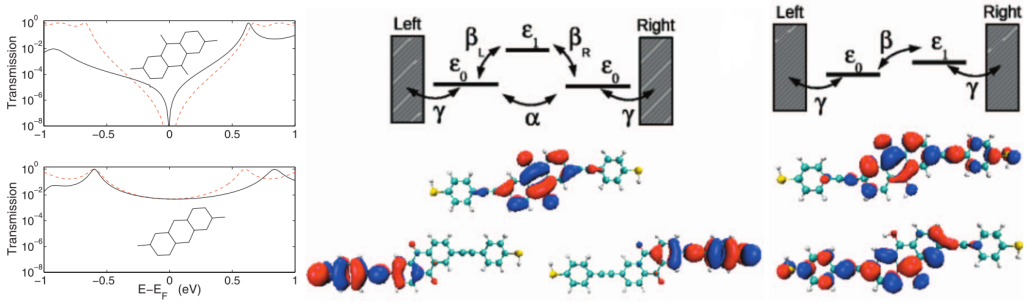
In 2010, Markussen *et al.* (101) published calculations similar to those in (103) but concentrating on the AQ-based molecules. They found that the switching behaviour observed by Van Dijk *et al.* could be understood in



(a) (b)

Figure 1.11: (a) Meta (top) and para (bottom) positioning of thiol anchor groups results in no or a linear conjugation pathway, respectively, between the opposing electrodes. Reproduced from (103). (b) A schematic showing anthraquinone-based redox switches connected to gold electrodes through thiol linkers. Upon reduction of the anthraquinone group, the conjugation changes from cross-conjugation to linear conjugation, opening a conduction pathway and increasing the conductance of the junction. The two separate cross-conjugated units are shown in red, while the single linearly-conjugated chain is shown in blue. Reproduced from (98).

terms of interfering transport pathways, and predicted a six order-of-magnitude difference in transmission around the Fermi energy due to the presence of a strong anti-resonance caused by the presence of the pendant oxygen moieties, as shown in Figure 1.12a. This was shown to be an intrinsic feature of the molecule, only qualitatively affected by the coupling to the leads by a shift in the energy of the anti-resonance. By mapping the molecular orbitals found from density functional theory into a set of three hybrid local molecular orbitals in the vicinity of the Fermi energy, shown in Figure 1.12b, they showed that two possible transmission pathways were possible in the cross-conjugated AQ. These two pathways destructively interfere with each other causing an anti-resonance while in the reduced, linearly-conjugated XA only one pathway is possible and no interference is predicted.

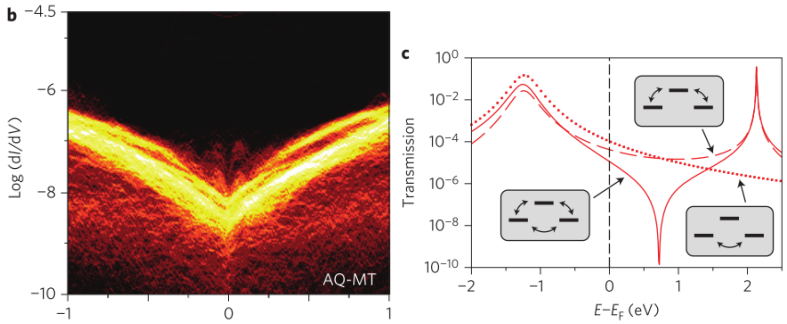


(a) (b) (c)

Figure 1.12: (a) Transmission curves calculated for tight-binding equivalents of both AQ and XA in the gas phase using both a full DFT-GF method (black curve) and a simple Hückel model (red curve). While the transmission function for XA can be seen to consist of two neighbouring Lorentzians at the HOMO and the LUMO, for AQ there is a clear anti-resonance is predicted by both models at the molecular Fermi energy. (b) Local molecular orbitals constructed from the molecular orbitals of AQ lying closest to the Fermi level highlight the two possible pathways that an electron may take, giving rise to interference effects. (c) Local molecular ortbitals for XA showing only a single transport pathway through the molecule. Figures reproduced from (101).

The first experimental transport measurements for AQ were performed by Hong *et al.* (104) who, using the MCBJ technique, found that the conductance of AQ was 300 times less than that of AC. However, their measurements suffered from poor coupling between the molecule and the electrodes and as such their IV

traces showed little structure and no direct evidence of quantum interference. The following year these results were reproduced by Kaliginedi *et al.* (105) in their large scale study of the relation between molecular structure and conductance.

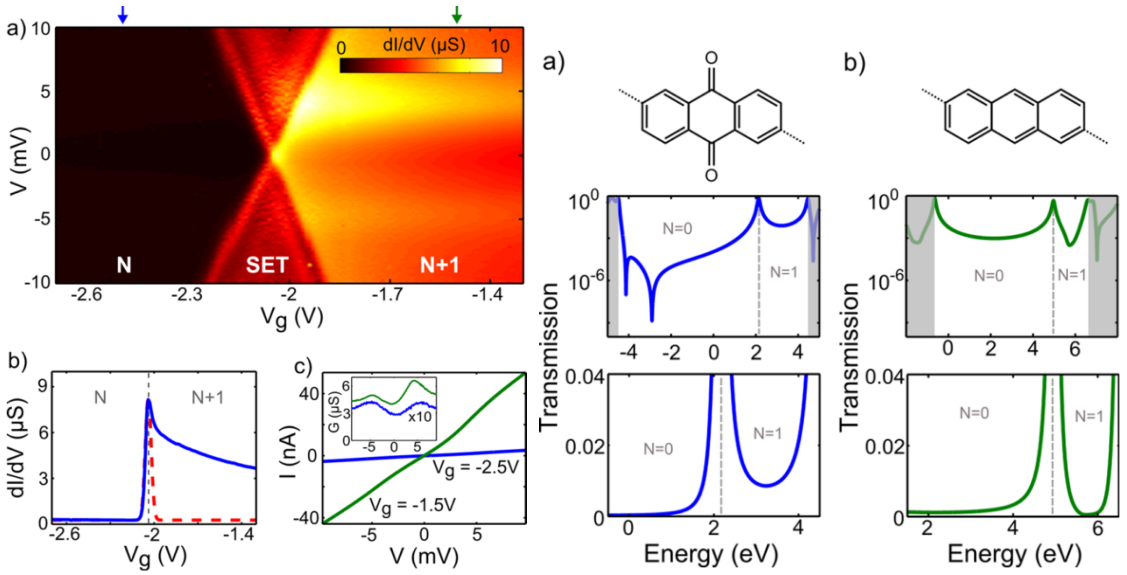


(a) (b)

Figure 1.13: Two dimensional differential conductance histograms for a dithiolated AQ (AQ-DT) (a) and a monothiolated AQ (AQ-MT) (b). Both molecules show characteristic low conduction when compared to their linearly conjugated counterparts, but a clear antiresonance is visible in (b) due to the weaker shift in level positions. The colour scale indicates the number of counts for each value. (c) Calculated differential conductance curves for AQ-MT, where $T(E)$ has been manually shifted by 0, 0.5 and -0.5eV relative to the Fermi energy to sample different possible energy shifts due to the molecule-electrode coupling. For $\Delta E = -0.5$eV the shape and range of the calculated curve can be seen to in excellent agreement with (b). Figures reproduced from (99).

The first direct evidence of quantum interference in this family of compounds was provided by Guédon *et al.* (99) who performed CT-AFM measurements on SAMs of AQ based molecules. They measured hundreds of conductance traces through each SAM allowing them to build the histograms like that shown in Figure 1.13a. They compared an AC-based SAM with two AQ-based molecules, one with a single thiol group to anchor it to the gold substrate (AQ-MT) and a second di-thiolated molecule which would also be able to bond to the gold coated AFM tip (AQ-DT). They also found that both AQ based SAMs showed 2 order-of-magnitude smaller conductance compared to the AC based SAM and observed a strong anti-resonance for the AQ-MT SAM, but not for AQ-DT. The authors explained the anti-resonance in AQ-MT with refined calculations (101) showing that the transport functions $\mathcal{T}(E)$ of the two competing orbital pathways through the molecule had a phase difference of π, resulting in a strong anti-resonance transmission when these 'partial waves' had equal weight, shown schematically in Figure 1.13b. They calculated that when AQ-DT was anchored between the substrate and the tip, the two charge transfer processes in the anchors shifted the anti-resonance to energies well above the Fermi energy, whereas for AQ-MT the single charge transfer aligns the anti-resonance with the Fermi energy. The same authors went on to show that large reduction in conductance between AC and AQ was due to destructive quantum interference in the cross-conjugated AQ rather than a simple loss of conjugation by comparing with a third, broken-conjugation AH (106).

In 2015, Koole *et al.* (100) reported on the in-situ conjugation switching of AQ junctions formed in gated MCBJs. Through the use of the electrostatic gate they were able to reversibly explore two charge states of the same molecule. They found that in the off-resonant region of the N+1 charge state the conductance was



(a) (b)

Figure 1.14: (a) A differential conductance stability diagram showing the transition from the N to the N+1 charge state, measured at 2.9K. The red region corresponds to the resonant transport regime. The left diamond shows much lower conductance than the right diamond, which has pronounced off-resonant transport, with visible inelastic co-tunnelling peaks. The graph on the bottom left shows a differential conductance trace taken at zero bias and plotted against gate voltage. The left side of the curve can be seen to fit well to a Gaussian line shape (red), while the right side strongly deviates from this. The bottom right figure shows two IV curves taken at the gate positions marked with the corresponding coloured arrows on the stability diagram. The inset shows the differential conductance traces, with the blue trace being scaled by a factor of 10 for ease of comparison. (b) Transmission functions calculated for AQ (left) and AC (right), shown on both a normal and logarithmic scale. The charge states are identified with the dashed line marking the position of the LUMO of each molecule. The non-logarithmic graphs serve to compare the elevated conductance in the N+1 state for AQ as compared to AC. Figures reproduced from (100).

greater than that in the N state by an order of magnitude, while both sides show consistent co-tunnelling excitations confirming that the same molecule was being probed. They observed a weak zero-bias Kondo peak in one of the blockaded regions, identifying the N+1 state as the singly charged AQ^{-}. This evidence further strengthens the proposed mechanism whereby the addition of an electron to form AQ^{-} changes the molecule from cross- to linear-conjugation and therefore lifts the quantum interference present in AQ.

1.1.3.3 Connectivity dependence

A recent publication by Ismael *et al.* (102) claims that the quantum interference observed by authors so far is a multiple path Mach-Zehnder-type interference, caused by changes in conjugation but which is distinct from a separate Fano resonance due to the pendant oxygen groups. They predict that if the connectivity of the anchor groups to AQ is changed from 'para' to 'meta' then the anti-resonance in the N state will be shifted to the N+1 state, but that the position of the Fano resonance will be unaffected. As such, they propose that by changing the anchor group symmetry these two interference effects may be disentangled. However, the authors predict that the Fano resonance for AQ exists at ~ -2 eV away from the Fermi energy, making it experimentally challenging to access. It is also worth noting however, that in this paper the authors do not

comment on the important work in (106) and (100).

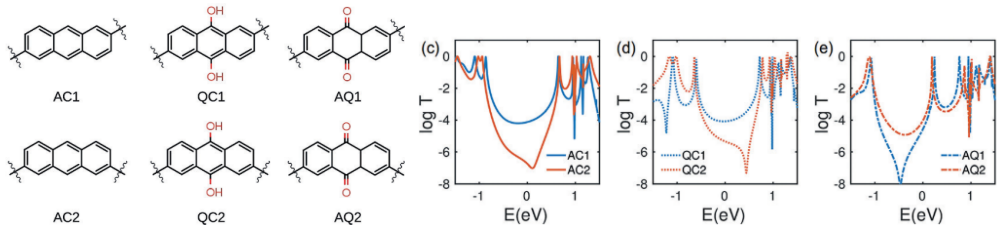


Figure 1.15: (a) Chemical structures of the 'para' (1) and 'meta' (2) coupled molecules studied in Alqahtani *et al.* using the authors' labels. (b) Transmission functions, $\mathcal{T}(E)$, calculated for these molecules coupled to graphene electrodes. For AC1, the para connectivity gives linear conjugation, and a high off-resonant transmission for the neutral state. For AC2 however, meta connectivity leads to cross conjugation and a strong anti-resonance in the transmission spectra. Dihydroxyanthracene (QC) based molecular devices show similar behaviour to that predicted for AC, with the change in connectivity creating a cross-conjugated meta species. Anthraquinone (AQ) molecular devices, however, show a reversed behaviour. Despite AQ remaining cross-conjuagted in both the para (AQ1) and meta (AQ2) configurations, calculations predict that the meta connected device will not exhibit a destructive interference feature. Figures reproduced from (107).

A subsequent paper from the same group (107) supported the prediction that changing the connectivity from para to meta lifts the destructive interference in the N state, despite the conjugation of the core remaining nominally cross-conjugated. The authors therefore claim that 'curly-arrow' rules break down in for AQ. They show that this remains true for AQ independent of electrode material or anchor group, while curly-arrow rules successfully predict interference in the case of AC and XA. However, the paper seems to suggest that, for graphene electrodes, only the N state will be cleanly resolved without being washed out by conduction channels in the electrodes, posing a challenge for the resolution of the Fano resonance proposed in their previous work in graphene-based nanogap devices.

Overall, the physics of charge transport through anthraquinone-derivatives are predicted to display interesting physics such as Fano resonances and destructive quantum interference. The prior theoretical and experimental work shows that these transport features can be charge-state-dependent, and, in the case of quantum interference that relies on coherent transport through the junction, will display a connectivity dependence (108). The aim of the work presented in the remainder of this chapter was to empirically test the predictions made regarding transport through anthraquinones by studying two derivatives with different connectivities in graphene-based single-molecule junctions that have a sufficiently high gate coupling to explore multiple oxidation states of the anthraquinone isomers.

1.2 Methods

In order to investigate the charge transport properties of single-molecules we must first fabricate our nanogap devices. The devices used in this thesis use graphene nanogaps formed through feedback-controlled electroburning as detailed in (73). The fabrication process was as follows:

1.2.1 Graphene transfer

- A 10×10 mm piece of graphene is manually cut from a 6 inch sheet of CVD graphene, purchased from Graphenea, which is backed with copper foil and coated with a thin protective layer of PMMA on top.
- The graphene pieces are placed into an oxygen plasma cleaner copper side up and etched at 50% power for 60s with 25 sccm of oxygen to remove residual backside graphene.
- A 0.4 M solution of ammonium persulfate (APS) in deionised water is prepared in a clean beaker and sonicated to remove any air bubbles.
- The graphene pieces are floated on top of the APS solution copper side down and left overnight for the copper to dissolve.
- 10×10 mm chips of a pre-patterned doped silicon wafer with a 300 nm layer of thermal oxide are cleaned by sonicating in acetone, washing in IPA and drying under nitrogen. The chips are patterned with an array of ~ 700 electrode pairs, formed of 50 nm Au evaporated on top of a 5 nm Cr adhesion layer. The electrode pairs are separated by 5 μm at the narrowest point, between which the graphene will be patterned (see Annex I).
- The etched graphene pieces are transferred three times to clean beakers of deionised water using a clean glass slide to remove residual APS.
- The graphene is transferred from the water directly onto the pre-patterned chips, using an IPA dip to remove any trapped air bubbles or smooth small creases, and is left to air dry for several hours.
- Chips are baked at 180 °C for 1 hour to re-flow the protective PMMA layer and remove residual solvents.
- The chips are submerged in acetone and heated to 50 °C for at least 2 hrs to remove the protective PMMA. The chips are then washed in fresh acetone and IPA and dried with nitrogen.

In order to create the nanogaps, the graphene must first be patterned into constrictions thin enough to breakdown at low (<10 V) voltages.

1.2.2 Graphene patterning

- Each graphene coated chip is loaded into a spin coater and 100 μL of Allresist AR-N 7500.18 (109) negative resist is deposited onto the bare graphene.
- The chip is spun at 5000 rpm for 60s in order to achieve a resist thickness of ~ 3.5 μm.
- The coated chip is baked at 85 °C for 60s to cure the resist.
- The chip is loaded into the cassette of an electron beam lithography (EBL) machine and pumped to high vacuum.

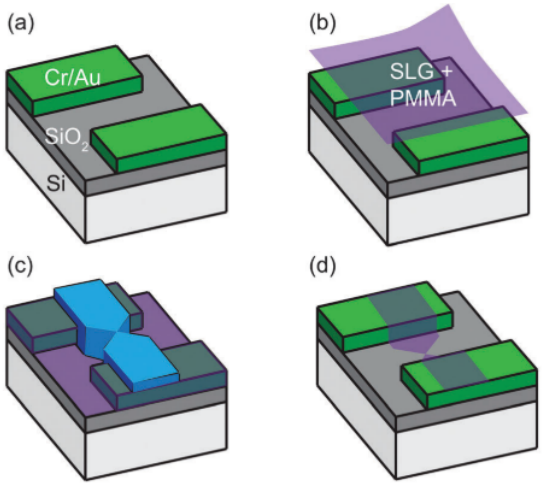


Figure 1.16: Representation of the fabrication process showing (a) patterning of the gold electrodes on a doped Si/SiO_2 wafer using photolithography, (b) wet transfer of single layer graphene (SLG) on top of the pre-patterned electrodes, (c) electron beam lithography of a negative resist to create bow-tie shaped electrodes with a 100 nm wide constriction and, (d) the resulting device after oxygen plasma and removal of the developed resist. Figure reproduced from (73).

- After the EBL has been calibrated (110, 111), constrictions with a minimum width of 100 nm are patterned onto the chip with the electron beam using a 500 pA beam current and a dose of 300 μC cm^{-2}.
- Chips are removed from the EBL and developed in a solution of DuPont MF-CD-26 developer for 45s, removing the unexposed resist, before being washed in deionised water and dried under nitrogen.
- The chips are loaded into an oxygen plasma cleaner and etched at 50 % power, 25 sccm of oxygen for 60 s to remove the exposed graphene.
- The chips are then submerged in Microresist MR-REM 660 at 50 °C for 2 hours to remove the remaining exposed negative resist.
- The chips are washed in acetone and IPA and dried using nitrogen.

The chips should now have clean, patterned graphene constrictions between all pairs of electrodes.

1.2.3 Electroburning

The constrictions must now be electroburned to form the graphene nanogaps. A successful transfer and patterning with good quality graphene should result in most devices being conductive post patterning, with an electrical resistance of around 10 kΩ. The graphene nanogaps are formed via a process of feedback-controlled electroburning, which is performed as follows (73):

- Each device is contacted using an automated probe station to a high-speed DAQ (ADWin Gold II) and a current amplifier (Femto DLPCA-200).

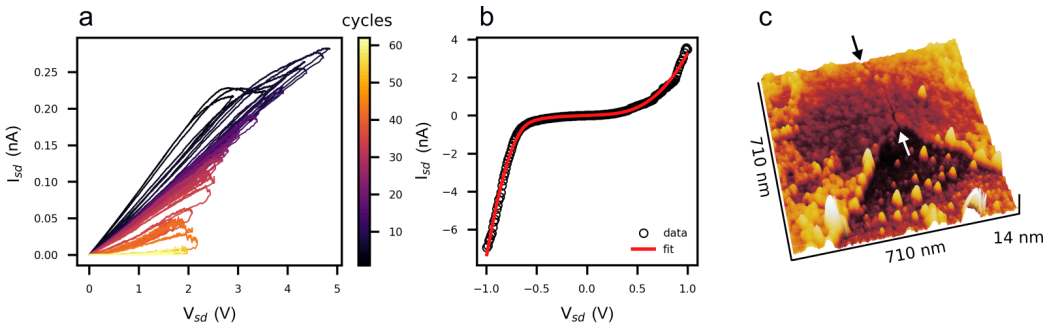


Figure 1.17: (a) A set of representative feedback-controlled electroburning curves. (b) An IV curve of an electroburned devices fitted to the Simmons model. (c) An AFM image of an electroburned graphene constriction, with the nanogap indicated by the arrows.

- A voltage ramp is applied across the device, while the current is monitored to detect any sudden decrease in the current which indicates that the constriction is beginning to break down. This typically occurs at around 5 V on the first cycle for 100 nm constrictions.
- The voltage is rapidly swept back to zero and an IV curve is measured to determine the new resistance of the device at zero bias after this partial breakdown.
- If the new resistance is smaller than a set target resistance then another voltage ramp is applied until breakdown is detected, with the feedback condition adjusted according to the voltage at which the previous breakdown occurred.
- This process is repeated until the resistance of the device is greater than a preset threshold at which the constrictions are believed to have formed nanogaps with spacings of approximately 1 nm between the electrodes, typically 1 GΩ.
- Once the device has reached the target resistance, the IV curves are fitted to the Simmons model (76, 89) (see §1.1.2.1) in order to assess the success of electroburning and obtain an estimate for the size of the nanogaps.
- Devices which fit well to the Simmons model and have resistances in the desired range are selected for further experiments.

Figure 1.17 shows a typical set of electroburning curves and the resulting tunnelling behaviour of the nanogap alongside an AFM image of a well formed graphene nanogap. Depending on the success of the fabrication and the quality of the graphene, the yield of tunnel junctions which fit well to the Simmons model from electroburned constrictions can be up to 75%.

1.2.4 Characterisation

The chips must now be mounted into a measurement setup in order to be fully characterised before molecular devices may be measured.

- Following electroburning, the chip or chip piece is adhered to a 44 pin chip carrier with conductive silver paste and wirebonds are made manually to 21 of the best devices alongside bonds to the base of the carrier in order to apply a gate voltage to the doped silicon that acts as a global electrostatic back-gate for all the devices.
- The chip carrier is mounted into a custom dip-stick vacuum chamber which has electrical connections to a custom break-out box to allow each device to be addressed individually.
- The dip-stick is pumped down with a vacuum pump to 10^{-4} mbar and IV curves are measured for all devices.
- The dip-stick is submerged in liquid nitrogen and allowed to cool to 77 K for approximately 1 hr.
- Stability diagrams are measured for all devices sequentially over a back-gate voltage range of ± 70 V for devices with a 300 nm oxide layer. While a single device is being measured all other channels are set to the same voltage as the back-gate to prevent large leakage currents or breakdown of the oxide.
- Once all devices have been measured the dip-stick is removed from the nitrogen and warmed to room temperature.
- The dipstick is vented to atmosphere and the chip carrier is taken out of the vacuum chamber.

Graphene nanogaps have been shown to display single electron tunnelling due to residual graphene islands within the junction (92, 94), therefore we must check the suitability of the electroburned devices for observing molecular signatures. If the stability diagram for a device is generally featureless then that indicates a clean, 'empty' nanogap free from any localised states. If, on the other hand, the stability diagram shows sharp features or Coulomb blockade-like structure then this is interpreted as a signal of incomplete nanogap formation or the presence of localised states near the Fermi energy. In this case the device is not suitable for molecular transport studies as any molecular features will be indistinguishable from the features of this unknown local state.

If a chip has empty devices, then these devices can be used for molecular transport measurements. A 2 μL drop of a 3 μM dilute solution of the target molecule suspended in toluene is drop-cast onto the chip surface, covering the devices, and the solvent is allowed to evaporate, leaving a sub-monolayer coverage. Once dry, the chip is loaded back into the dip-stick which is again sealed and pumped before being cooled to 77 K. Another set of stability diagrams are taken, and molecular devices are identified by the appearance of Coulomb blockade features in the stability diagram that were not present prior to deposition.

1.3 Results

In my experiments I aimed to first reproduce the results of Koole *et al.* and confirm whether the behaviour they reported also exists in devices with graphene electrodes. Secondly, I aimed to go on to explore the theoretical predictions offered in (101, 102, 112), that the connectivity of AQ with respect to its anchor groups could be used to invert the charge state dependence of the conductivity and thereby potentially observe a distinct Fano resonance. The molecules that were synthesised are shown schematically in Figure 1.18. The anthraquinone core was prepared in two configurations, with anchor groups attached to 'para' positions (AQp) and 'meta' positions (AQm). The anchor groups, also shown in Figure 1.18, are based on an aromatic pyrene core which bonds to the AQ core via alkyne bond so to extend the conjugation. The anchors bind to graphene non-covalently and have additional alkyl chains which help increase the binding energy. Importantly, these anchor groups had been found to give the best probability of forming a molecular junction using graphene nanogaps (92). The synthesis of these molecules was not performed by this author but by colleagues in the H.L. Anderson group in Oxford.

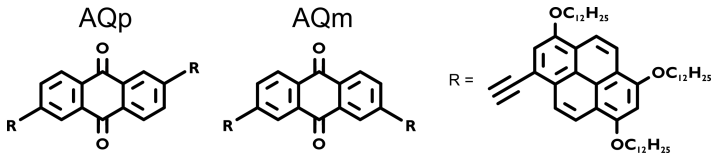


Figure 1.18: The chemical structure of 'para' and 'meta' coupled anthraquinone as well as the pyrene anchor group R.

Several chip architectures were used over the course of this study with different oxides and oxide thicknesses including 300 nm SiO_2, 100 nm SiO_2 and 10 nm HfO_2, where thinner oxides were employed to boost the lever arm α, the fraction of the voltage drop between the gate and the molecular levels, to increase the number of charge states that can be studied experimentally. HfO_2 has a much larger dielectric constant that SiO_2 and can withstand larger electric fields before breaking down, meaning that I could greatly improve the coupling to the molecule with a thin layer of HfO_2. I found that while we could improve the gate coupling with a 100 nm layer of SiO_2 over a standard 300 nm layer, this made the devices much more vulnerable to gate leakage and dielectric breakdown. For 300 nm SiO_2 we find lever arms on the order of 3×10^{-3} and we can access a gate range of $\sim \pm 80$ V before gate leakage dominates the conductance, giving a total level shift capability of ~ 0.5 eV (92). For the HfO_2 devices we can achieve a much larger lever arm of ~ 0.1 but can only access $\sim \pm 5$ V before risking dielectric breakdown. However, this doubles our possible level shift to ~ 1 eV.

Overall, I obtained an average 16% yield of 'empty' junctions which were free from localised states, in good agreement with that obtained in a previous study (92). However, the previous study, which used porphyrin based molecules with identical anchor groups, found a further yield of 36% to form molecular junctions from empty nanogaps, giving a total yield of 4.7%. Despite characterising over 600 devices on which AQ was deposited, I observed only 6 devices which showed molecular signatures, giving a junction formation proba-

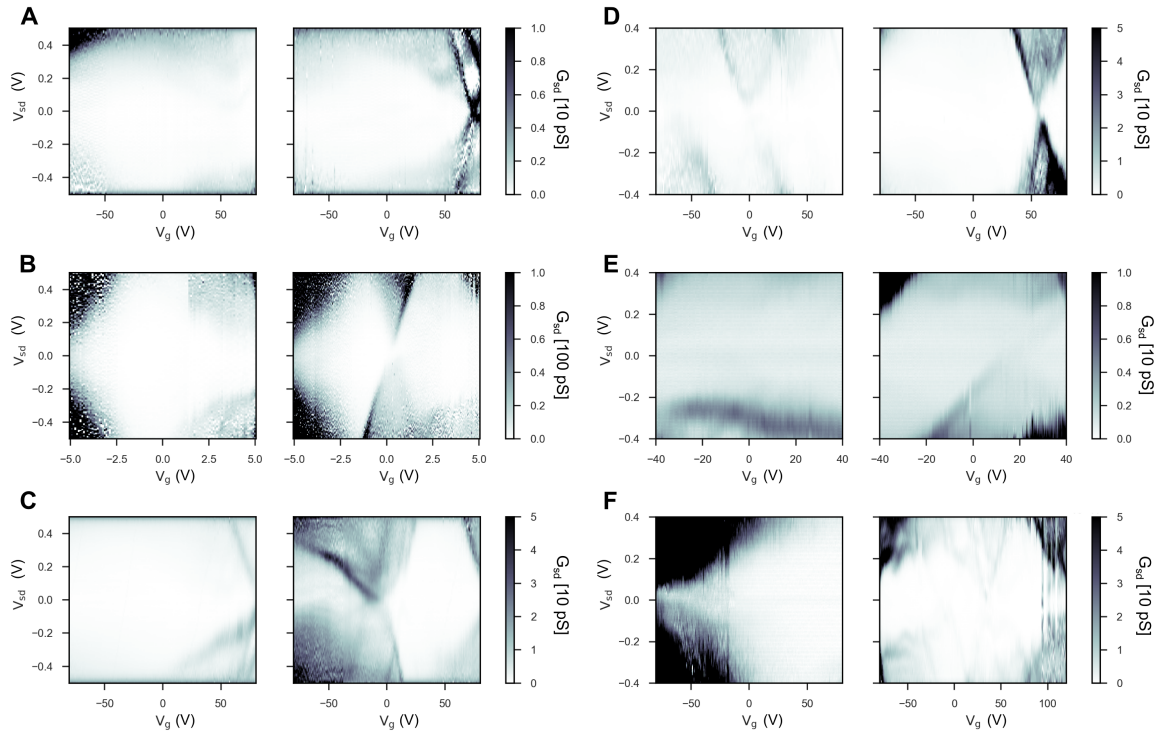


Figure 1.19: Differential stability diagrams taken before (left) and after (right) molecular deposition at 77 K for six devices which showed substantial change. Devices A-D were formed with AQp while E and F were formed with AQm.

bility of ≈ 5% and a total yield of only ≈ 0.8%, almost 10 times less than that found for porphyrin molecules. Of these devices four were formed using AQp (**A - D**) and two using AQm (**E**, **F**).

Figure 1.19 shows stability diagrams, measured before and after molecular deposition, for each of these devices. A device was determined to show a 'molecular signature' if clear Coulomb blockade features were visible in the stability diagram after molecules had been deposited, but only if the device had shown no such structure during characterisation. Devices **A, B, E** and **F** all meet this criteria, while devices **C** and **D**, which show some weak structure beforehand, exhibit post deposition structure which is significantly shifted in gate voltage position and shows greatly enhanced conduction, and have been included to aid the discussion. We can immediately see that in devices **A, C** and **D** we can resolve additional excitations within the single electron tunnelling region. Devices **B** and **C** both appear to show asymmetrical conductance on either side of the charge degeneracy point, which is suggestive of the charge/conjugation state dependent conductance seen previously. Finally, we see that devices **E** and **F**, both formed using AQm, have particularly weak molecule-electrode coupling which makes it very challenging to resolve any features in their stability diagrams.

In order to better understand this data we can take a closer look at the stability diagrams and extract individual bias traces to identify any features. Figures 1.20 and 1.21 show zoomed in and, where available, higher resolution stability diagrams taken around the molecular resonance (left) alongside zero-bias gate traces (centre) and bias traces taken at fixed gate voltages (right), for devices **A-C** and **D-F**, respectively. For each device I performed a fit of the zero-bias gate trace data to Eq. 1.14 in order to extract a lower bound for

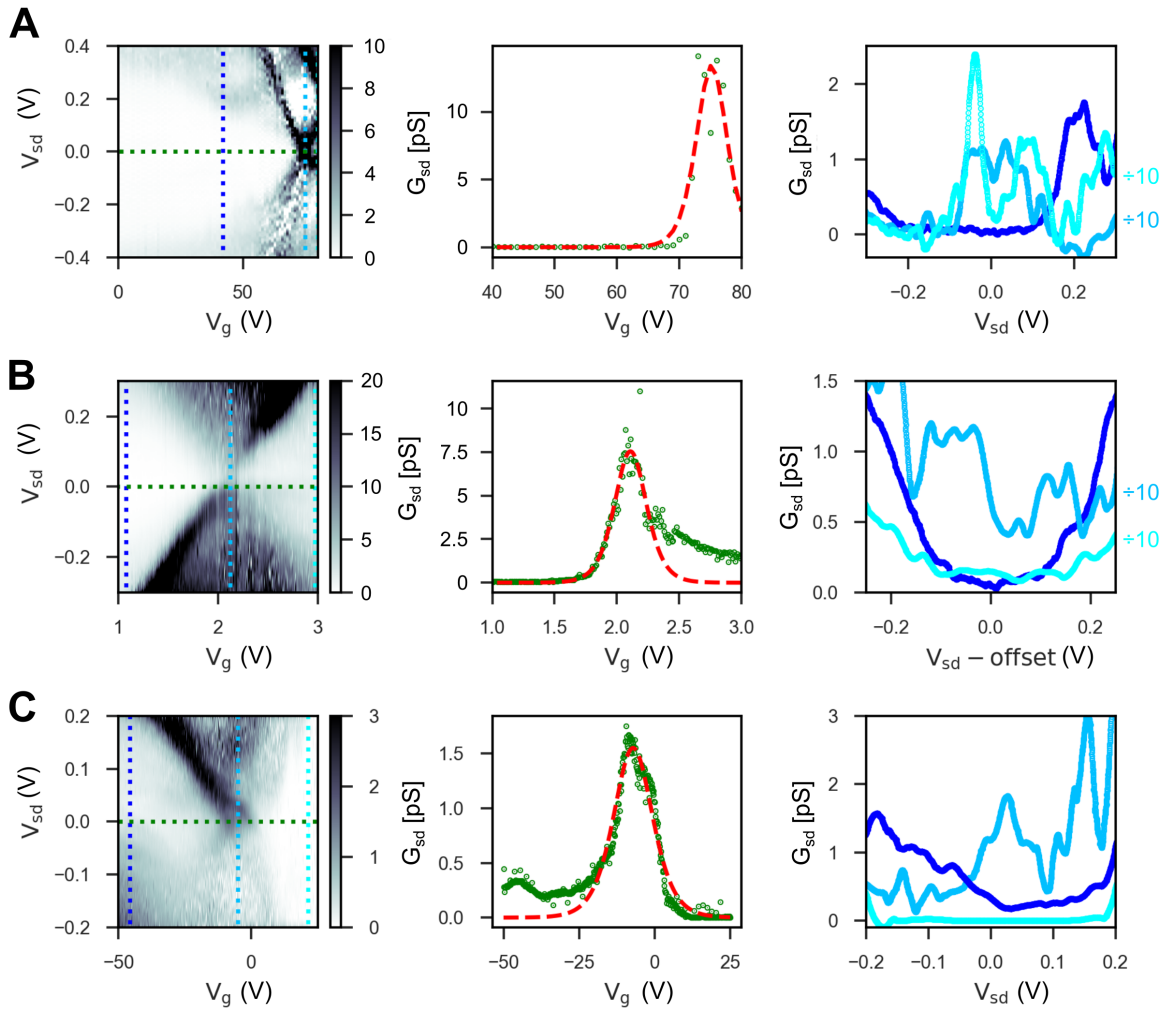


Figure 1.20: Conductance stability diagrams, gatetraces fitted to Eq. 1.14 and IV traces on either side of the resonance extracted from the stability diagrams for devices **A**, **B** and **C**.

the molecule-electrode coupling Γ_{lower} and the lever-arm α. The results of these fits are listed in Table 1.1. The gate traces also give us information on the zero-bias differential conductance within the Coulomb blockaded regions on either side of the molecular resonance.

Device	α	G_{max} (pS)	Γ_{lower}
A	0.004	13.5	5.9×10^{-9}
B	0.07	4.29	1.9×10^{-9}
C	0.001	1.56	6.8×10^{-10}
D	0.006	7.7	3.4×10^{-9}
E	0.001	0.33	1.4×10^{-10}
F	0.004	1.76	7.7×10^{-10}

Table 1.1: Parameters extracted from fitting gate traces to Eq. 1.14.

Koole *et al.* observed an almost 10-fold increase in the zero-bias conductance as the molecule is charged from the N state to the $N+1$ state (see Figure 1.14a, 1.14b). We see the same magnitude of increase in our device **B**, as is particularly evident when comparing the bias traces taken either side of the resonance (Figure 1.20). We see a similar behaviour in **C**, however, in this case the trend is reversed and a larger differential

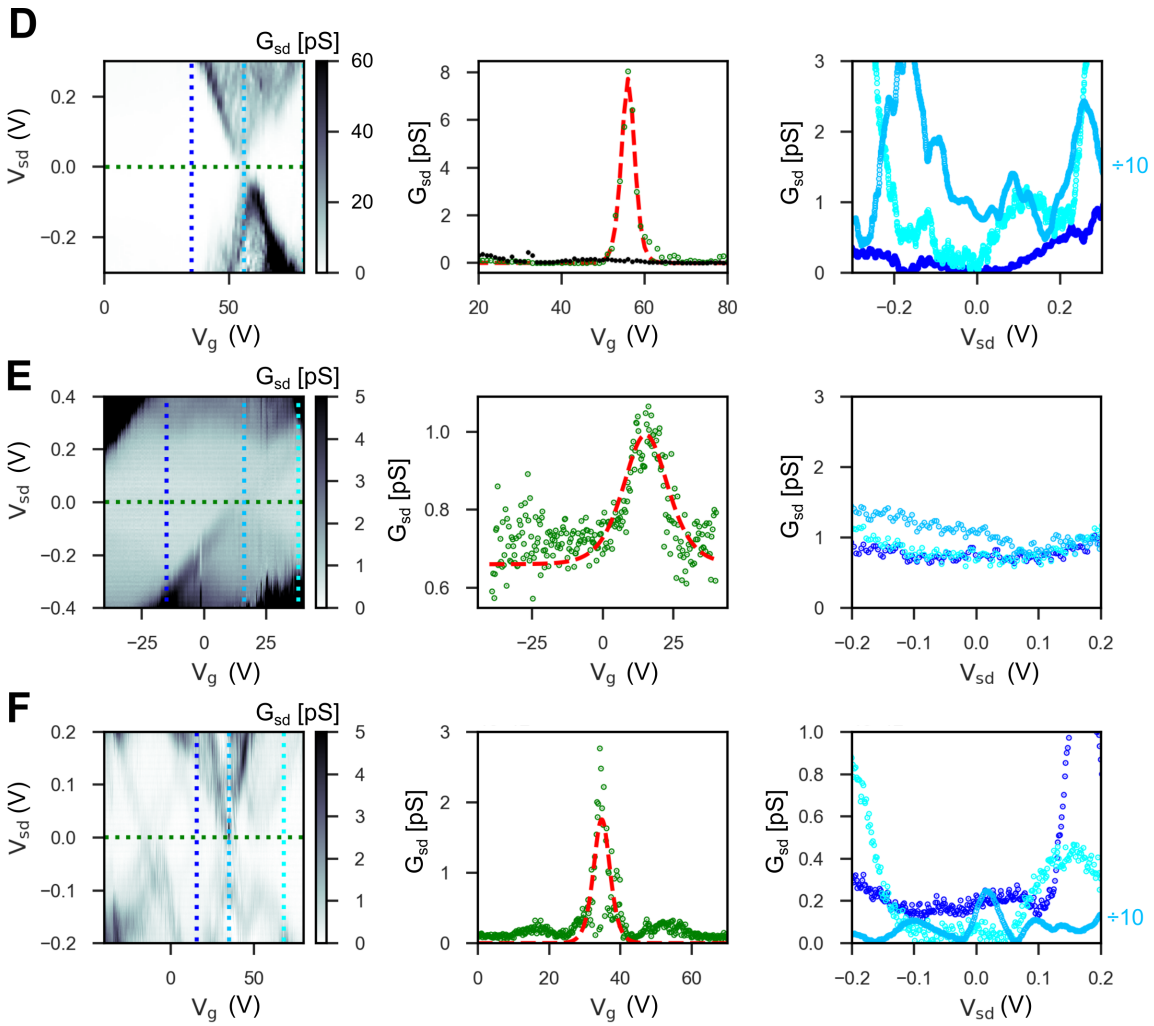


Figure 1.21: Conductance stability diagrams, gatetraces fitted to Eq. 1.14 and IV traces on either side of the resonance extracted from the stability diagrams for devices **D**, **E** and **F**.

conductance is seen at negative gate voltages. The change in the zero-bias conductance on either side of the molecular resonance relates to a change in the conjugation of the molecule with the addition or subtraction of an electron, leading to a substantial change in the off-resonant transport (100, 113). This reversal of charge/conjugation state dependence is what we would expect to observe in AQm, but for AQp it can be explained as a transition from $N-1$ to N as opposed to N to $N+1$. Unfortunately, it is not possible to assess whether device **A** shows any asymmetry as the resonance occurs at the edge of the available gate voltage window. Device **D** meanwhile does not show any obvious asymmetry. At this temperature and with weak molecule-electrode coupling it is hard to draw conclusions about the nature of any excited states or signatures of co-tunnelling in the blockaded region, or whether these features are reproduced across the devices. Any observed excitations are likely to be due either to vibrational modes in the molecule or electronic excitations within the graphene electrodes (85). For device **D** we have included in Figure 1.21 a gate trace of the nanogap before deposition in order to show that no significant features existed which may have conflated with the molecular resonance.

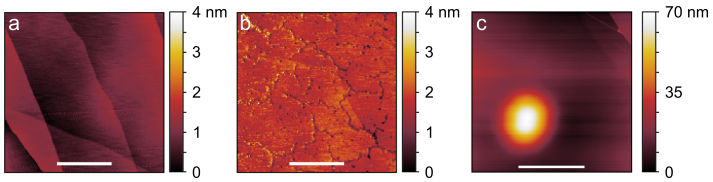


Figure 1.22: AFM images of (a) bare HOPG, (b) a monolayer of porphyrin molecules drop-casted onto HOPG and (c) and AFM image of HOPG after drop-casting an equal concentration of AQm, showing that no monolayer has formed. The scale bar (a) and (b) represents 1 μm, while for (c) it represents 4 μm. These AFM images were taken by J.O. Thomas.

From Table 1.1 we see that my values of Γ_{lower} are fairly consistent across all devices, however they are six orders of magnitude lower than those found by (100) using gold nanogaps, and several orders of magnitude lower than those expected for graphene nanogaps (92). The off-resonant tunnelling current is second order with respect to molecule-electrode coupling, whereas the sequential tunnelling regions that separate the Coulomb diamonds are first order (9). Therefore the small values of Γ make the observance of off-resonant tunnelling features particularly difficult, and we cannot comment further on the presence of co-tunnelling or Kondo peaks. The two AQm devices **E** and **F** are in particular very weakly coupled, with the resonance peak in **E** barely resolvable above the background current. For the AQm devices we expect to see a reversed off-resonance asymmetry as discussed, but we see no sign of this in either due to the extremely weak coupling. Inspecting the stability diagrams for device **F** we see multiple Coulomb diamonds. This is inconsistent with previous theoretical work that predicts a spacing of several eV between charge states in AQ. In this case we can disregard device **F** as a molecular device; instead, it has likely resulted from a rearrangement of the graphene electrodes during deposition and thermal cycling.

In order to draw robust conclusions about the behaviour of graphene based AQ devices and on the difference between AQp and AQm further devices are needed, particularly for AQm. Additionally, magnetic field and temperature dependent measurements down to mK temperatures would have helped shed light on the underlying transport mechanisms. Such low temperature measurements were planned, however, given the very low yield of devices I did not observe the creation of any devices when the equipment required for these advanced measurements was available.

The poor yield of molecular junctions may, in part, be due to the chemical structure of the AQ molecules. In a previous study using porphyrin units with equivalent anchor groups (92), the planar porphyrin cores were functionalised with long alkyl chains which both aided solubility in non-polar toluene and inhibited $\pi - \pi$ stacking interactions between the molecules, thereby preventing aggregation and allowing for interaction with the graphene electrodes. However, here the AQ molecules have no such side groups which may impact on their tendency to aggregate. This difference can be observed with atomic force micrsocopy. Figure 1.22a shows an AFM image of freshly cleaved highly-oriented pyrolytic graphite (HOPG), which is used as an analogue for our graphene nanogap electrodes. Figure 1.22b shows the result of drop casting a dilute soltution of porphyrin molecules on HOPG, which form a uniform monolayer approximately 1 nm high. In Figure 1.22c we see the

result of drop casting a solution of AQm on HOPG, taken after the transport data had been gathered. Here, no monolayer is seen and the image looks much the same as bare HOPG barring one large blob-like feature. We believe that this is an aggregate of AQm. This image suggests that our low junction formation probability may be due to the preference of AQm molecules to aggregate rather than bind to the graphite surface. Interestingly, I found that though the coupling of the AQ molecules to the graphene electrodes is weak it is fairly consistent across our devices, in contrast to the broad spread found in (92). While the absence of side groups may favour aggregation, it may allow the molecules that do couple to graphene do so more reproducibly. The weak coupling itself may also be a consequence of differences in the electron affinities of the core AQ moeity and the pyrene anchors: if the AQ unit has a much greater electron affinity than the anchors then this will result in the molecular wavefunction being centred on AQ, resulting in poor wavefunction overlap and thus poor coupling between the graphene electrodes and the anchors. These observations highlight the importance of molecular design in the field of molecular electronics.

1.4 Conclusion

In this study I aimed to verify the theoretical prediction that quantum interference in AQ-based molecular wires could be altered by changing the connectivity of the anchor groups. However, despite much effort the small quantity and limited quality of the devices created made it impossible to assess these predictions. Through this study, two key challenges with the methodology became apparent:

1. The low yield of featureless nanogaps suitable for molecular deposition ($\approx$ 16%).
2. The even smaller junction formation probability for molecular devices, particularly for AQ-based molecules ($\approx$ 5%).

Due to these limiting challenges, I decided that it would be impractical to continue with the same methodology in the hope of obtaining further devices. Instead, I decided to first direct my efforts towards addressing these challenges and improving the methodology to increase the overall yield of molecular devices. The resulting experiments and the studies that they enabled constitute the remainder of this thesis.

Outlook

Having provided an overview of the field of molecular electronics in terms of the processes used to create nanogap electrodes I moved on to discuss the particulars of molecular devices composed of single anthraquione-based molecules. Though I saw tantalising evidence for quantum interference with results matching those of Koole *et al.*, I was unable to draw conclusions about how changing the coupling from 'para' to 'meta' would change the observed quantum interference due to challenges with device yield and reproducibility. The following chapters will cover efforts to improve the device yield by improving the electroburning process, followed by efforts to improve the formation of molecular junctions by using the technique of dielectrophoresis to capture and position molecules from solution across the nanogap.

Chapter 2

Electroburning

Overview

In this chapter we will take a closer look at the electroburning process and will explore some experiments I undertook as part of an effort to overcome the challenge of the low yield of clean, empty nanogap devices for use in molecular electronics experiments. Specifically, we will discuss the effects of performing electroburning under different atmospheres and how this may affect the mechanism of graphene breakdown.

2.1 Introduction

Graphene nanogaps, formed through a process of feedback-controlled electroburning, are the platform on which the work in this thesis is built. With the advantages of stability, low screening of electrostatic gating potentials and the expansive chemistry of carbon, graphene and other carbon-based nanogap devices have remained an area of active interest (73, 76–80, 82, 83, 114–116).

While the chemistry of carbon may be useful in the formation and manipulation of molecular devices, this chemistry also extends to local contaminants and defects. Defects are common in chemical vapour deposition (CVD) graphene and further chemical contaminants are introduced during the transfer of CVD graphene to desired substrates and lithographic patterning of the graphene into desired shapes. The sp^2 covalent network of bonds between carbon atoms means that electroburning does not occur through the migration of single atoms as in electromigration but instead via more drastic chemical changes, where the end structure may differ substantially from the initial structure. As such, compared to metallic nanogaps, control over and knowledge of the final atomic structure of graphene nanogaps is poor and the relationship between this structure and the electrical transport properties of the device is unknown. This relates directly to the challenge of device yield highlighted in the previous chapter, which represents a key barrier for the use of these devices for molecular electronics going forward. In this chapter, we will attempt to address this challenge before continuing on to further transport studies in later chapters.

2.1.1 Mechanism

The electric field-induced breakdown of graphene generally occurs at the narrowest part of the patterned constriction as at this point the current density, and therefore the Joule heating, is highest (73). This heat leads to a reaction with oxygen in the atmosphere beginning at the graphene edges where the sp^2 hybridisation is broken and the reactivity is greatest. During burning, the gap is thought to form via the propagation of cracks from the edges of the constriction, and these cracks propagate through the graphene as the current density remains highest at the cracks' apexes, continuing until a gap has developed across the whole constriction. However, graphenes thermal properties depend strongly on defects and grain boundaries which may lead to electroburning and gap formation away from the constriction (117). The electrical breakdown of graphene has been observed in-situ within a TEM, observing how applied currents can cause single carbon atoms to sublimate and create cracks (118) and can also result in the reconstruction of the carbon lattice around defects (119). Studies have also observed the formation of linear carbon chains and disordered networks of aromatic rings in graphene constrictions created through electron irradiation (120). However, in all of these experiments the graphene is suspended and under ultra-high vacuum. It is likely that the mechanism of electroburning under atmospheric conditions and atop a substrate will follow a different mechanism given the different chemical and thermal environment.

El Abbassi *et al.* (80) found that the electroburning process, performed using voltage pulses as opposed to voltage ramps (121), behaved differently depending on the atmospheric oxygen concentration. They found that under high-vacuum the breakdown occurs at a higher power than under air, and that they achieved a tighter distribution of gap widths. They attribute this to a mechanistic difference: under air, the breakdown occurs via a self-sustaining and less controlled exothermic oxidation, while under vacuum almost no oxygen will reach the construction during voltage pulses of any length and breakdown occurs via sublimation. They observed similar electroburning behaviour on SiO_2 and Si_3N_4 substrates, indicating that oxygen atoms in the substrate are not involved in the breakdown mechanism.

Lee *et al.* (122) showed how the transport properties of suspended graphene constrictions evolved under high bias as the width of the constriction reduced. They found that transport through a narrow graphene channel was dominated by disorder, both in the bulk and at the edges. A schematic of their findings is shown in Figure 2.1. They proposed that the interaction between the confinement potential of the constriction and the local disorder potential leads to the creation of quantum dots: islands of charge isolated by depleted regions which act as tunnel barriers. In this scheme, Coulomb blockade is observed once the majority of charge carriers passing through the constriction are tunnelling through the quantum dot. As the constriction narrows further disorder may be removed, which can allow normal conduction channels to reopen and the Coulomb blockade to be suppressed, corresponding to an increase in conduction. Alternatively, the expansion of the confinement potential by narrowing of the constriction may ultimately close any normal conduction channel, leaving only blockade behaviour. As the confinement gap is further increased by narrowing of the

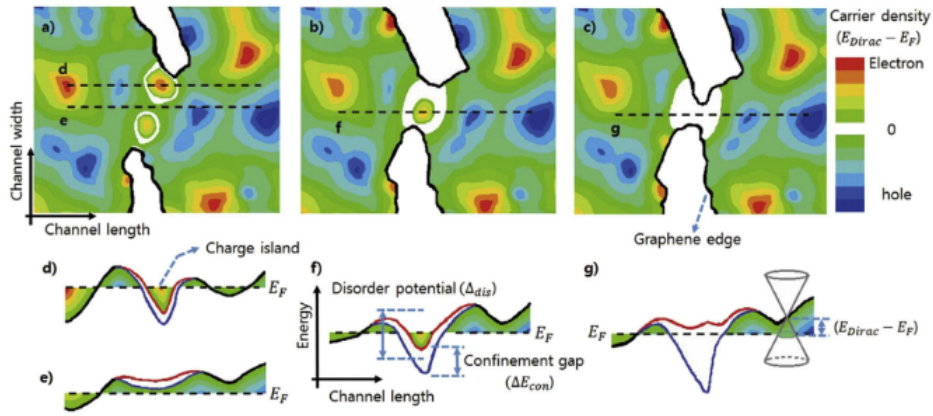


Figure 2.1: Formation of quantum dots during voltage driven narrowing of a graphene constriction. (a) Local disorder coupled with a confinement potential creates two parallel quantum dots within the constriction, but the confinement potential is not great enough to close the normal conduction channel between the dots. Energy profiles taken along lines d and e are shown in (d) and (e), respectively. (b) Further narrowing of the constriction leaves just one quantum dot and the greater confinement energy increases the tunnel barriers to the dot. The energy profile traced by line f is shown in (f). (c) Eventually, the confinement energy brings down the level of the Fermi energy, depleting the charge island of its carriers leaving a single tunnel barrier. The energy profile along line g is shown in (g). Figure reproduced from (122).

constriction with voltage pulses then the Fermi level is lowered and any remaining charge island is depleted of charge carriers. In this case the constriction acts as a single tunnel barrier, with transport characteristics that are electrically indistinguishable from a physical gap with a vacuum barrier.

Similar behaviour has also been observed in numerous narrow graphene devices patterned on top of substrates (123–130). Indeed, electroburning-like processes are well known to result in quantum dots (92, 94) and some authors use the technique for exactly that purpose (75, 131). Such quantum dots, when off-resonance, also yield IV curves which fit the Simmons model. As such, the electroburning procedure does not and cannot distinguish between physical tunnel junctions, carrier-depleted tunnel barriers or disorder-induced quantum dots.

2.2 Evolution during electroburning

In order to gain a better understanding of the electroburning process within our devices, I performed some experiments in which stability diagrams were taken during the electroburning process to see how the character of each device evolved. In order to take stability diagrams using globally-gated devices we had to perform the electroburning process in a 10^{-2} mbar vacuum and at 77 K to prevent excessive gate leakage. Despite no oxygen being present in the atmosphere and the devices being significantly colder we observed that the electroburning curves closely resemble those under ambient conditions. Figure 2.2 shows how one representative device evolves during electroburning. All devices begin with resistances of a few kΩ and are significantly p-doped by residual photoresist on the surface of the graphene, shifting the charge neutrality point δ to large positive gate voltages.

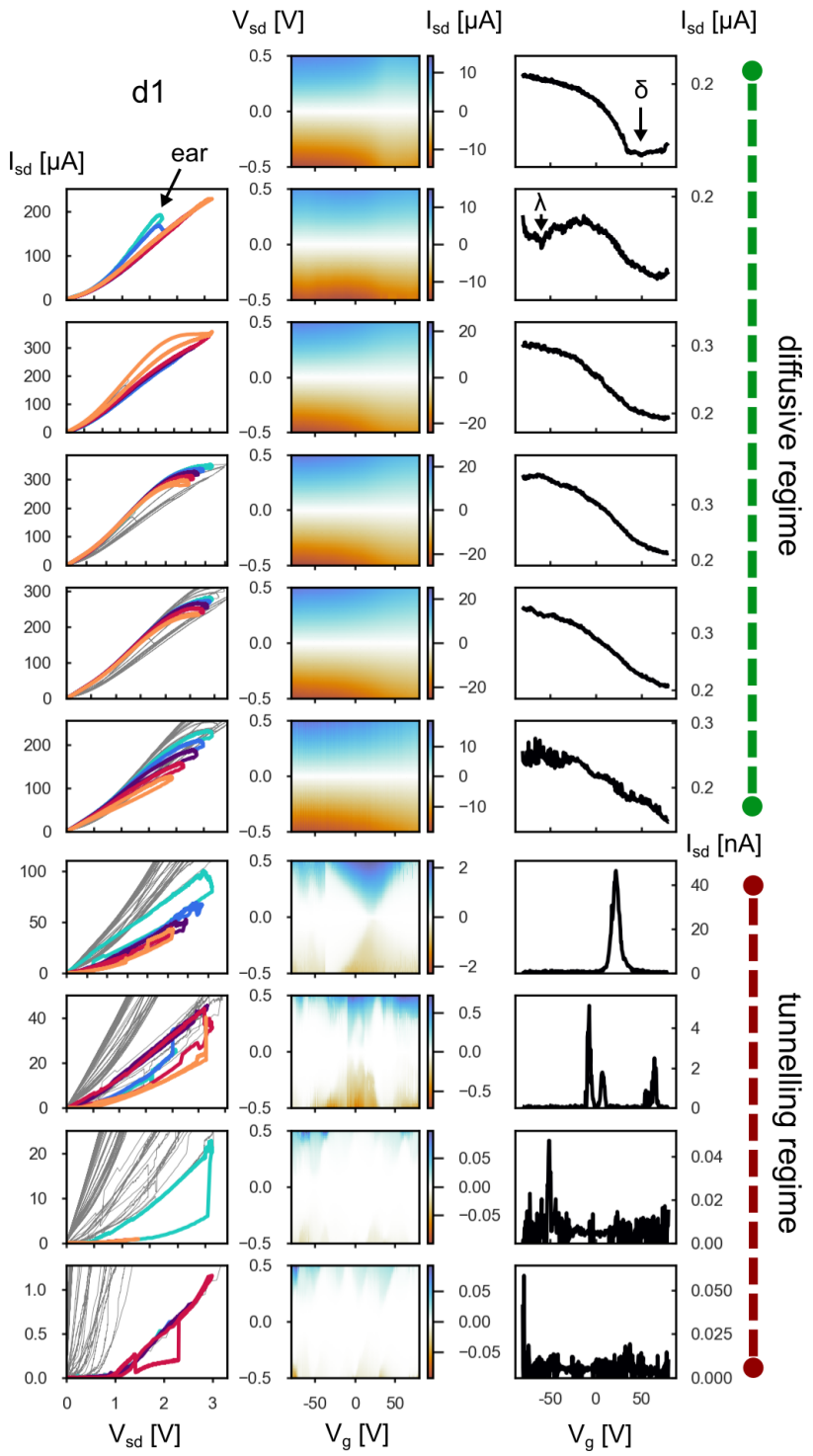


Figure 2.2: Evolution of device d1 during electroburning at 77 K. After every fifth electroburning cycle (left) a stability diagram (centre) is measured and a zero-bias gate trace (right) extracted. The top row shows a stability diagram and gate trace taken of the constriction before electroburning, with the charge neutrality point labelled as δ. During the first five cycles an ear is developed and a second dip γ appears in the gate trace. After the first 25 cycles the device enters a second tunnelling regime where transport is dominated by Coulomb blockade from quantum dots in the constriction. For the electroburning cycle plots each x-axis division in the left column represents 1 Volt. All stability diagrams show the current in μA. Gate traces currents are shown in μA in the diffusive regime and nA in the tunnelling regime.

We see that the electroburning process occurs over two regimes; an early stage regime (green dashed line) where the electroburning feedback cycles are smooth, the stability diagrams are featureless and the gate traces sit in the μA current range; and a late stage regime (red dashed line) where the electroburning cycles show discontinuous jumps in the conductance, the stability diagrams become structured and the current levels in the gate traces fall to the nA range. These two regimes are reproduced across all devices. The early stage regime lasts for between 15 and 30 feedback cycles, with stability diagrams measured every 5th cycle, while the late stage regime shows much more variance with devices requiring between 15 and 85 additional cycles before the resistance threshold is met. The regimes are also differentiated by the curvature of the electroburning cycles, with the early regime showing a negative curvature while the later regime exhibits positive curvature. Other works from the group concurrently looking at similar datasets have also observed these two categories and classified them as representing diffusive and tunnelling conduction mechanisms, respectively (132, 133), which would be consistent with the observations of Lee *et al.* (122).

An interesting observation is that of the 'ear' that is traced out in the first few electroburning cycles. The consensus is that these ears represent a pinch-off in the current as the electrochemical potential in the drain side of the channel approaches and passes the charge neutrality point δ, with the majority carriers changing from holes to electrons as the voltage is further increased (134). Joule heating is thought to remove some surface contaminants and shift δ towards the Fermi level (135), decreasing the voltage at which the pinch-off is observed (73), where the principal contaminants would be residual photo-resist or water.

I however, observed that after the ear and, indeed, in the following cycles, the charge neutrality point δ does not significantly shift its position. In fact, we see from the gate traces that the development of this ear coincides with the appearance of a second dip in the zero-bias gate trace, which I have labelled λ. This feature was reproduced in all devices and was at its most prominent immediately after the ear had been developed. An further example of this feature is shown in Figure 2.3b. The λ point may be a signature of the charge neutrality point of the newly cleaned constriction while the δ point represents the unchanged charge neutrality point of the bulk electrodes. As the cycles continue the λ point appears to shift towards zero while reducing in magnitude. This would be consistent with the constriction being further cleaned and the transport becoming dominated by the lower mobility electrodes. Eventually, the constriction narrows to the point where we enter the tunnelling regime and transport is then dominated by Coulomb blockade of charge islands in the constriction. A second observation is that most devices actually exhibit two ears, though the second is smaller and often eclipsed by later electroburning cycles which trace the same region. This can best be seen in Figure 2.3a for a device where both ears unusually occurred within the first electroburning cycle without triggering the feedback mechanism. The first ear occurs at voltages of 1-3 V across all devices while the second appears at 3-5 V. Exactly what the two ears represent is unknown, but they may result from the loss of different contaminants at different temperatures or a second pinch-off process.

During electroburning, it is common for the resistance of devices to decrease and increase as conduc-

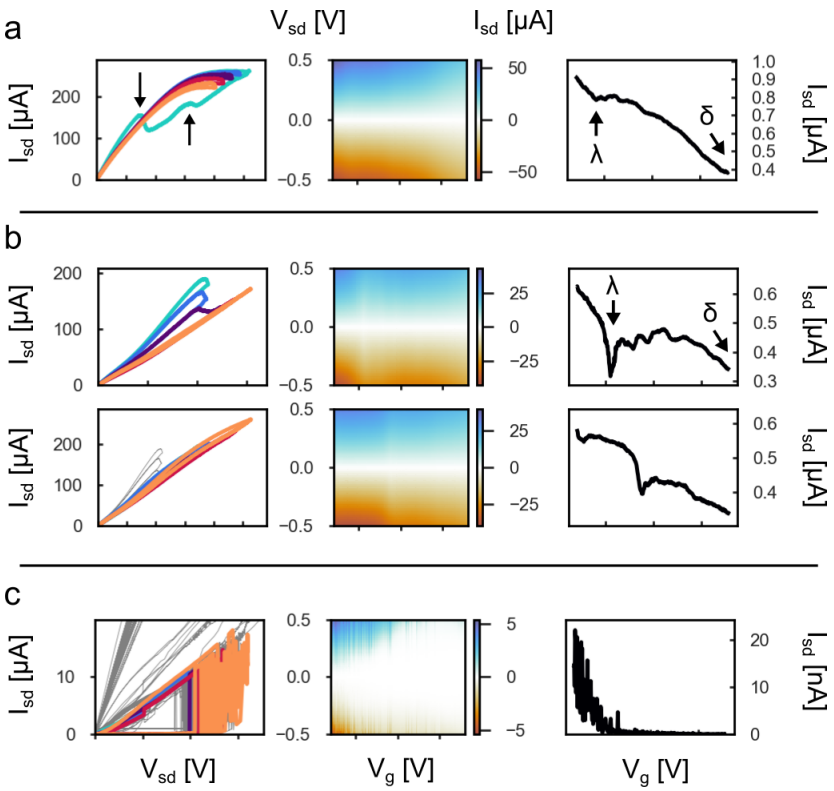


Figure 2.3: (a) Electroburning cycles from device d18 showing two ears traced out within the first electroburning cycle where the feedback is not triggered. Charge neutrality point δ and the ear-induced feature λ are labelled in the gate trace taken after 4 further cycles. (b) Device d14 which shows a particularly prominent λ as the stability diagram was taken immediately after the ear had developed. After a further five cycles the γ point has shifted and decreased in magnitude. Further cycles see the λ point further reduced. (c) Switching events observed during electroburning cycles in device d13 in the tunnelling regime.

tion channels are damaged and restored throughout the process, whether through changes in the disorder potential or restructuring of the carbon lattice. Devices may also become stuck within a single cycle, where the resistance switches rapidly between two states as shown in Figure 2.3c. Switching observed in metallic nanogaps correlates to voltage-induced atomic rearrangements, with jumps taking values of integer multiples of G_0 (136). The origin of these fluctuations in graphene likely does not correspond to single atom rearrangements given the strong covalent bonds between the carbon atoms but may be linked to chemical bonding and confirmation changes at the edges (137). We see that quantum dots are formed in Figure 2.2 during electroburning, a finding that is mirrored across most devices. In fact, the electroburning progresses in a manner similar to that seen by Lee *et al.*, where as the constriction narrows the transport becomes dominated by disordered local charge islands. Subsequent cycles may destroy the quantum dots, shift them to different energies or create new ones, and many devices retain residual quantum dots after electroburning had finished. For the purposes of our work, ideal nanogaps without any localised states are highly desirable in order to be able to determine transport properties specific to any molecule which may be bridging the nanogap, or doping the depleted constriction, as molecules and quantum dots will show the same transport physics.

As quantum dots are induced by disorder, improving the quality of the graphene and cleanliness of the

devices may reduce their prevalence. Unfortunately, our methodology is limited to CVD graphene which contains many grain boundaries and the lithographic patterning employed introduces numerous chemical contaminants. Experiments performed by colleagues investigating whether annealing could be used to better clean the graphene prior to electroburning showed little effect on the yield. Indeed, authors using chemically unzipped nanotubes with well defined edges observed that disorder remained prevalent (129).

2.2.1 Electroburning under different atmospheres

I next performed a set of experiments to discern the effect of performing electroburning under different gaseous environments on the yield and character of the nanogaps. I performed electroburning under air, nitrogen and vacuum to better understand the role of oxygen in the burning process and also performed electroburning in a hydrogen atmosphere in an attempt to functionalise the edges with hydrogen. Termination of graphene with hydrogen is also known to stabilise the edge configurations (59, 138), which may help reduce disordered localised states from forming, and hydrogen termination has been proposed as a method to control the size of the bandgap in the constriction (139, 140). Hydrogen passivation has also been predicted to introduce spin-active edge states at the Fermi level (141, 142) which may find application in single molecule devices (143), but, importantly, would also afford better control over the chemistry of the devices. Electroburning in an oxidative environment likely results in an array of carbon-oxygen edge groups including carboxylic acids, alcohol, ketone, 1,2-diketone etcetera, each with its own chemistry and effect on the local density of states of the electrode. Carbon-hydrogen bonds meanwhile have no such variation which could therefore boost the reproducibility of the devices, which would indicate that the carbon-oxygen bonds are a key source of edge disorder and noise (144). Furthermore, control over the termination of the graphene edges may allow for covalent bonding of target species to the graphene electrodes (145).

The electroburning was performed as follows: The devices to be electroburned were mounted into a sealable dipstick. The dipstick was then pumped out to 10^{-4} mbar, purged with nitrogen, and pumped out again to remove any oxygen. For burning under nitrogen the dipstick was purged again with nitrogen up to atmospheric pressure and sealed. For hydrogen burning 10 mbar of H_2 was released into the pumped dipstick which was then sealed. For vacuum burning the pump was kept running throughout the experiment to maintain a low pressure. Electroburning in ambient conditions was also performed in the dipstick, but the pumping and purging were not performed. After the electroburning was complete the dipstick was purged with nitrogen and pumped down before being cooled to 77 K to measure stability diagrams.

Devices could be categorised in terms of their final transport behaviour. Four categories were used: ideal 'empty' devices with no significant structure in the stability diagram, devices with structure indicating local states, unburned devices where the electroburning had not completed with currents in the μA range and devices with significant leakage currents to the global gate, which prevented further characterisation. The number of devices in each category from each different environment are shown in Table 2.1.

	Air	H_2 (10 mbar)	N_2	Vacuum
Gate leakage	0 (0%)	14 (33%)	2 (10%)	3 (6%)
Unburned	1 (4%)	6 (14%)	3 (15%)	6 (11%)
Structure	16 (62%)	14 (33%)	6 (30%)	5 (9%)
'Empty'	9 (35%)	8 (19%)	9 (45%)	40 (75%)

Table 2.1: Number of devices of each category recovered from electroburning in four different atmospheres.

From these numbers it is immediately obvious that electroburning under vacuum gives a significant improvement in the yield of empty devices than under ambient conditions. The yield of empty gaps formed under nitrogen also seems improved, however the sample size is smaller. These experiments showed a yield of 35% for ambient electroburning, well above the 16% found during the anthraquinone study in the previous chapter. One key difference between this study and the typical electroburning process is that it is performed in a dipstick as opposed to on an automated probe station. On the probe station there is only a short distance between the chip and the DAQ, whereas in the dipstick these are separated by much greater lengths of unshielded cable in the copper looms and the break-out-boxes. These long cables have a significant capacitance which may impede the feedback algorithm during the electroburning causing devices to be burned beyond the desired point.

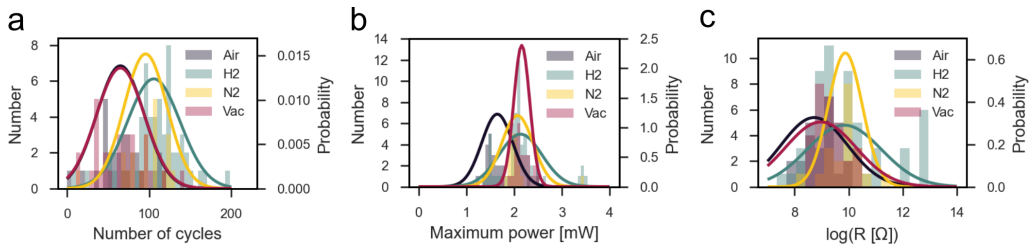


Figure 2.4: Histograms showing the number of cycles (a), the maximum power reached during burning (b) and the final resistance of the devices (c) found after electroburning in each of the 4 atmospheres. The number of devices is labelled on the left axis and the fitted probability densities are shown on the right axis.

Figure 2.4 shows the distributions of the number of electroburning cycles, the maximum power reached during burning and the resistance of the final nanogap for each environment. The number of burning cycles is greatest for hydrogen and nitrogen, which also result in junctions with greater resistances, above that of the target 1 GΩ. Plots for the resistance and maximum power exclude outliers at the low resistance (unburned) and high power extremes, respectively. The maximum power follows a notably tighter distribution under vacuum than under other atmospheres, with H_2, N_2 and vacuum all requiring more power to begin the electroburning process (the highest power is usually required at the start of the electroburning process, after the initial ears).

Selecting a typical device for each environment is challenging due to the range of classes and spread of parameter values for each device, however there are some key behaviours during the electroburning process which are mostly unique to each atmosphere. Electroburning traces which show these characteristic behaviours are shown in Figure 2.5 for air, H_2 and vacuum, while for N_2 we found that the behaviour was

very similar to that in air.

From Figure 2.5 the characteristic behaviours are clear. In air the burning power first increases as the ears are passed while the resistance is relatively unchanged. After approximately 30 cycles the device enters the tunnelling regime and the resistance begins to fluctuate between each successive cycle. Towards the end of the electroburning the resistance suddenly increases past the threshold resistance (1 GΩ) and the burning is complete. Under an H_2 atmosphere the behaviour is quite different: after the initial smooth cycles the resistance and power begin to fluctuate significantly between cycles. A dense switching region is seen at low biases in the plot of the electroburning cycles where the current appears to switch between two values. Under vacuum we observe that devices 'pop' into tunnel junctions with a resistance within the target range in a single step after only a few cycles. In these devices the power behaves similarly to those burned under ambient conditions, increasing and then decreasing in the same manner until the constriction pops. While the popping was not controlled, as noted above the resulting tunnel junctions were also largely featureless. However not all devices in vacuum behaved this way. Figure 2.5d shows how some devices burned in vacuum would recover between cycles or even during a single popping cycle as the voltage was swept back to zero. This gives a switching behaviour in the resistance and burning power but at a much reduced rate than that under H_2.

From these results it seems that all devices undergo a similar process during the first few electroburning cycles, regardless of the atmospheric conditions. This is likely some form of contaminant removal driven by Joule heating, where the ears may represent the removal of different dopants, the two leading candidates being water and photo-resist. We see from AFM images of electroburned devices (Figure 1.17c) that the region immediately around the constriction is much cleaner than the surrounding graphene. We know that, under vacuum the graphene construction can reach temperatures of 2500 K (132), and that the electroburning process is capable of removing significant amounts of material from the surface of the graphene (79). Any surface contaminants would have either sublimated or decomposed before reaching these temperatures, suggesting that they are mostly removed in the early cycles and may be connected to the position of the ears. The mechanism behind contaminant removal may explain the differences in the maximum power reached during electroburning between air and other atmospheres, with oxidative decomposition requiring less energy than sublimation. Alternatively, the larger burning powers could be a result of the doping of the clean graphene around the constriction by the gases themselves, which would cause a shift in the Dirac point and therefore the carrier density, resulting in a change in the voltage required for breakdown to begin (146).

2.2.1.1 Switching

The switching that occurs in H_2, vacuum and sometimes in air (see Figure 2.3) may be indicative of the underlying mechanism, where steps in the conductance of size G_0 or multiples thereof would indicate the opening or closing of transport channels. Previously, it has been suggested that these switching events may

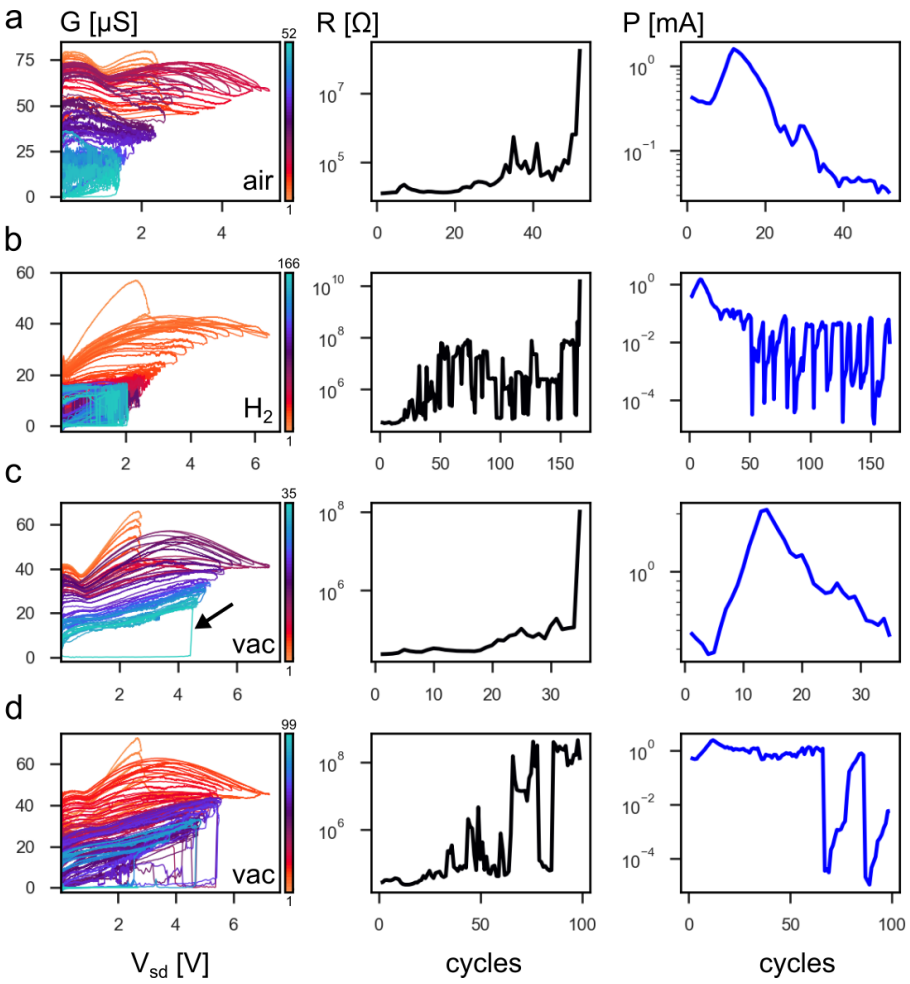


Figure 2.5: Plots showing representative electroburning cycles (left), changes of device resistance with each cycle (centre) and maximum power during each cycle (right) for (a) burning in air, (b) burning in H_2, (c) burning in vacuum where a device shows the characteristic 'pop' indicated by the arrow and (d) burning in vacuum where a device recovers and switches after popping.

arise due to the formation and breaking of carbon chains across the nanogap (79, 120, 137, 147, 148). In order to evaluate the steps I employed a step-counting algorithm (149) to analyse each electroburning cycle of all devices listed in Table 2.1. In order to discern the steps from background noise I first applied an iterated-median filter to the data with a window size of 5 data points. This helped to filter out transient spikes in the conductance while preserving small steps. I then applied an algorithm which transforms the data, which we first normalise, in such a way that large discontinuities give a large response, while small fluctuations give a small response, shown graphically for a single electroburning trace in Figure 2.6a. We filter the significant steps from background noise by applying the condition that steps are only considered if their algorithmic significance $|s|$ is greater than 0.05, and then they are only counted if the heights of the associated conductance steps $\Delta G/G_0 > 0.001$. This is an arbitrary condition but one that qualitatively captures the large steps of interest while filtering out the numerous small background fluctuations.

In Figure 2.6b-e 2D histograms of step size vs. step position are shown for all for environments. Under air the step size distribution is uniform, with the number of steps increasing as the step size approaches zero,

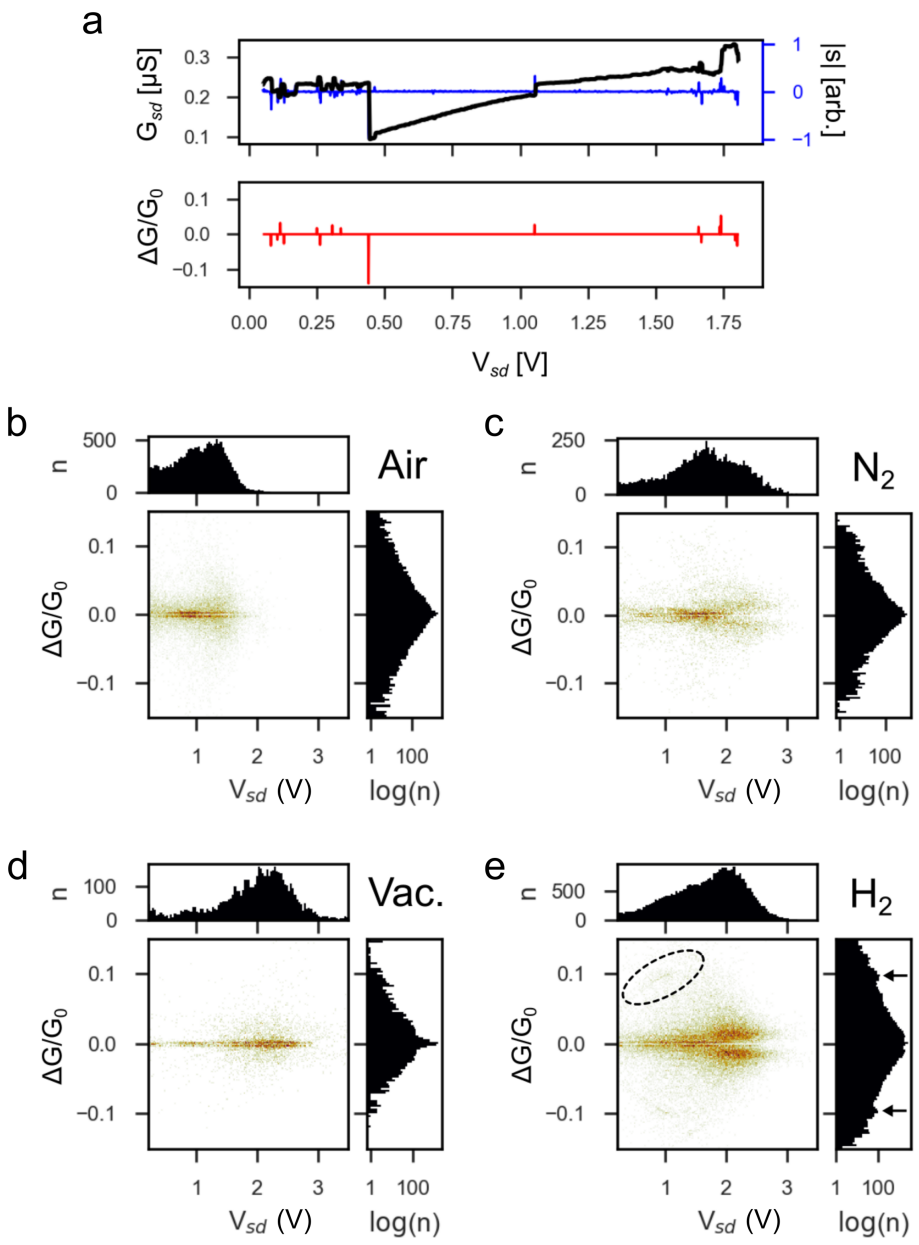


Figure 2.6: (a) Top: A single electroburning cycle (black) and the output of a step detect algorithm (blue) which identifies all steps in terms of their significance $|s|$. Bottom: A filtered output of the step detect algorithm showing the step heights in $\Delta G/G_0$ of only the most significant steps. (b) 1D and 2D histograms of the height and bias of every step found throughout all electroburning cycles in all 26 devices burned in air. (c) Histograms for electroburning under nitrogen for 20 devices. (d) Histograms for electroburning in vacuum for 54 devices. (e) Histograms for electroburning under hydrogen for 42 devices. In the step height histogram we see two populations of steps centred around $\pm 0.1\,G_0$, labelled with arrows. The $+0.1\,G_0$ population can be identified in the 2D histogram in the region circled by a dashed line. A similar population can be seen for $-0.1\,G_0$.

suggesting that they do not correspond to any specific chemical interaction. The same is broadly true for N_2 and vacuum, though in these environments the detected steps occur at larger voltages in line with the distribution of peak powers in Figure 2.4. Under H_2 is where we see some indication of a specific process, with a pronounced bump at $\pm 0.1 \Delta G/G_0$. We measured more devices under H_2 than for air and nitrogen, so these sub populations could appear for the other atmospheres with the collection of further data. However,

it is notable that under H_2 I found an average of ~ 900 steps per device, or about 9 per cycle. For air this was lower at ~ 600 steps per device, but the typically lower number of cycles (see Figure 2.4a) means this also gave about 9 steps per cycle. Under nitrogen these numbers were lower still at ~ 450 per device and ~ 5 per cycle, while for vacuum they are only ~ 100 per device and ~ 1.5 per cycle. It is not particularly surprising that under vacuum we see far fewer steps as devices tend to pop before they reach the tunnelling regime where most steps occur. What exactly these fractional 0.1 G_0 steps under hydrogen could correspond to is difficult to say, however in many single molecule experiments such sub G_0 peaks are interpreted as signals of molecular conductance (11, 105). This value is in contrast to those seen in metallic electromigrated nanogaps or MCBJs where the constriction takes conductance values at integer multiples of G_0 as it is thinned, indicating the number of open conductance channels. For such devices, once the conductance decreases below G_0 this is interpreted as the formation of the nanogap.

If we assume that this sub-population is due to an interaction between H_2 and graphene then could it indicate the desired functionalisation of the graphene edges? We observe for all atmospheres that their is a strong symmetry between the number of positive and negative conductance steps in Figures 2.6b-e, and that that symmetry is reproduced for the 0.1 G_0 steps under H_2. This would not be consistent with a chemical mechanism, whether oxidation, hydrogenation or sublimation of carbon atoms, as these processes should be irreversible. We note that for H_2 a significant proportion of the electroburned devices showed gate leakage. Gate leakage can occur when a conduction pathway is opened in the dielectric, perhaps formed by impurities which charge carriers may tunnel between. It is known that hydrogen can interact with SiO_2 to form charge traps where hydrogen ions are repeatedly captured and released (150). Switching of charge traps would gate the graphene constriction and may produce the switching we observe in the electroburning cycles. Furthermore, the diffusion of hydrogen into the substrate may also explain the gate leakage as the hydrogen ions can act as charge carriers themselves by hopping through the dielectric lattice (151).

From these experiments the vacuum burned junctions appear most promising for the use in molecular electronics due to their featureless transport characteristics, despite the limited control over their formation. Furthermore, it was found that no significant change was seen in the stability diagrams after the devices were exposed to atmosphere and re-characterised, indicating that the vacuum formed nanogaps were stable and did not harbour dangling bonds. The nature of the edge chemistry in this case remains unknown, though it is possible that the edges may be functionalised with oxygen through an interaction with the substrate. To test the suitability of the vacuum devices for molecular electronics I deposited porphyrin-based molecules with a 35% junction formation probability (92) onto vacuum burned nanogaps. However, after depositing molecules on more than 20 structureless junctions, no molecular devices were observed. This suggests that the junctions are not equivalent to the ones burned under atmosphere. The popping behaviour observed during electroburning may indicate sudden and catastrophic destruction the graphene constriction, to form a gap too large for molecules to bridge. The heat generated may also cause a partial breakdown of the SiO_2

into SiO_x to create weakly conductive tunnelling channels through the substrate, resulting in the observed weak tunnelling behaviour with no gate dependence. This may help explain the broad distribution of final resistances of junctions obtained through vacuum burning. The switching behaviour observed under vacuum, where devices may revive themselves after a popping event, might then be attributed to resistive switching within the degraded SiO_x (152). Whatever the switching mechanism under vacuum, it occurs over a much longer timescale than that observed under hydrogen.

2.3 Conclusion

Overall, the early stages of electroburning under all environments follow similar behaviours, with the key differences occurring in the tunnelling regime. Air and nitrogen atmospheres are very similar in terms of yields and behaviour, with the main difference lying in the higher powers reached during early electroburning cycles under nitrogen. This suggests that oxygen may assist the removal surface contaminants or initial breakdown of the graphene during early stages of electroburning, but that it may not be crucial for electroburning once we enter the tunnelling regime. This may be a manifestation of a change from oxidation to sublimation as the driving mechanism, or may even indicate that oxygen plays a limited role in the whole process (73, 80). In vacuum the electroburning differs with the prominent popping behaviour, but not under nitrogen where sublimation should also be the principal mechanism, which suggests that the popping is caused by the absence of any atmospheric gas, not specifically oxygen.

What then causes the popping and why does it occur at the beginning of the tunnelling regime rather than at the point of peak power? Both of these questions may be answered by further experiments looking at electroburning as a function of pressure, under both an oxidative and inert environment. This may unveil a power-dependence and a threshold pressure for popping, with distinct activation energies if different mechanisms are at play, similar to those shown by El Abbassi *et al.* (80). This would help indicate whether the breakdown is a chemical or a thermal process: perhaps the gas acts as an important thermal pathway to cool the constriction during electroburning, slowing the thermal breakdown of the constriction enough to allow the feedback mechanism to prevent total breakdown. Furthermore, it is unknown to what extent the observed behaviours are a result of the particular feedback-controlled electroburning process here employed as opposed to feedback-less or pulsed electroburning processes employed by other authors (73, 75, 76, 121), as the aim of the feedback-control is to retard the breakdown mechanism. A second open question is whether, notwithstanding the degradation of the oxide, electroburning under H_2 creates clean hydrogen terminated graphene edges? In-situ Raman microscopy may be useful in identifying any change in edge chemistry (153). If the switching is due to an unfavourable interaction between the hydrogen and the SiO_2 substrate then this effect could be isolated by performing electroburning on different substrates such as Si_3N_4.

Untangling the processes occurring during electroburning of graphene constrictions with unknown com-

position is incredibly complex given the limited control over the structure and condition of the graphene. Further studies with exfoliated graphene may provide a clearer answer on the breakdown mechanism, however the patterning of the graphene into a narrow constriction suitable for electroburning without introducing contaminants or defects would be challenging (86, 154). One promising solution for addressing the desire for hydrogen termination and reproducible nanogap formation may lie in using hydrogen plasma to clean and etch the constrictions into nanogaps (153, 155–158). Combining hydrogen plasma etching of graphene constrictions with real-time electrical feedback may enable the precise creation of nanogaps with ideal edge chemistry.

The goal of this study was to examine the electroburning process and explore favourable conditions for the formation of graphene nanogaps suitable for molecular electronics experiments. While junctions formed under vacuum appeared promising at first, I found that they did not form molecular junctions using a well studied molecule. As such, I was not able to improve the yield of empty devices by changing the atmospheric conditions, but instead uncovered some of the uncertainties of the electroburning process.

Outlook

In this chapter we have explored how the electroburning process is affected by the atmospheric conditions under which it is performed. While making some interesting observations about the electroburning mechanism I was unable to convincingly boost the yield of electronically featureless nanogap devices suitable for molecular electronics. As such, my attention shifted to addresssing the second challenge raised in Chapter 1 by looking at methods to improve the yield of forming molecular junctions.

Chapter 3

Dielectrophoresis

Overview

In this chapter we will explore the phenomena of dielectrophoresis and how it can be employed in graphene nanogap devices in an effort to overcome the second major challenge highlighted in Chapter 1: that of the lack of control over bridging molecules across the nanogap. I will describe how dielectrophoresis can be used to direct the motion of particles in solution and how this technique has been used in previous works. I will show a computational model to quantify the trapping ability of our graphene nanogaps for the technique, and go on to show trapping experimentally using several different target particles, including molecules, highlighting some optimum trapping parameters. A portion of this work has been reported in (1).

3.1 Introduction

While single nanoparticles can be manipulated with high fidelity using techniques such as optical tweezers (159–161), viscoelastic stamping (162) and atomic force microscopy (163, 164), integrating nanoparticles into functional devices by placing them between electrodes reliably, facilely and at scale has remained a long-standing challenge (165). For molecules this challenge is even greater, and methods used to bridge molecules across nanogaps rely on stochastic processes such as drop-casting (166) which give poor yields. Yields may be boosted by engineering molecules to interact favourably with the electrodes (92) or with the substrate between the electrodes (167), however these modifications can significantly alter the electronic properties of the molecules themselves (168). One possible solution exists in the technique of dielectrophoresis, whereby particles are manipulated using non-uniform electric fields, which has been shown to enable the positioning and integration of nanoparticles into devices (169–186), and where there is emerging evidence of its applicability to the manipulation of molecules (177, 187–191).

In this chapter I will demonstrate how our atomically-sharp, nanometre-separated graphene electrodes can be used as precise dielectrophoretic traps to capture a variety of nanoparticles and molecules.

3.1.1 Theory

Dielectrophoresis (DEP) describes the force exerted on neutral but polarisable particles by gradients in non-uniform electric fields. This force depends on the particles volume V, the relation between the complex permittivities of the particle ε_p^* and the medium ε_m^* the particle is suspended in (typically liquid), and the square of the electric field gradient $\nabla|\mathbf{E}|^2$. Assuming the dipole approximation, the time-averaged DEP force can be expressed as (192):

$$\langle \mathbf{F}_{\mathrm{DEP}} \rangle = \frac{1}{4} V \, \varepsilon_m \, \mathrm{Re}\left\{K(\omega)\right\} \nabla|\mathbf{E}|^2 \tag{3.1}$$

Here, $\mathrm{Re}\left\{K(\omega)\right\}$ is the Clausius-Mossotti factor (CM) which describes a ratio between the complex permittivities of the particle and the medium. The form of $K(\omega)$ depends on the shape of the particle being trapped, where for a homogenous sphere $K(\omega) = (\varepsilon_p^* - \varepsilon_m^*)/(\varepsilon_p^* + 2\varepsilon_m^*)$. The complex permittivities carry a frequency dependence as $\varepsilon_j^* = \varepsilon_j - i\sigma_j/\omega$, and as such CM can take values between $-\frac{1}{2} \leq K(\omega) \leq 1$. Generally speaking, when the particle is more polarisable than the medium CM is positive and the force on the particle acts in the direction of the highest field gradient. This is known as positive dielectrophoresis (pDEP). Conversely, negative dielectrophoresis (nDEP) occurs when the particle is less polarisable than the medium and the force on the particle acts away from regions of high field gradient.

Non-uniform fields with field gradients large enough for DEP manipulation can be readily generated by applying electric potentials to sharp electrodes, across small distances or across boundaries between dielectric materials (193). AC fields are often employed to achieve high field strengths while avoiding electrolysis reactions and unwanted Faradaic currents within the medium that occur under DC potentials.

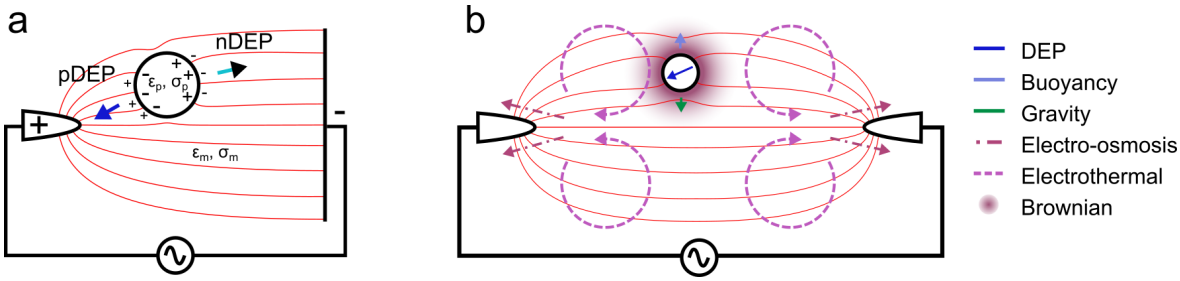


Figure 3.1: Schematic representations of (a) a polarisable particle experiencing positive (pDEP) or negative (nDEP) dielectrophoresis within a non-uniform electric field and (b) competing forces acting on the particle and the medium.

When using DEP to manipulate small particles one must consider other competing forces which act on suspended particles, in order to determine if the DEP force will be sufficient to overcome them (192, 194, 195). Figure 3.1 shows a graphical representation of some of these other forces. In addition to DEP, buoyancy and gravity will give large contributions to the motion of large particles, while the application of electric fields across a media with finite conductivity will generate electro-osmotic forces on the ions in the double-layer at the electrode-medium interface and electrothermal flows in the fluid body as Joule heating creates small

temperature and permittivity gradients, inducing large convective fluid motion. Finally, for small particles random Brownian motion becomes a significant barrier to controlling their movement.

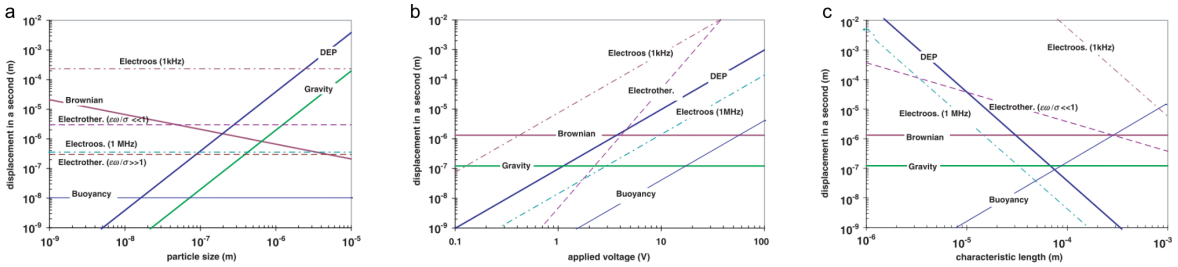


Figure 3.2: The scaling of positive dielectrophoresis and competing forces on the displacement of a particle in 1 s as a function of (a) particle radius, a, (b) the applied voltage, V and (c) the characteristic length, r in a solution of low conductivity $\sigma = 0.01$ Sm^{-1}. The force relationships are calculated considering model system consisting of a pair of co-planar strip electrodes, where the characteristic length describes the inter-electrode separation. For (a) $V = 5$ V, $r = 25\,\mu$m, (b) $a = 0.25\,\mu$m, $r = 25\,\mu$m and (c) $V = 5$ V, $a = 0.25\,\mu$m. Figures are reproduced from (196).

Figure 3.2a shows how these forces scale with particle size. As we reach the nanoscale, the magnitude of the DEP force rapidly decreases while the influence of Brownian motion increases significantly. Applying larger voltages to boost the field gradients and therefore the DEP force (Figure 3.2b) allows one to overcome Brownian motion, but quickly this gain is overtaken by the scaling impact of electro-osmotic and electrothermal flows with voltage. Instead of increasing the applied voltage, by decreasing the characteristic length of the system - the separation between the electrodes - the DEP force can be made to dominate all other competing forces and flows (see Figure 3.2c) (196). This is particularly true if high frequency (MHz) AC voltages are used as the magnitude of the electro-osmotic force is much reduced at high frequencies as the double layer does not have sufficient time to respond to the changing potential landscape. Therefore, in order to maximise $\nabla|\mathbf{E}|^2$ for the manipulation of small particles, electrodes with nanoscale dimensions are particularly advantageous.

3.1.2 Device design

Metal electrodes are the most common choice when designing dielectrophoretic devices and several authors have shown how nanoscale metal electrodes can be used to achieve single particle capture (169, 170, 197, 198). However, metallic electrodes stable enough for dielectrophoresis and are largely limited to separations achievable with lithographic patterning (171, 176, 178, 197), which then limits the size of particles that can be captured and *contacted* across both electrodes.

Recent works have employed atomic layer deposition and 2D materials, such as graphene, to create stable and scalable nanoscale devices capable of manipulating particles at very low voltages (177, 188, 191, 199–201). Graphene in particular is an ideal electrode material for dielectrophoretic devices owing to its high conductivity and atomic sharpness, allowing for the trapping and integration of various nanoparticles into conductive electrical devices (183, 185, 188, 202). However, Barik *et al.* showed that while graphene gives an enhanced field gradient close to the electrode, as one moves away from the electrode into the medium

the magnitude of the field gradient falls off more rapidly than for an equivalent metallic electrode, which they attribute to graphene's small density of states (188). This apparent weakness of graphene for long-range DEP trapping applications may in fact be an advantage when the goal is to trap individual nanoparticles from a relatively concentrated and freely diffusing suspension. In addition, graphene has many appealing qualities as an electrode material such as a gate-tunable carrier concentration, optical transparency, plasmonic activity (203) and long spin-diffusion lengths (204), which make it attractive for applications such as biosensing (205) and spintronics (206). As such, our graphene nanogap devices appear to be ideal platforms for dielectrophoretic trapping, as I will go on to show in the remainder of this chapter.

3.2 Modelling

In order to better understand the capability of our graphene nanogap devices for dielectrophoresis I employed finite element modelling using COMSOL Multiphysics 5.5 to map the field gradients generated around the nanogap. I used the electric currents interface from the AC/DC physics module which computes electric fields and potential distributions for conducting media where inductive effects can be neglected.

In this interface Poisson's equation is expressed as:

$$\nabla \cdot \mathbf{J} = Q = -\frac{\partial \rho}{\partial t} \tag{3.2}$$

$$\mathbf{J} = \sigma \mathbf{E} + j\omega \mathbf{D} \tag{3.3}$$

$$\mathbf{E} = -\nabla \varphi \tag{3.4}$$

Where, within any one element, $\mathbf{J}$ is the current density, Q is the charge, ρ is the electric charge density and t is time, σ the conductivity, $\mathbf{E}$ is the electric field, ω is the frequency of the electric field, $\mathbf{D}$ is the electric displacement field and φ is the electric potential.

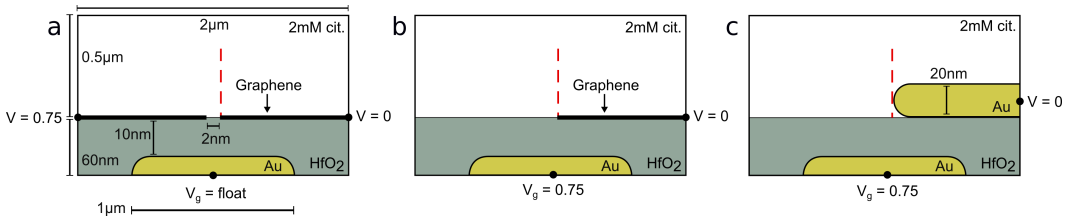


Figure 3.3: Schematics of the geometries used for electric field calculations for: (a) A 2 nm graphene nanogap with a floating buried gate, (b) a single graphene electrode trapping against a buried gate and (c) a 20 nm gold electrode trapping against a buried gate.

A 2D simulation of a cross section of a locally gated graphene nanogap was built to scale as shown in Figure 3.3a. The simulation domain was 2 μm wide by 0.56 μm high, centred around the nanogap in the x-direction.

The nanogap was set as 2 nm wide, sitting on top of a 10 nm layer of HfO_2 dielectric which further encased a rounded local gate electrode below. In this model, the medium was assumed to be an aqueous solution with a permittivity of $80\varepsilon_0$ and a conductivity of 600 μS cm^{-1}, as was the case for the gold nanoparticles suspended in a 2 mM citrate solution discussed in §3.3.2. The 10 nm thick HfO_2 was assigned a permittivity of 13 (207) and a negligible conductivity. Dirichlet boundary conditions of $\varphi = 0.75$ V and $\varphi = 0$ V were set on the left and right vertices of the 1D graphene layer at the edges of the simulation domain, respectively. The buried gate electrode was assigned a 'floating potential' boundary condition. All other external boundaries were set to the insulating Neumann boundary condition $\mathbf{n} \cdot \mathbf{J} = 0$. The graphene was defined as a 1D layer with a dielectric shielding boundary condition whereby:

$$\mathbf{n} \cdot (\mathbf{J}_1 - \mathbf{J}_2) = -\nabla_T \cdot d_s d((\sigma + j\omega\varepsilon_0\varepsilon_r)\nabla_T\varphi) \tag{3.5}$$

where $\mathbf{n}$ is the normal vector, $\mathbf{J}_{1,2}$ are the current densities on either side of the boundary, ∇_T is the tangential differential and d_s is the thickness of the boundary which was set as 1 nm. I used $\varepsilon_r = 6.9$ (208) and set the conductivity as $\sigma = e\mu_e\, n_{2D}(\varphi(x))$, where μ_e is the electron mobility in graphene (2.5×10^4 cm^{2}V^{-1}s^{-1} (209)) and n_{2D} is the surface charge concentration per unit area. This was defined according to the analytical expression presented by Barik *et al.* (188):

$$n_{2D}(\varphi(x)) = 2\frac{\Gamma(2)}{\pi}\left(\frac{k_B T}{\hbar v_F}\right)^2 \left[\mathcal{F}_1\left(\frac{e\varphi(x)}{k_B T}\right) - \mathcal{F}_1\left(\frac{-e\varphi(x)}{k_B T}\right)\right] \tag{3.6}$$

where v_F is the Fermi velocity (10^6 ms^{-1} in graphene), $\varphi(x)$ is the electric potential at position x along the graphene layer and $\mathcal{F}_1$ is the Fermi-Dirac integral of order 1:

$$\mathcal{F}_j(\eta) \equiv \frac{1}{\Gamma(j+1)} \int_0^\infty \frac{\epsilon^j d\epsilon}{e^{\epsilon-\eta} + 1} \tag{3.7}$$

where $\Gamma(n) = (n-1)!$ (210). $n_{2D}(x)$ was calculated in MATLAB using the algorithm published by Wang and Lundstrom (211), and the results were implemented into the COMSOL simulation in a self-consistent calculation for φ. The low solution conductivity combined with the low trapping voltages used means that we can neglect any effects of Joule heating of the solution (191). The model was solved in the frequency domain at $\omega = 1$ MHz, allowing us to also discount electro-osmotic forces.

To compare the effectiveness of our graphene nanogaps versus competing trapping architectures between single electrodes and a local buried gate (188) I calculated the field gradients in two further configurations shown in Figure 3.3b, for a single graphene electrode and 3.3c, for a single 20 nm thick gold electrode with rounded edges (the gold was assigned a conductivity of 4.6×10^7 S cm^{-1} (212) and a permittivity of 1). Within a finite element model any field gradient will tend to infinity at the boundary between the field source and the rest of the domain, with gradients only increasing as the size of the model elements, or mesh, are reduced. This problem is exacerbated when modelling 1D materials. Therefore, we must exclude the values calculated

at the boundary from our results but can approach arbitrarily close by selecting appropriate mesh sizes for the modelled features. In this case, we set a maximum mesh size of 0.1 nm around the nanogap in order to capture the field gradient on a scale relevant to target nanoparticles. The mesh size was increased with distance from the nanogap for the rest of the domain to reduce the computational load.

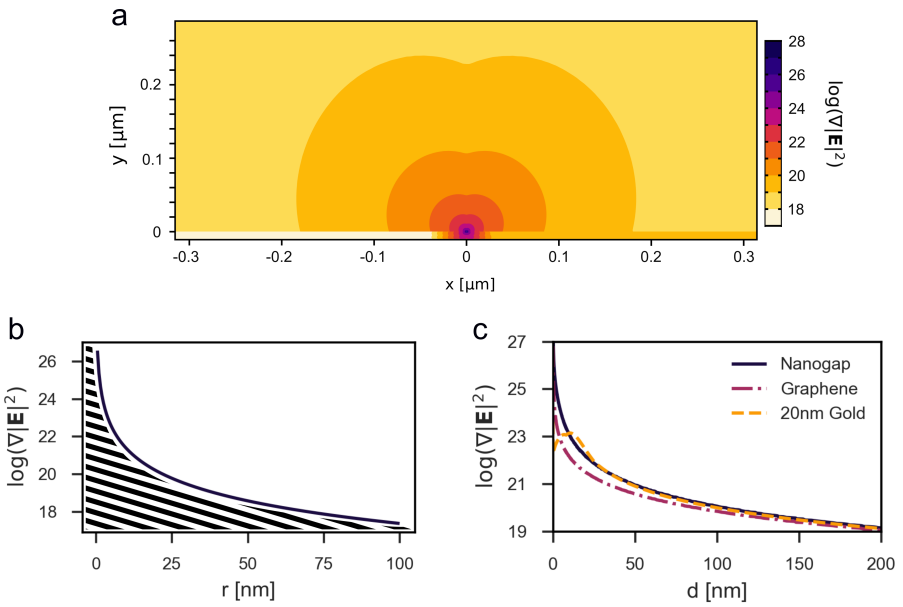


Figure 3.4: (a) A contour plot of the field gradient generated about a 2 nm graphene nanogap under a 0.75 V_p bias at 1 MHz. (b) A graphical representation of Eq. 3.9. (c) Line plots of the field gradient along the red dashed lines in Figure 3.3 for the three electrode types.

Figure 3.4a shows a contour plot of the logarithm of the field gradient calculated around a graphene nanogap device with a floating local gate. Figure 3.4c shows a comparison between the results of the three configurations shown in Figure 3.3, with field gradients extracted along the path of the red dashed lines up to the electrode edges. From this plot we see that at distances more than 100 nm from the electrode edges all three configurations behave similarly. Approaching the edge, the gradient around the gold electrode pulls ahead of the single graphene electrode before reaching a maximum at approximately 10 nm from the substrate, as a result of the curvature. Approaching the dielectric boundary closer, the single graphene electrode pulls ahead in terms of absolute magnitude of the field gradient but over a much smaller volume, limiting its ability to be a superior trap for particles until they are only a few nanometres away from the edge. For the graphene nanogap however we see that the field gradient keeps pace with that generated around the gold electrode and then exceeds it after the gold electrode reaches its maximum. This result indicates that our graphene nanogap devices should prove superior to these alternative architectures.

In order to place the calculated field gradients in context we can consider the gradient required to trap against the most significant competing force considering our choice of sub-volt potentials and MHz frequency: Brownian motion. A particle of volume V experiences an approximate thermal force of:

$$F_{\mathrm{T}} \approx \frac{k_B T}{V^{1/3}} \tag{3.8}$$

where k_B is the Boltzmann constant and T the temperature of the solution. By equating (3.1) and (3.8) we can obtain an expression for the field gradient required to overcome thermal forces:

$$\nabla|\mathbf{E}|^2 > \frac{4k_B T}{\varepsilon_m V^{4/3}} \tag{3.9}$$

This relationship is plotted as a function of particle radius $r = \sqrt[3]{V}$ in Figure 3.4b. From this relationship we can estimate that the field gradient required to trap a particle with a 10 nm radius is about 1×10^{22} $\mathrm{V^2m^{-3}}$. At a trapping voltage of 0.75 V_p this gives a trapping region which extends about 25 nm from the nanogap. Clearly, for such a small volume the trapping will be diffusion limited at this voltage, however, as I will show this is in fact an advantage when attempting to capture single particles from a relatively concentrated solution.

3.3 Experimental

With the knowledge that our nanogaps are capable of generating field gradients to trap nanoscale particles I was interested in exploring the different types of particles that I could trap. For the experimental work I used a combination of local and globally gated devices with different electrode geometries depending on the technique used, the nature of the particles and the ultimate goal of the experiment. The subsequent sections detail experiments undertaken using a range of particle types.

3.3.1 Latex beads and DNA

To understand the trapping behaviour it would be advantageous to observe the trapping in real time using optical microscopy. I collaborated with B.P. Nadappuram from the Edel group at Imperial College London to take advantage of their expertise in microscopy and dielectrophoretic trapping (188, 191, 213). While optical microscopy experiments are limited to resolving features larger than the diffraction limit (~ 200 nm), by using fluorescence microscopy we could observe the movement of fluorescently tagged particles as they diffused around our devices and were acted upon by the dielectrophoretic trapping voltage (213).

In order to perform these experiments chips with long finger electrodes were prepared with electroburned graphene nanogaps in the manner described in Chapter 1. These chips were mounted onto and wire-bonded to a custom PCB, which gave access to each device (see Annex II). A 150 μm thick spacer with a central hole cut-out was adhered to the surface of the chip and a dilute solution of target particles was deposited inside this well. A thin 300 μm glass slide was then placed on top of the spacer, sealing in the solution. This setup, represented in Figure 3.5a, prevented the solution from evaporating and ensured that the chip was in the focal range of the high numerical aperture water-immersion objective. The chip was then mounted upside down in

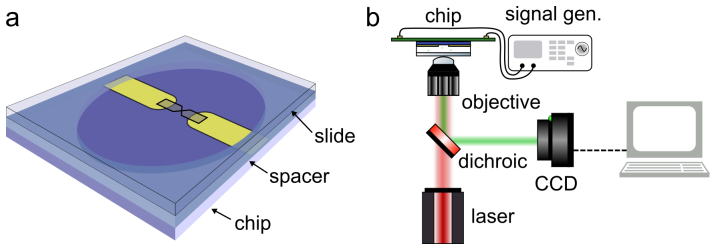


Figure 3.5: (a) A representation of the devices used in the optical experiments. Chips with finger electrodes and graphene nanogaps were covered with a thin spacer with a cut-out around the devices in which we deposited a dilute solution of target particles. A thin glass slide was then adhered to the spacer encapsulating the solution on top of the devices. (b) A schematic of the microscopy setup. The chip was mounted upside-down on and wire-bonded to a PCB which was connected to a signal generator to generate the trapping signals. A 60× water immersion objective was brought into contact with the chip, which was illuminated from behind through a cut-out in the PCB (enough light could pass through the silicon substrate to observe the electrodes). Particles labelled with YOYO-1 dye were illuminated using a 488 nm fibre-coupled tunable argon ion laser, and the fluorescence was directed to an electron multiplying CCD camera. The CCD camera had a pixel size of 16 mm giving a final effective pixel size of 266 nm when used with the 60× objective (191, 213).

an XY stage and the objective was brought into contact and focussed on a single device. A range of trapping parameters were tested using a signal generator from a few kHz up to 10 MHz and with voltages from 0.5 to 5 Volts. The experiments were monitored in real time using a CCD camera and the video files were stored on a PC.

We first tried trapping 2 μm diameter latex beads tagged with the YOYO-1 fluorophore suspended in de-ionised water. Figure 3.6 shows a series of frames taken from a video trapping these beads using a trapping voltage of 1 V_p at a frequency of 800 kHz. Starting from the first frame, we see that a latex bead has already become trapped at the nanogap showing us that in this case the nanogap has formed away from the patterned constriction, likely due to a tear in the graphene. We see how a freely diffusing bead probes the volume around the nanogap, drifting in and out of the focal plane until, in the penultimate frame, it is suddenly captured and pulled into the nanogap region where it remains fixed. Knowing that, for these remote electrode devices, the gold electrodes are separated by 17 μm, we observe that the trapping radius extends out approximately 2.3 μm from the nanogap. According to Eq. 3.9 a particle with a radius of 1 μm would require trapping potentials in excess of 3×10^{12} V^2m^{-3} to overcome Brownian motion, which we know is in easy reach for our devices. These videos were taken at 30 frames per second, with each frame representing about 33 ms.

Figure 3.7 shows the results of the next set of experiments where we attempted to trap pieces of DNA 500 base pairs long: approximately 150 nm. As these molecules were much smaller than the latex beads they had far fewer fluorophores attached and as such would quickly photobleach under laser irradiation. This made it harder to test multiple trapping parameters however we were able to successfully trap these molecules with the application of a 2 V_p voltage at 5 MHz frequency. We see in the Figure how one DNA piece diffuses around the nanogap over a long period of time, approaching the nanogap closely without being captured. Eventually, in frame 118 the particle crosses the trapping threshold and is immobilised at the nanogap as seen in frame 119. The particle does not move from this position during the remainder of the experiment. From this video

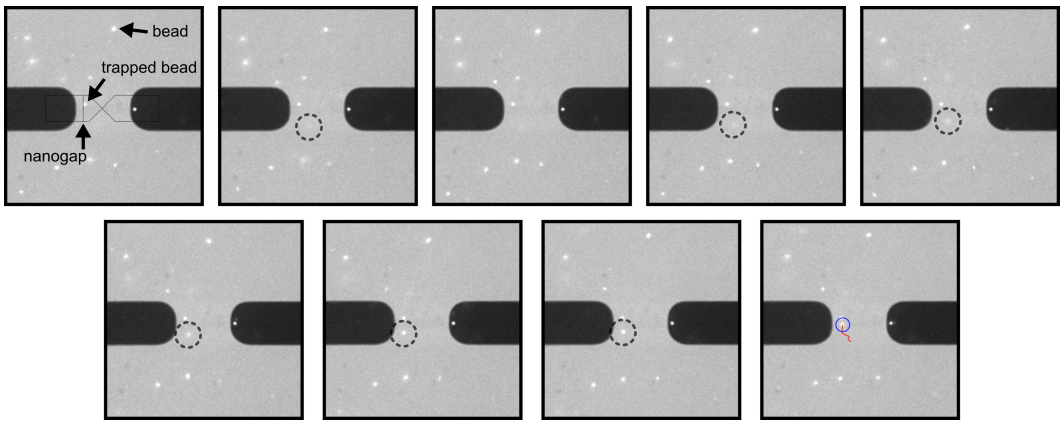


Figure 3.6: Still frames extracted from a video showing trapping of 2 μm diameter latex beads in de-ionised water under a 2 V 100 kHz potential. The light spots a fluorescent beads while the dark areas are the gold finger electrodes. The graphene constriction sits between the finger electrodes, with an outline shown in the first frame. In these devices the nanogap has formed to the left of the constriction centre, as labelled. Each sequential frame represents approximately 33 ms. A dashed circle highlights the position of the latex bead which will be trapped. In the final frame the red line traces the motion of the particle across the previous frames and the blue circle traces the approximate trapping radius.

it is not possible to obtain an estimate for the trapping radius other than noting it must be less than 1 μm.

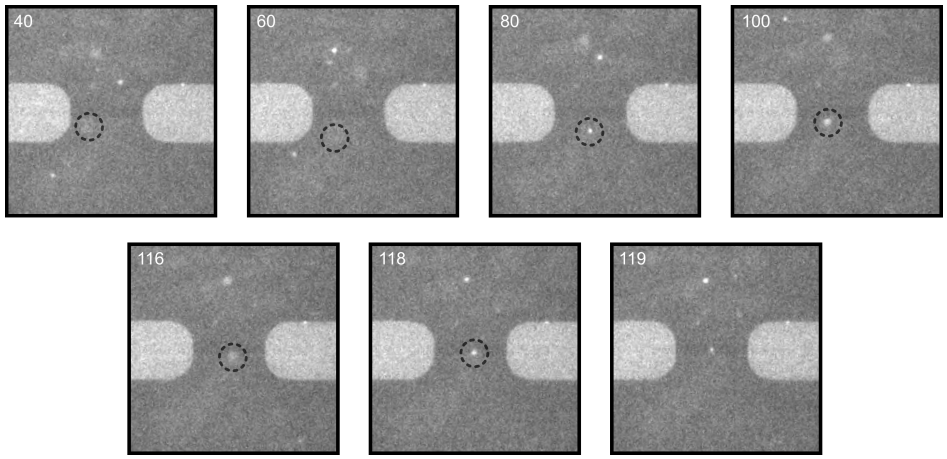


Figure 3.7: Still frames extracted from a video showing trapping of 500 bp DNA in de-ionised water under a 1 V_p 5 MHz potential. Here, a selection of frames are chosen to show the motion of the DNA over a longer time period. Each frame is labelled with its frame number where each frame represents ~ 33 ms. The trapping occurs between frames 118 and 119.

These experiments show that our devices are very capable of trapping single particles at low voltages, albeit being limited by diffusion of the particles into a small trapping region, as expected from our model. However, for the trapping of single particles this diffusion limit is advantageous in preventing large aggregations of particles being captured.

3.3.2 Gold nanoparticles

Having demonstrated the capture of nanoscale pieces of DNA I was interested in whether I could trap even smaller inorganic nanoparticles which could then be studied in electrical transport measurements. Testing the

trapping of smaller nanoparticles required a change of method: optical microscopy lacked sufficient resolution and the devices would need to be dried after trapping to perform electrical measurements. I turned to gold nanoparticles as a test particle given their stability, ease of handling and high conductivity. The particles selected for this purpose were 60 × 15 nm gold nanorods in a 2 mM aqueous citrate solution acquired from nanoComposix. These nanoparticles would be resolvable within our SEM and their aspect ratio would give me information on their orientation. I also altered my device design as I no longer required long finger electrodes and would benefit from the presence of a local gate electrode in the transport measurements. A representation of the device geometry is shown in Figure 3.8a, the fabrication of which will be outline in more detail in Chapter 4.

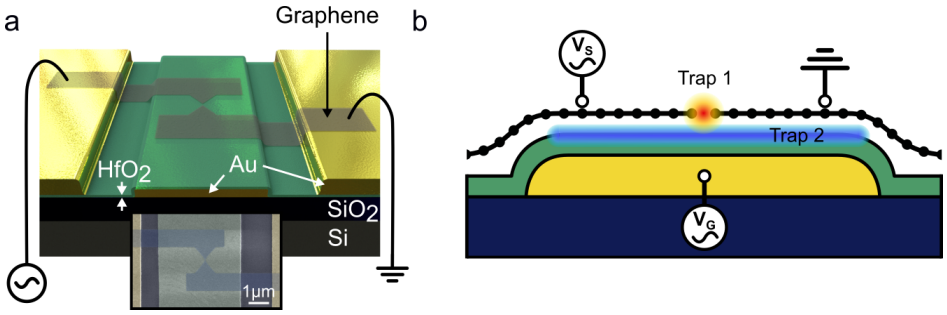


Figure 3.8: (a) A graphic representation of the device architecture. The graphene is transferred and patterned on top of a 10 nm layer of HfO_2 which conformally covers the local gold gate electrode. The inset shows a false-colour SEM image of a real device. (b) A diagram showing the difference between trapping at the nanogap (Trap 1) and between the graphene edge and the local gate (Trap 2). All trapping was performed at 1 MHz for 30 seconds.

Trapping was performed by depositing 2 μL of nanoparticle solution (containing $\approx 2 \times 10^8$ nanoparticles) onto a chip prepared with electroburned nanogaps. The chips had been bonded to a custom 44 pin PCB which was mounted in a custom break-out box and connected to a function generator (see Annex II). This allowed for devices to be addressed individually or in parallel, where the trapping voltage could be applied to the source, drain or local gate electrodes, and for excess solution to be washed off the surface of the chip afterwards. Once the solution was deposited, the trapping signal would been applied for a set amount of time to all devices that were being tested with the same parameters. The stability of the solution meant that multiple experiments could be performed sequentially, limited only by the number of devices (~22 per experimental run). After trapping, the PCB was disconnected from the break-out box and the remaining nanoparticle solution was washed off with de-ionised water. The chips on the PCBs were dried under nitrogen and were then imaged in an SEM to observe the outcome of the trapping.

The local-gate device architecture of the chips allowed me to explore several trapping configurations. A trap could be created both across the nanogap (Trap 1) and between the graphene electrodes and the local gate electrode (Trap 2), as shown in Figure 3.8b and as discussed in §3.2. While the nanogap generates the largest magnitude field gradients due to the smaller electrode separation, trapping between the graphene and the gate electrode still offers an effective dielectrophoretic trap which extends along the whole edge of the

graphene.

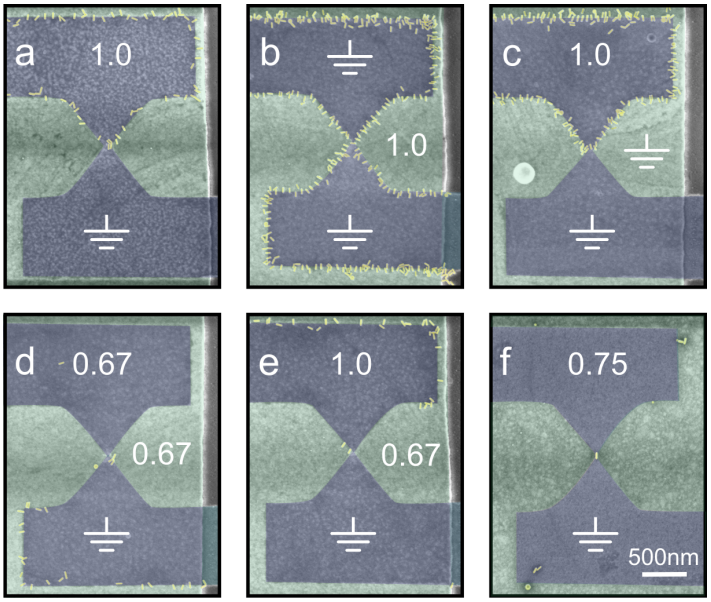


Figure 3.9: False-coloured SEM images of the effects of trapping gold nanoparticles using various trapping configurations. The two graphene electrodes are biased with the labelled peak voltages (V_p) or are grounded. Where the local gate is not labelled it has been floated.

Figure 3.9 shows the outcome of trapping under various voltages and configurations, while the frequency was set at 1 MHz and the potential was applied for 30 s. For metallic nanoparticles $K(\omega)$ can be assumed to be equal to +1 and the nanoparticles experience positive dielectrophoresis across all experimental frequencies (214, 215). I found that trapping with the local gate (Figure 3.9b) resulted in many more nanoparticles being captured than when trapping across the nanogap using the same voltage while the local gate was floated (Figure 3.9a). However, trapping using the local gate resulted in a loss of site-selectivity and the field gradient appeared to be screened by the electrodes around the nanogap. If instead I grounded the local gate I observed that nanogap site-selectivity was also lost as the trap generated at the edges of electrode out-competed the trapping across the nanogap (Figure 3.9c). Applying smaller in-phase AC voltages of 0.67 V_p to both the local gate and across the nanogap also lead to the local gate dominating over nanogap, while the overall number of nanoparticles captured was significantly reduced (Figure 3.9d). Applying a larger potential across the nanogap than that applied to the local gate does achieve better site selectivity (Figure 3.9e), however I found that the optimal trapping configuration was to apply a voltage of 0.75 V_p across only the nanogap while the local gate electrode was allowed to float (Figure 3.9f). Such a configuration allowed me to achieve single particle capture where, for one chip, 66% (26/39) of the tested nanogaps were found to have captured nanoparticles, of which 35% (9/26) achieved single particle capture. Figure 3.10 shows three further examples of nanoparticles captured under these conditions. In all cases, we see some preference for the nanoparticles to align with the electric field lines, but this effect is not particularly strong.

To better understand these observations, we can turn back to the model developed in §3.2. For nanoparticles of an equivalent radius to our nanorods, using Eq. (3.9) we would expect that gradients in excess of

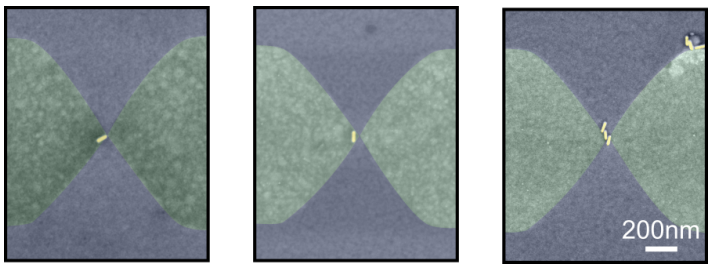


Figure 3.10: False-colour SEM images of three further devices created using the optimum parameters of 0.75 V_p at 1 MHz for 30 seconds.

$1 \times 10^{19}\,V^2m^{-3}$ would be necessary for trapping. From Figure 3.4c we see that this condition is met within about a 200 nm radius around the nanogap. Figure 3.11 shows the calculated field gradient generated about a 2D cross section of the local gate architecture true to experimental dimensions, where in this model I have captured the full extent of the graphene and local gate electrodes. Figure 3.11a shows the field gradients generated using a trapping voltage of 1 V_p applied across the nanogap while the local gate is treated as a floating potential. The black countours indicate where the field gradient reaches $1 \times 10^{19}\,V^2m^{-3}$. We can see that the largest trapping region is generated around the nanogap while sizeable trapping volumes exist at the outer graphene edge due to the confinement of the electric field by the local gate. We can also see that small trapping volumes are found at the edges of the local gate electrodes under the dielectric layer. Figure 3.11b shows the result of a 3D model capturing the full device geometry. The iso-surface shown is that where the field gradient is equal to $1 \times 10^{19}\,V^2m^{-3}$. In Figure 3.11c we see the result of applying the trapping voltage to the local gate electrode while the graphene electrodes are both grounded. A large trapping volume is generated at the outer graphene edge while we see that at the nanogap the field gradient is heavily screened by the graphene electrodes, reproducing what I observed experimentally in Figure 3.9b. Finally, Figure 3.11d shows the gradients generated in a device without a local gate electrode and a SiO_2 substrate where the trapping potential is applied across the nanogap. Here, the central trapping volume is equivalent in size to that in Figure 3.11a, with only a small volume generated at the outer edges of the graphene due to its atomic sharpness.

Having achieved the capture of single nanoparticles across our graphene nanogaps the transport properties of these devices will be explored in detail in Chapter 4. This study also paved the way for trapping and electrical transport studies of 25 nm magnetite nanoparticles which is discussed in detail in Chapter 5.

3.3.3 Molecules

Ultimately, the aim of the exploration of dielectrophoresis was to be able to direct the formation of molecular devices like those discussed in Chapter 1. Exploring the trapping of molecules is particularly challenging, however, as monitoring their movement would require complex optical instrumentation (216) and evaluating the structure of the final device would require advanced scanning probe techniques (217). Nonetheless, with the tools available I performed several experiments to explore the applicability of this technique to molecules.

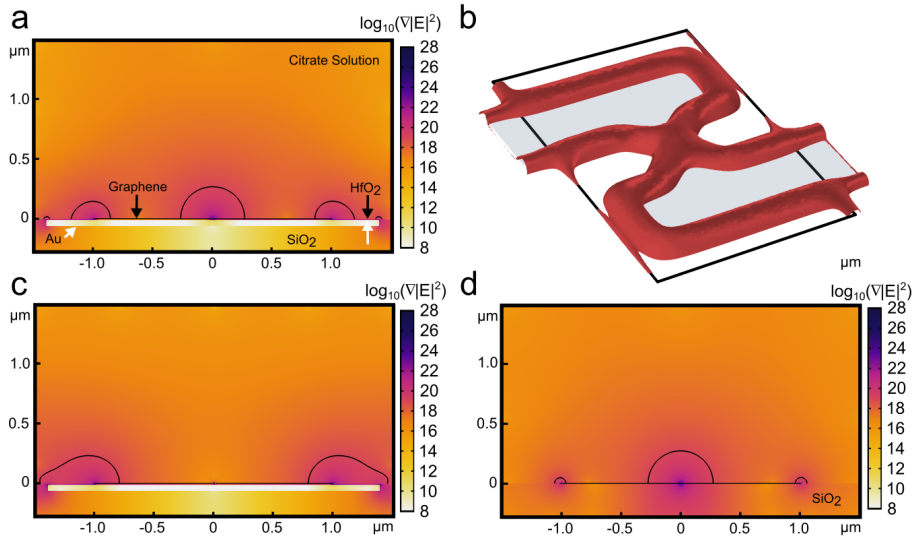


Figure 3.11: Finite element calculations of the field gradient generated around (a) a 2 nm graphene nanogaps using the parameters 1 V_p at 1 MHz while the local gate is floated, (c) a graphene nanogap where the trapping potential (1 V_p at 1 MHz) is applied to the local gate and the graphene electrodes are grounded and (d) a graphene nanogap using the optimum parameters in the absence of a local gate electrode. These plots are shown on a logarithmic scale where the black contour shows where $\nabla|\mathbf{E}|^2 = 1 \times 10^{19}\,\mathrm{V^2m^{-3}}$. (b) A 3D iso-surface of $\nabla|\mathbf{E}|^2 = 1 \times 10^{19}\,\mathrm{V^2m^{-3}}$ calculated for a 3D model of the device architecture shown in Figure 3.8a under a the same parameters as in (a). Here, the graphene was treated as a simple 1D gold electrode to reduce the computational load. The black border shows the footprint of the buried local gate electrode while the grey shaded areas represent the graphene electrodes.

For an initial target molecule I again chose the zinc-porphyrin-based molecules funtionalised with pyrene anchor groups used in Chapter 2 which were known to give a high junction formation probability (92). The structure of this monomer is shown in Figure 3.12a.

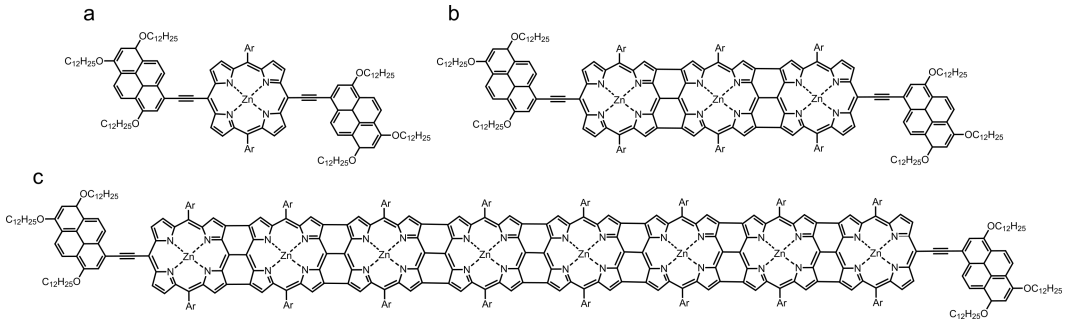


Figure 3.12: Molecular structures of (a) a zinc-porphyrin monomer with pyrene anchor groups, (b) a zinc-porphyrin fused trimer with pyrene anchor groups and (c) a zinc-porphyrin fused octomer with pyrene anchor groups. Theses molecules were synthesised by colleagues in the H.L. Anderson group in Oxford (92, 218).

Considering the size of the molecules (< 3 nm), dielectrophoresis was first attempted using a high voltage of 3 V_p at a frequency of 10 kHz as the polarizability of the monomer was unknown. At such voltages I was hoping to observe some aggregation of molecules around the nanogap but did not expect the tunnel junctions themselves to survive. I again used devices with finger-like electrodes mounted in my custom break-out box so that I could apply the trapping voltage to all devices simultaneously, as once the 3 μM molecular solution was deposited the toluene solvent would rapidly evaporate. The results of this study are shown in Figure 3.13b.

As shown, an optical image of the nanogap taken after trapping shows a faint green spot at the constriction: the same colour as the porphyrins in solution. In the SEM we see that an aggregate of molecules has formed around the nanogap with a coffee ring-like structure on the substrate. Figure 3.13c shows a similar result for a device where the trapping parameters were set to 3.5 V_p at 1 MHz. Despite the apparent success, an immediate concern was that the aggregation could be formed from other contaminants or by the breakdown of the graphene electrodes instead of molecules. Figure 3.13a shows the results of a control experiment where the same trapping process was repeated using a solution of pure toluene. I found no green spot under the optical microscope and in the SEM I saw no aggregate. I did, however, clearly resolve the inter-electrode spacing indicating that the high trapping voltage has resulted in a significant widening of the nanogap. Indeed, for all devices tested with pure toluene at high voltages no measurable tunnel current was detected afterwards. When using the molecular solution I observed two devices in which their conductivity significantly increased after trapping. These devices were later found to have aggregates at the nanogap, suggesting a conductive pathway had been established through the aggregate, but this finding was not reproduced in subsequent devices.

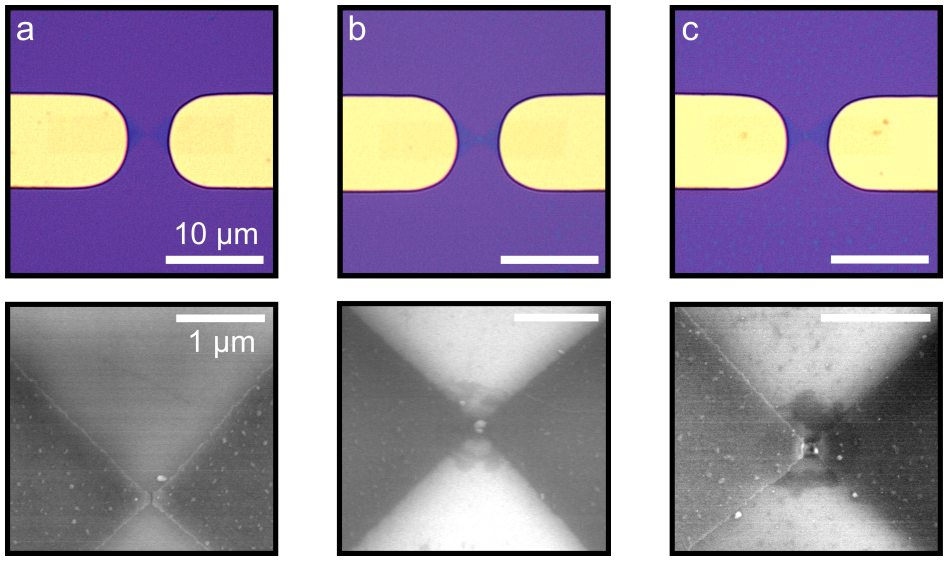


Figure 3.13: Optical (top) and SEM (bottom) images of graphene nanogaps after trapping in (a) pure toluene at 3 V_p, (b) porphyrin monomer in toluene at 3 V_p and (c) porphyrin monomer in toluene at 3.5 V_p at 1 MHz.

These results suggest that at large ($\sim$ 3 V_p) voltages it is possible to trap small molecules at using graphene nanogaps, however, whether these molecules are damaged in the process remains unknown. It may be possible that the conductivity observed in two devices after molecular capture was infact caused by the breakdown of the molecular aggregate under the large voltages to form a conductive amorphous carbon bridge. In order to explore trapping at lower voltages I turned to electrical detection using a lock-in amplifier, following the methods outlined in (219), hoping to observe a response in when molecules bridged the nanogap. Unfortunately, I quickly discovered that the baseline noise level in our graphene nanogaps was far too high to be able to distinguish any molecular event from background charge fluctuations (144), even at sub-volt potentials,

and so this could not be pursued further.

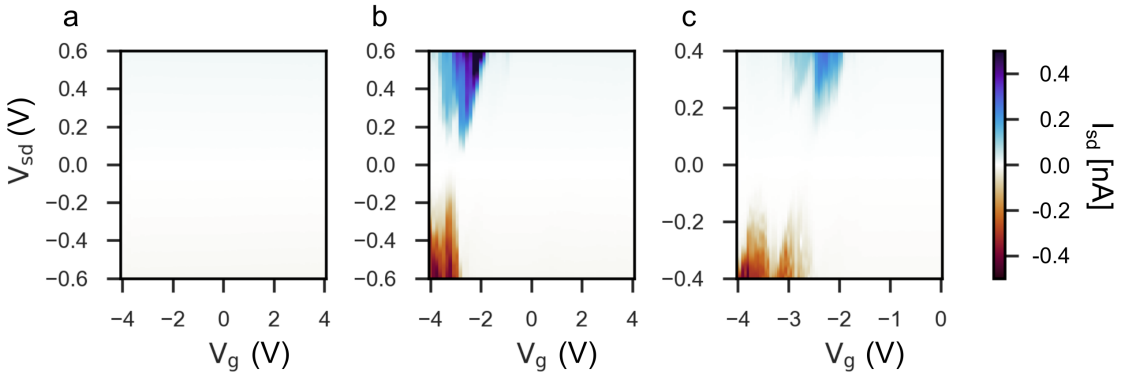


Figure 3.14: Stability diagrams measured at 77 K (a) after electroburning and (b) after trapping porphyrin octomers under 0.75 V_p at 1 MHz. (c) A higher resolution measurement over a smaller window of the features seen in (b).

With these limits in mind I attempted to monitor the formation of molecular devices following the methodology outlined in Chapter 1: measuring stability diagrams before and after molecular deposition. Using a more modest trapping voltage of 0.75 V_p at 1 MHz and longer 'fused trimer' porphyrin molecules, shown in Figure 3.12b, I observed no change the stability diagrams measured for any of the tested devices, suggesting that either the applied potentials were too small to capture small molecules, that captured molecules were not forming good electrical connections with the electrodes or that the trapping voltages were causing the nanogaps to expand beyond the length of the molecules. Later, the end of my project, I attempted this same experiment with the same parameters using a newly synthesised fused-porphyrin octomer, shown in Figure 3.12c, which were longer (~ 8 nm) and should be more polarisable than the monomer or the fused trimer. This time, despite a limited sample size and a low yield of featureless nanogaps I did observe a significant change in one device, shown in Figure 3.14. This device did not exhibit a clean Coulomb blockade, making it difficult to interpret, particularly in the absence of other octomer devices against which it could be compared. This device does, however, indicate that there is promise for using dielectrophoresis to trap molecules with our devices, and adds to a growing body of evidence on this topic (177, 187–191, 220).

3.4 Conclusion

In this chapter we have explored how the technique of dielectrophoresis can be applied to our graphene nanogap platform to capture a range of nanoparticles. I have demonstrated how nanoparticles and molecules can be directed into the nanogap with the application of modest potentials. Using optical microscopy I have observed the highly localised trapping of large bio-molecules and using SEM I have optimised the trapping conditions to boost the yield of single nanoparticle capture. I have shown tantalising evidence that dielectrophoresis may be applicable to the capture and formation of molecular devices owing to the high field gradients that can be generated around the nanogap. Further experiments with larger molecules like the porphyrin

octomer are needed confirm this capability, creating more devices using dielectrophoresis and studying their low temperature transport behaviour. Additionally, a comparison between devices formed through dielectrophoresis and conventional drop-casting would be needed to verify whether the applied potentials have caused any chemical changes to the molecules, which should manifest as differences in the charge transport. Efforts to optimise the trapping parameters would also prove valuable, however with the current methodology a large number of devices would need to be created to generate reliable statistics. As for nanoparticles, the work in this chapter highlights a ready route to the creation of hybrid graphene-nanoparticle-graphene devices which we will explore further in the following chapters.

Outlook

In this chapter I have demonstrated the dielectrophoretic trapping capability of our graphene nanogaps by trapping a variety of nanoparticles, optimising the trapping parameters for gold nanoparticles and creating a finite elment model to map the generated field gradients. I have shown evidence of the ability to trap of small molecules using our nanogap devices, however, this result requires further verification and experiments to confirm whether it is suitable for creating molecular devices. As such, and given the observed ability to trap single nanoparticles, in the subsequent chapters I will focus on the electrical transport properties of nanoparticle devices created using the methodology developed in this chapter.

Chapter 4

Gold nanoparticles

Overview

In this chapter we will build on the results in the previous chapter by exploring the electrical transport properties of devices formed from single gold nanoparticles using the technique of dielectrophoresis. I will discuss the interest in nanoparticle devices and some of the physics that governs their transport before outlining my efforts to establish a conductive pathway through the nanoparticle after capture and explore the devices' transport properties at low temperatures. I will then give a discussion on how we can be confident that we are measuring devices formed from gold nanoparticles before discussing some limitations and directions for future research which this work has highlighted. A portion of this work has been reported in (1).

4.1 Introduction

An abundance of unique and interesting nanoparticles (NPs) can now be synthesised and functionalised with impressive chemical control such as graphene nanoribbons (221), 2D transition-metal dichalcogenide crystals (222) and heterostructured nanoparticles (223, 224). Devices formed from single NPs have shown promise for applications such as nanoscale light sources (177, 197, 198, 225–229), spintronic devices (183, 230, 231), plasmonics (226–228) and bio-sensing (213, 220, 232–235). Furthermore, creating hybrid graphene-NP devices has enabled to exploration of proximity-induced spin effects (236, 237) and enhancement of graphene's plasmonic performance (238).

However, the lack of control over the integration of such particles into functional devices has long limited their application. Having established the optimum DEP parameters for trapping gold NPs in the previous chapter, this chapter will describe how we can form functional graphene-gold NP-graphene electronic devices and analyse the resulting transport properties.

4.1.1 Gold nanoparticle devices

Gold NPs, clusters of atoms with a diameter on the order of 100 nm, have been the subject of great interest since they were first studied by Faraday in the middle of the 19th century (239). Their chemistry allows them to be easily functionalised with organic molecules and their size leads to quantum confinement of their electrons, creating quantum dots (QDs) with tunable, size-dependent optical and electrical properties. This tunability has made them suitable for applications in sensing, therapeutics, computation and in optical devices (240–244). They have also proven to be a useful test-bed system for studying a range of transport phenomena (245) and have been at the centre of efforts to create useful single-electron transistors through techniques such as chemical assembly (178, 246–248), electrodeposition (249) and DC (169, 178, 179) and AC (170, 171, 173, 175, 250–253) dielectrophoresis. Gold NPs have also found applications in single molecule electronics, where the NPs have been dimerised using molecular linkers, the transport properties of which can then be probed by attaching the larger NPs to electrodes (182, 250, 253–255). Here, I will focus on the electrical properties of nanoscale devices formed from single NPs bridging across graphene nanogap electrodes.

4.1.2 Transport physics

A QD, like a molecule, possesses an integer number of electrons N which exist in discrete levels with spacing ΔE, and therefore has a total charge of Ne which remains fixed while the QD is isolated. If the QD is placed into an electrical circuit and is coupled to the electrodes by coupling energy $h\Gamma$, then adding an electron to the QD will alter its *electrochemical* potential by an addition energy $E_A = \mu_{dot}(N+1) - \mu_{dot}(N) = e^2/C + \Delta E$, composed of a change in its *chemical* potential ΔE, the level spacing, and an electrostatic charging energy $E_C = e^2/2C$ which depends on the capacitance C between the QD and it's environment (see Figure 4.1). The charging energy E_C only exists between $\mu_{dot}(N)$ and $\mu_{dot}(N+1)$ while all other levels are separated by ΔE, which is relatively constant in QDs, unlike molecules. If the coupling energy $h\Gamma$ between the QD and the electrodes is weak then, in accordance with Heisenberg's uncertainty principle $\delta E \delta t > h$ the timescale of electron transfer is slow and number of electrons on the QD at any one time will be well defined. The small size of QDs results in small values of C and thereby large values of E_C. When the temperature is lowered such that $k_B T \ll E_C$ then the occupation number N becomes fixed as electrons in the electrodes lack sufficient thermal energy to overcome the charging energy $\mu_{dot}(N) < \mu_{\mathrm{L}}, \mu_{\mathrm{R}} < \mu_{dot}(N+1)$ and the QD is in a state of Coulomb blockade.

Several authors have observed the energy level spacing ΔE within ultra-small metal NPs by means of tunnelling spectroscopy (256–259), finding that, unlike in molecules, ΔE is regular and remains independent of the number of electrons on the NP. Notwithstanding this discreteness, for metallic NPs larger than a few nanometers in diameter $\Delta E \ll E_C$ (245, 256, 258) and the chemical potential can therefore be regarded as a continuum (260), and the transport can be described in a semi-classical, purely electrostatic framework (261, 262). This framework is known as the *orthodox* theory and is valid while $h\Gamma, \Delta E \ll k_B T \ll E_C$. This theory

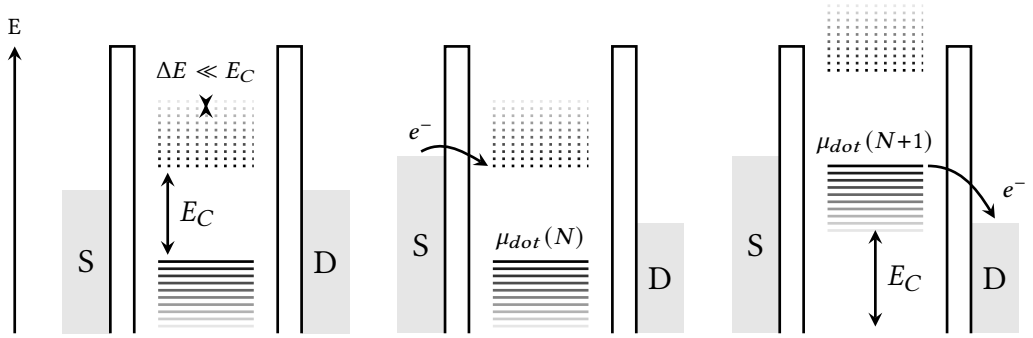


Figure 4.1: (left) An energy level diagram showing the relative level-spacing in a metallic quantum dot between two electron reservoirs. The charging energy E_C is much greater than the level spacing ΔE. (centre) Under a bias the Fermi level of the left reservoir is brought in line with an unoccupied state in the QD, allowing a single electron to hop onto the QD. (right) This changes the chemical potential of the dot by E_C, which raises it above the Fermi level of the right electrode allowing an electron to tunnel off the QD, restoring the chemical potential of the QD to $\mu_{dot}(N)$, and establishing a single-electron tunnelling current.

can be extended to consider the presence of quantised energy levels ΔE, provided that the level broadening $h\Gamma \ll k_B T$ and N remains well defined (263–266), but this is not the case in the large NPs used here and so will not be further considered.

4.1.2.1 Two terminal devices

Coulomb blockade may be lifted under the application of a potential difference V_{sd} between the source S and drain D electrodes such that $V_{sd} = (\mu_\mathrm{D} - \mu_\mathrm{S})/e$, raising the chemical potential in the source electrode and lowering that in the drain. With sufficient bias, $V_{sd} \sim E_C$, the lowest lying unoccupied level $\mu_{dot}(N+1)$ of the QD enters the bias window enabling an electron from the source electrode to tunnel onto the QD, which raises the electrochemical potential of the QD by the addition energy $E_A \simeq E_C$. $\mu_{dot}(N+1)$ is now the highest occupied level of the QD, above the chemical potential of the drain, and the electron may tunnel into an unoccupied state in the drain electrode, restoring the QD's potential to $\mu_{dot}(N)$ and generating a current between the source and drain electrodes. The large addition energy limits the current to a successive, correlated charging and discharging of the QD by single electrons, and as such generates a *single-electron tunnelling* current (265, 267).

We can obtain a simple expression for the current by recasting the picture in Figure 4.1 as an equivalent circuit diagram as shown in Figure 4.2 (262, 268, 269). Here, we treat each tunnel barrier as an resistor-capacitor (RC) unit, through which we can describe the Coulomb interactions between the charge on the QD $Q = (Ne - Q_0)$ and the electrons in the leads. The term $|Q_0| \leq e/2$ is used to account for any *fractional* charge on the QD due to the influence of external fields. We can apply a bias across the QD by connecting a voltage V_{sd} to the right electrode and connecting the left electrode to ground. Depending on the bias, electrons may be added to the QD from both the source and drain electrodes changing the systems energy by ΔE^+_S and ΔE^+_D, respectively (unrelated to the level spacing ΔE described above, which we have neglected). Conversely,

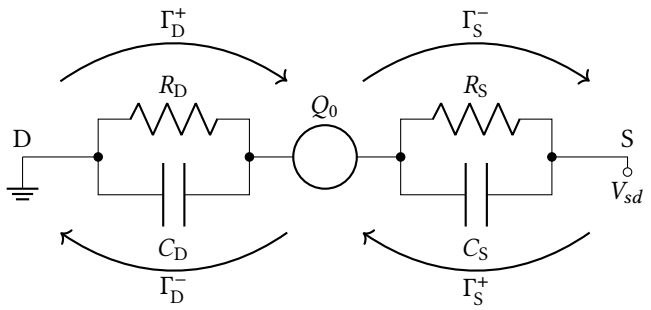


Figure 4.2: A circuit diagram representing the orthodox model. Each tunnel barrier is represented by a RC circuit and electrons tunnel from (−) (to (+)) the island to (from) the left (L) or right (R) electrodes, respectively, at rates $\Gamma^{\pm}_{L,R}$. The central island has a residual fractional charge Q_0.

electrons may be removed from the QD to the source and drain electrodes, changing the energy of the system by ΔE^-_S and ΔE^-_D, respectively. We can express these energies in relation to the initial state of N electrons on the QD as:

$$\Delta E^{\pm}_D(N) = U(N \pm 1) - U(N) \pm \frac{C_S}{C} eV_{sd} \tag{4.1}$$

$$\Delta E^{\pm}_S(N) = U(N \pm 1) - U(N) \mp \frac{C_D}{C} eV_{sd} \tag{4.2}$$

Where $U(N)$ is the *total* energy of the QD with N electrons, $C = C_D + C_S$ the total capacitance and the final term accounts for the fraction of the bias dropped over each RC tunnel barrier. Within the limits of the model we can define $U(N) = e^2N^2/2C$ and, as such, $\Delta U^{\pm}(N)$ as:

$$\Delta U^{\pm}(N) = U(N \pm 1) - U(N) = \frac{(Q \pm e)^2}{2C} - \frac{Q^2}{2C} \tag{4.3}$$

Substituting Eq. (4.3) into (4.1) and (4.2) we can write:

$$\Delta E^{\pm}_D(n) = \frac{e}{C}\left(\frac{e}{2} \pm (Q + C_S V_{sd})\right) \tag{4.4}$$

$$\Delta E^{\pm}_S(n) = \frac{e}{C}\left(\frac{e}{2} \pm (Q - C_D V_{sd})\right) \tag{4.5}$$

From these energy expressions we can determine the tunnelling rates $\Gamma^{\pm}_i$ to and from each electrode i by invoking the golden-rule expression:

$$\Gamma^{\pm}_i(N) = \frac{1}{R_i e^2}\left(\frac{-\Delta E^{\pm}_i(N)}{1 - e^{\Delta E^{\pm}_i(N)/k_B T}}\right) \tag{4.6}$$

Where any dependence of $\Gamma^{\pm}_i$ itself on N has been neglected. The current through the QD at a given bias voltage is then given by:

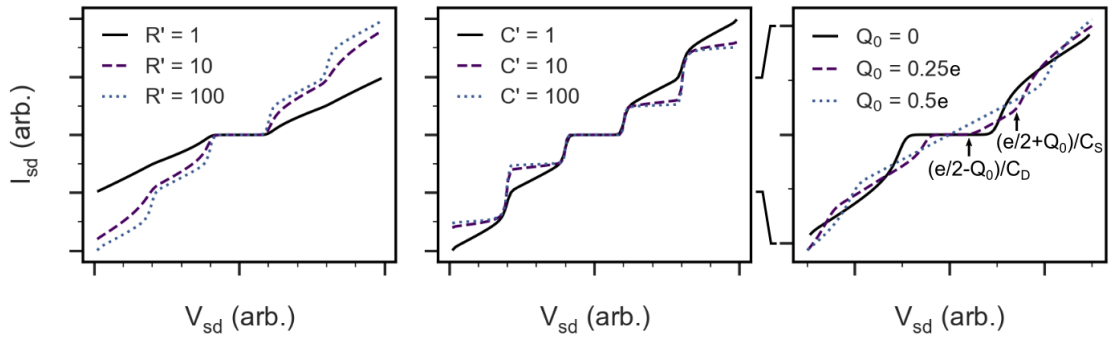


Figure 4.3: Current voltage curves as calculated by the orthodox model with various parameter relationships using arbitrary units. (a) $R' = R_S/R_D$, where $C_S = C_D$ and Q_0 is set to zero. (b) $C' = C_S/C_D$, with $R' = 10$ and $Q_0 = 0$. (c) $R' = 10$ and $C' = 1$. The two inflection points in the $Q_0 = 0.25e$ curve occur at the positions determined by the two labelled expressions. For $Q_0 = -0.25e$ this curve would be mirrored about $y = -x$, while the $Q_0 = -0.5e$ curve would be identical to $Q_0 = 0.5e$ unchanged.

$$I(V_{sd}) = e \sum_{N=-\infty}^{\infty} \sigma(N) \left[\Gamma_S^+(N) - \Gamma_S^-(N)\right] \equiv e \sum_{N=-\infty}^{\infty} \sigma(N) \left[\Gamma_D^-(N) - \Gamma_D^+(N)\right] \tag{4.7}$$

In order to find $I(V_{sd})$ we must first find $\sigma(N)$, which describes the ensemble distribution of the number of electrons on the QD: the probability that the occupation number of the QD is exactly N. We can find $\sigma(N)$ by noting that under a steady state the net probability of making a transition between any two neighbouring states is zero, such that:

$$\sigma(N) \left[\Gamma_D^+(N) + \Gamma_S^+(N)\right] = \sigma(N+1) \left[\Gamma_D^-(N+1) + \Gamma_S^-(N+1)\right] \tag{4.8}$$

Together with the normalisation condition $\sum_{N=-\infty}^{\infty} \sigma(N) = 1$ and the fact that $\sigma(N) \to 0$ as $N \to \pm\infty$ we can solve numerically for $\sigma(N)$ and thereby obtain $I(V_{sd})$. The algorithm used to calculate $I(V_{sd})$ is given in Appendix III. Figure 4.3 shows (4.7) as calculated using various relations between the parameters R_S, R_D, C_S, C_D and Q_0, as detailed in the caption. When there is an asymmetry between R_S and R_D the voltage drops mainly across the barrier with the larger resistance and broad step-like features become pronounced in the IV curves. This structure is known as a Coulomb staircase and is characteristic for this mechanism of charge transport. From Figure 4.3, we see that the staircase is most prominent when $R_S \gg R_D$, $C_S > C_D$ and $Q_0 = 0$.

4.1.2.2 Three terminal devices

As noted in the previous section, the charge on the QD can also be influenced by external fields. Unlike the discrete charging effect that results from changes in V_{sd}, $U(N)$ can also be varied continuously by an external electrostatic potential which acts to gate μ_{dot} and change its alignment with respect to μ_D and μ_S. We can add to our picture a third electrode coupled to the dot by a capacitance C_G to which we can apply a gate voltage

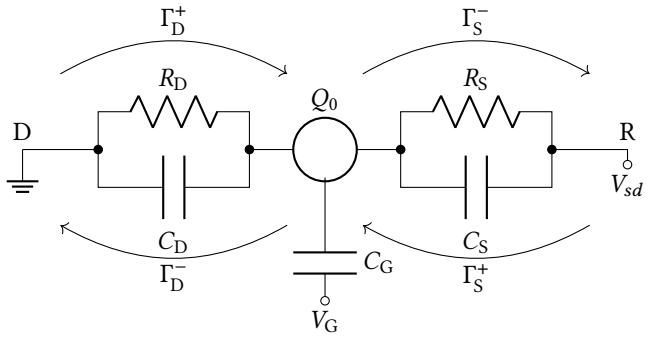


Figure 4.4: A circuit diagram representing the orthodox model for a three terminal device. Each tunnel barrier is represented by a RC circuit and electrons tunnel from (−) (to (+)) the island to (from) the source (S) or drain (D) electrodes, respectively, at rates $\Gamma^{\pm}_{S,D}$. The central island has a residual fractional charge Q_0 and is capacitively coupled to the gate voltage V_G by the capacitor C_G.

V_G. This modifies $U(N)$ to include a second contribution such that $U(N) = Q^2/2C - NeV_G$ and we include C_G in C such that $C = C_D + C_S + C_G$. Following the same procedure as before we find modified forms of (4.4) and (4.5) where:

$$\Delta E^{\pm}_D(N) = \frac{e}{C}\left(\frac{e}{2} \pm (Q + C_S V_{sd} - C_G V_G)\right) \tag{4.9}$$

$$\Delta E^{\pm}_S(N) = \frac{e}{C}\left(\frac{e}{2} \pm (Q - (C_D + C_G)V_{sd} - C_G V_G)\right) \tag{4.10}$$

From here the derivation of the expression for the current follows the same process as above, using (4.6) to calculate the tunnelling rates and (4.7) to find $I(V_{sd}, V_G)$. The current can then be plotted as a function of V_{sd} and V_G in the form of a stability diagram like that shown in Figure 4.5. When measured experimentally, these diagrams allow for the capacitances to be determined directly from the spacing and gradients of the Coulomb diamond edges according to the relations shown in the Figure.

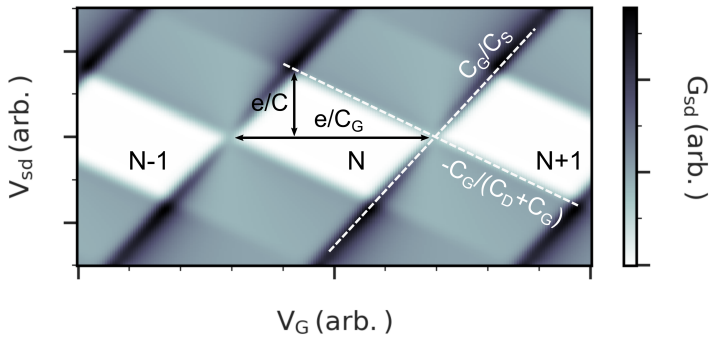


Figure 4.5: A sample stability diagram as calculated from the orthodox model. Each white diamond corresponds to the Coulomb blockaded region for the labelled charge states. The gradients of the diamond edges, together with their total width and height gives information which allows the values of C_S, C_D and C_G to be found.

4.2 Device preparation

Having established the optimum DEP parameters for our devices in the previous chapter, I went on to explore whether they could be used to study electrical transport physics across the captured particles. Before measuring devices decorated with NPs, I first explored whether the nanogaps themselves would retain their Simmons-like tunnelling behaviour when exposed to the potentials required for trapping. I found that under air, water and in a 2 mM sodium citrate solution the IV curves of the nanogaps before and after applying the trapping potential did not change significantly up to a voltage of $0.75\,V_p$. At larger potentials, devices were increasingly likely to 'break', showing no tunnelling current at biases below 1V. This loss of conductivity is attributed to the following: under air, we would expect that the application of large ($>$ 1 V) voltages may further expand the nanogap given that the electroburning procedure relies on successive voltage ramps to voltages of this magnitude (73, 270), while under aqueous environments it has been observed that graphene undergoes electrochemical degradation at moderate potentials which likely contributes to the loss of conduction under these conditions (271, 272). We do not expect Joule heating to play a role in the loss of tunnelling as it should have negligible impact in low-conductivity solutions such as the one used here even under large biases (191). Fortunately, this limit coincides with the optimum trapping parameters for single-particle capture and suggests that devices formed using the procedure outline in Chapter 3 should remain viable after NP capture.

4.2.1 Fabrication

For this study I chose devices which had a local gate electrode buried under a thin dielectric layer which would afford strong coupling between the gate and the trapped NP and provide rich spectroscopic information. The devices were fabricated at wafer scale by fellow group members. Briefly, first an array of local gate electrodes (40 nm high) were patterned onto a degenerately doped Si substrate with a 500nm thick SiO_2 oxide layer using photolithography. Second, a 10 nm layer of HfO_2 was deposited by atomic layer deposition (ALD) to isolate the gate electrode. Then pairs of source and drain electrodes were defined in a second photo-lithography step on top of the ALD layer, followed by the deposition 5 nm of chromium and 55 nm of gold. Wafers of devices were then sent to the company Graphenea who transferred 6 inch pieces of graphene, grown by chemical vapour deposition, over the top of the patterned electrodes. After receiving the wafers back from Graphenea, I spin-coated them with a protective layer of photoresist before dicing the wafers into 1×1 cm chips, with a large array of over 800 devices on each chip. The protective photoresist layer could then be removed by immersing the chips in warm acetone for several hours after which the graphene could be patterned into bow-tie shaped constrictions by electron-beam lithography following the same method outlined in Chapter 1. After patterning was completed chips were diced further by hand into 16 pieces with roughly 50 devices on each piece. This allowed the number of experimental runs to be maximised for each patterned chip and

minimised wastage of devices.

4.2.2 Deposition

In order to create single electron transistors I performed the following steps:

- First, a chip piece would be mounted onto the chuck of an automated probe station.
- The graphene constrictions on the chip would be electroburned to form nanogap electrodes following the method outlined in Chapter 1 to achieve tunnel junctions with a target resistance of 1 GΩ.
- After electroburning, the devices were characterised by taking IV curves over a ±1V range and all viable tunnel junctions were selected for DEP trapping.
- The probes would then be connected to a function generator set to the optimum trapping parameters of 0.75 V_p at 1 MHz as ascertained in the previous chapter.
- A 2 μl droplet of gold nanoparticle citrate solution was deposited onto the surface of the chip piece, covering the surface and remaining in place thanks to surface tension.
- The probes were set to automatically engage each device for a period of 30 s before moving on to the next device. The nanoparticle solution remained on top of the chip and the probes would move through it to progress to the next device.
- After all devices had been contacted the probes were removed and the function generator was disconnected. The chip piece was then removed from the probe station and washed with a gentle flow of de-ionised water to remove the remaining nanoparticle solution.
- The chip piece would then be dried under a flow of nitrogen gas.
- The chip pieces could then be re-characterised on the probe station and wire-bonded into a 44 pin chip carrier for cryogenic transport measurements.

4.2.3 Characterisation

With the knowledge that the trapping parameters should produce several suitable devices per chip piece, and in an effort to preserve the transport properties of the nanogap and nanoparticle, devices were not SEM imaged after trapping but were instead only characterised electronically. However, I quickly discovered that the success of the trapping could not be immediately judged by electrical characterisation. I had expected to see an increase conductance due to the NPs establishing a new conductive channel, however, I found that the conductance of the devices either remained unchanged or was significantly reduced to below the noise floor of the current amplifier at sub-volt biases. This change did not correlate with the success of trapping or with

the number of NPs trapped, as confirmed by subsequent SEM imaging. Indeed, SEM imaging later revealed that the majority of devices had successfully captured nanoparticles, and exposure to the electron beam established conductive channels in many devices, likely due to contamination or modification of the chemical environment by the electron beam. Contamination on the graphene electrodes, perhaps compounded by the DEP process, in addition to the citrate functionalisation of the NPs, likely make a significant contribution to the poor contact between the nanoparticle and the electrodes. The reduction of tunnelling currents for some nanogaps may also have been caused by trapped NPs 'shorting' the devices and damaging the graphene nanogaps. Additionally, the presence of the highly negatively charged NPs would be expected to significantly alter the energy landscape around the nanogap and therefore the tunnel barrier, which might explain the total loss of conduction from the underlying nanogap.

4.2.4 Annealing

In order to establish good contact between the NPs and the graphene an annealing step was introduced. The annealing step was designed to help remove contaminants from the surface of the graphene (273) and also increase the mobility of the gold atoms on the NPs surface (274), which would aid the establishment of electrical contact. Annealing was performed in a tube furnace under a protective argon atmosphere. Initial trials at 300 °C resulted in highly conductive devices, with currents that increased from nano-Amps before DEP to micro-Amps after DEP and annealing. However, SEM imaging revealed that at 300 °C the NPs would melt and relax into spheres (Figure 4.6b). At 200 °C degrees a large proportion of devices were also revived, albeit to lower conductivities than at 300 °C, but the NPs retained their aspect ratio indicating they had not fully melted (Figure 4.6a).

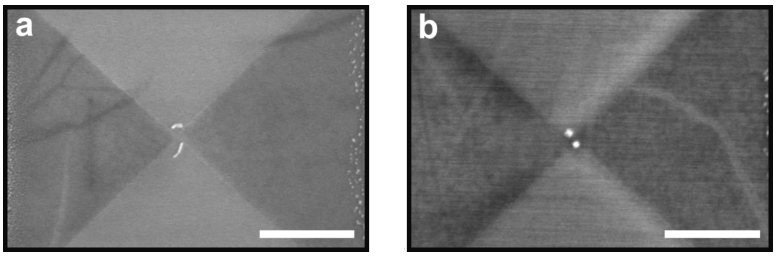


Figure 4.6: SEM images of devices annealed at (a) 200 °C and (b) 300 °C. The scale bars represent 1 μm.

The IV behaviours before and after annealing for three representative devices are shown in Figure 4.7. As a control, bare graphene nanogaps that were annealed under the same conditions were found to lose all tunnelling behaviour. This indicates that the nanogaps themselves relax somewhat at these temperatures and confirms that the conductivity seen in devices bridged by NPs after annealing is indeed established via the NPs. The above annealing step was then introduced for all subsequent chip pieces before further measurement.

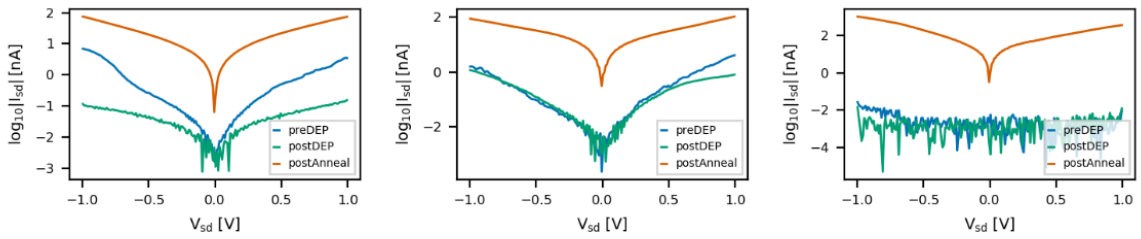


Figure 4.7: Logarithmic IV traces for three devices before dielectrophoresis, after dielectrophoresis and after annealing at 200 °C.

4.2.5 Measurement

After the annealing step had been established devices were ready to be characterised at low temperatures to understand the nature of the charge transport. The chip pieces were mounted onto 44 pin chip carriers and devices that showed an increase in conductivity following annealing were wire-bonded to the carrier. The carrier was mounted into a puck and loaded into an Oxford Instruments Puck Tester dry cryostat which was evacuated to 10^{-4} mbar and cooled to 3 K. IV traces and stability diagrams were then measured for all viable devices. Multiple chip pieces were measured in order to capture a representative array of data.

4.3 Results

At 3 K I saw clear Coulomb blockade features in the IV curves and gate-traces (IV_g) for multiple devices. A selection of IV curves are shown in Figure 4.8.

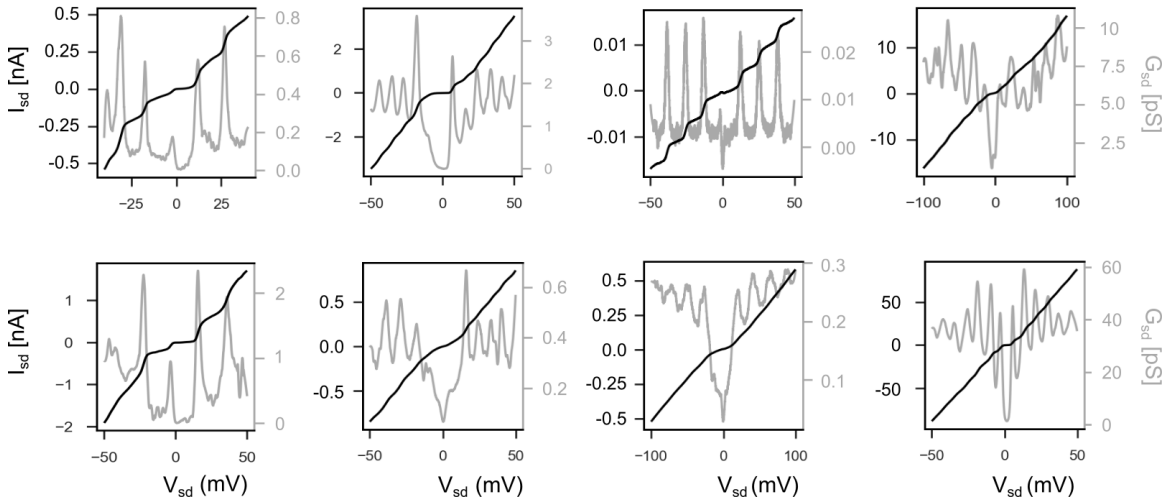


Figure 4.8: IV traces and their numerical derivatives measured for a selection of gold nanoparticle devices.

Clearly, these IV curves show characteristic Coulomb staircase behaviour, particularly evident by the equally spaced peaks in the numerical derivative. However, it is also apparent that the parameters are not uniform across devices leading to variations in total conductivity and periodicity of the Coulomb peaks. We can find these parameters by fitting our data to Eq. (4.7), but first we must obtain an estimate for the

Device	C'_S	C'_D	C'_G
A	13.5	6.0	4.2
B	11.7	1.1	6.2
C	8.3	7.7	2.3

Table 4.1: Graphically extracted capacitance values, given in units of atto-Farads (aF).

capacitance between the NP and the gate electrode without which we cannot independently determine C_S and C_D. For this we need to measure $I(V_{sd}, V_G)$ and build a stability diagram of the current. Figure 4.9 shows stability diagrams measured for three devices. Unfortunately, it was not possible to obtain stability diagrams for all devices due to large gate-leakage currents which destroyed several devices. These currents arise either due to tunnelling through the thin gate oxide, facilitated by defects in the oxide or fabrication errors, or leakage between measurement channels in the copper loom which carried the currents within the cryostat.

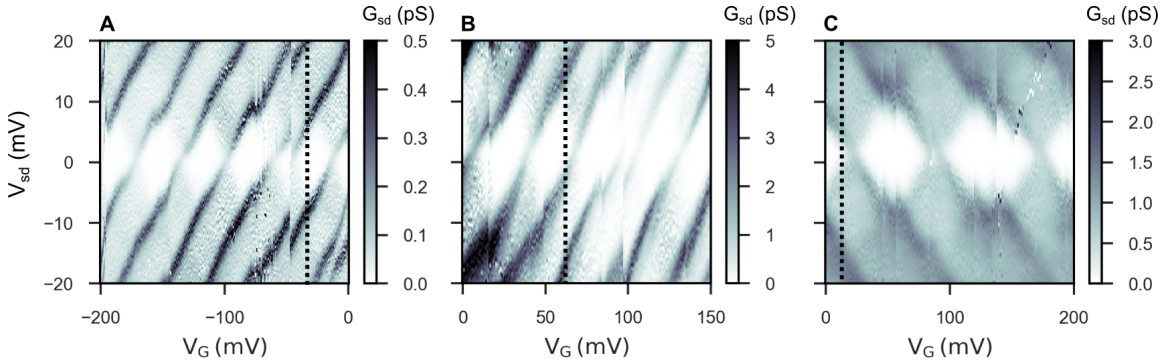


Figure 4.9: Measured differential conductance stability diagrams for devices A, B and C. The dashed lines correspond to the position of the IV curves that are shown in Figure 4.10.

The regular width the Coulomb diamonds seen in Figure 4.9 implies that the charging energy E_C of the NP is dominant over the level spacing ΔE, and no excited states are observed parallel to the diamond edges. The fact that only two gradients are observed in each stability diagram and that the diamonds 'close' at zero bias indicates that transport is occurring through a single NP (275). A 'particle-in-a-box' estimate $\Delta E = 2\pi^2\hbar^2/m_e k_F V$ (212, 245) gives $\Delta E \approx 17\,\mu$eV for a spherical gold nanoparticle of equivalent volume V. Such small excitations would only become resolvable at temperatures below 200 mK (265), and indeed are not resolved at 3 K. This strongly suggests we are in the classical orthodox regime ($E_a \approx E_C \gg \Delta E$) as was expected for metallic NPs of this size (276, 277).

The stability diagrams in Figure 4.9 all exhibit multiple discontinuities as the gate-voltage is swept. These discontinuities are caused by sudden rearrangements of local background charges which themselves electrostatically gate the nanoparticle, shifting the position of the Coulomb diamonds. These background charge traps can be quite disruptive to transport measurements but are intrinsic to each device and are commonplace in all single-electron tunnelling measurements. By measuring the spacing of the diamonds and the gradients of their edges we can obtain estimates for the capacitances C'_S, C'_D and C'_G using the relations shown in Figure 4.5. The extracted values are given in Table 4.1.

Device	C_S (aF)	C_D (aF)	C_G (aF)	R_S (MΩ)	R_D (MΩ)	Q_0 (e)	E_C (meV)	β (eV V^{-1}))
A	11	6.5	4.2	58	1.2	-0.28	7.4	0.19
B	10	1.1	6.0	6.2	0.55	0	9.4	0.35
C	9.3	6.4	2.4	1.1	5.8	0.17	8.9	0.13

Table 4.2: Parameters resulting from fits to the orthodox model. $\beta = C_G/C$ is the lever-arm.

Taking the values of the gate capacitance extracted from the stability diagrams $C_G = C'_G$ and using the values of C'_S and C'_D as starting parameters I fitted Eq. (4.7) to IV traces at selected gate voltages (indicated by the dashed lines in Figure 4.9). The results of the fitting as well as subsequently calculated stability diagrams are shown in Figure 4.10 and the corresponding parameters are listed in Table 4.2. The calculated stability diagrams reproduce the measured stability diagrams well. The capacitances take similar values across all three devices, resulting in a fairly uniform value for the charging energy E_C with a mean value of 8.6 meV. We can compare this value with an estimate for the self-capacitance of a rod-like prolate ellipsoid $C_{self} = 4\pi\epsilon_r\epsilon_0 2aM/\log((1+M)/(1-M))$ where $M = \sqrt{1 - c^2/a^2}$ (278). We account for the mixed dielectric environment by taking $\epsilon_r = (1 + \epsilon_{HfO_2})/2 \approx 7$. This yields $C_\Sigma = 11$ aF for an ellipsoid with dimensions $a = b = 7.5$ nm and $c = 30$ nm, the average dimensions of one of the gold NPs used in this study. This estimate only provides a lower bound for the capacitance as we have not considered any other capacitances within the system such as those between the three electrodes. We therefore obtain an upper bound for the charging energy of $E_C^* = e^2/C_{self} \approx 14.6$ meV (126), which is in good agreement with the extracted values.

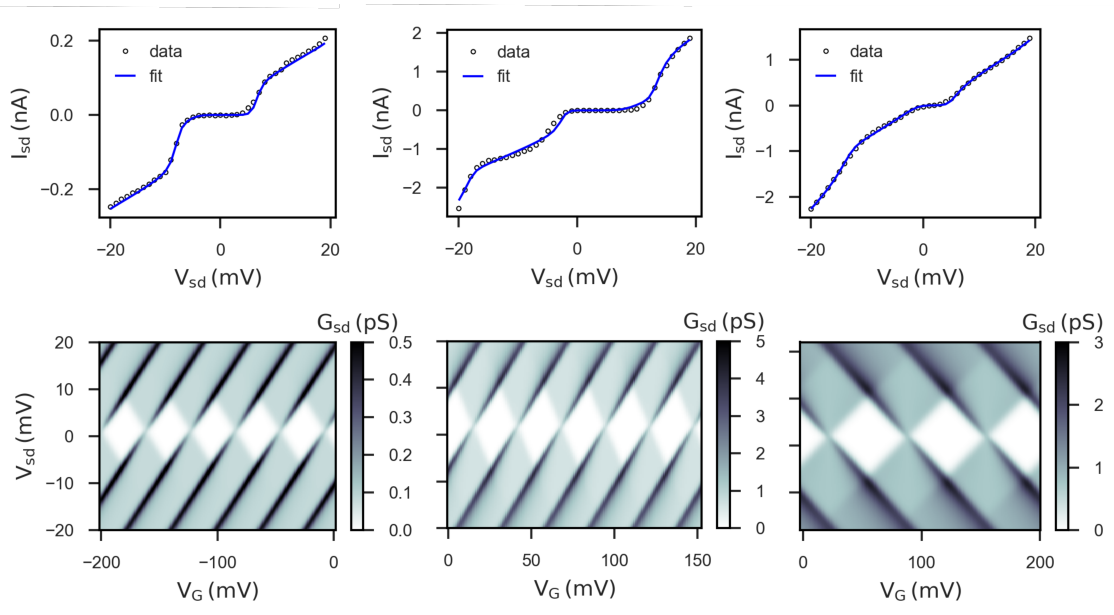


Figure 4.10: IV curves fitted to the orthodox model (top) and the stability diagrams calculated from this fit (bottom) for devices A, B and C.

The resistances however show much more variation. Asymmetries in values may be indicative of the NPs being off-centre with respect to the nanogap, which is quite likely given that the NPs are considerably longer than the widths of the nanogaps. The capacitance and resistance values are highly dependent on the exact

positioning of the NP and will be affected by the local shape of and disorder around the electrodes. Notably, however, for devices A and B we find that $C_S > C_D$ and $R_S > R_D$. This is an unusual situation as, in a purely electrostatic framework $C \propto 1/d$, with d the separation between the NP and an electrode, while $R \propto d$ (279). We would then expect if, say, the NP was positioned more over the source electrode that $C_S > C_D$ but that $R_S < R_D$. The exact reason for this peculiarity is unknown, but it is know that graphene and gold couple weakly (280), due in part to the low density of states of graphene, resulting in a large sensitivity of the contact resistance to chemical termination, contact area, contaminants and defects (281, 282) which would upset the purely electrostatic picture and result in weakly coupled tunnel barriers. The relatively large values for C_G are a result of the close proximity of the gate electrode, the choice of a high-κ dielectric and the reduced screening of the gate voltage by the graphene electrodes compared to equivalent metallic electrodes (74). For the remaining devices where stability diagrams are not available it is much more challenging to fit the IV traces to the orthodox model as without the estimates from the stability diagrams there are six independent parameters which must be fitted.

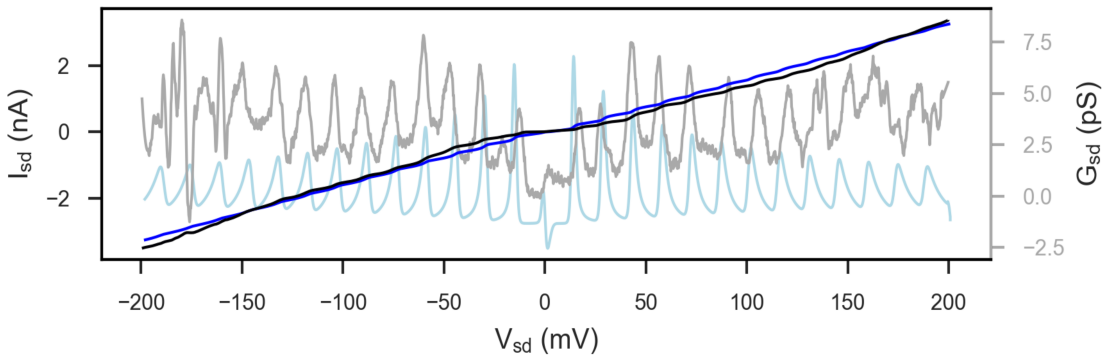


Figure 4.11: An IV trace and associated the numerical derivative conductance-voltage trace taken from device A are shown in black and grey, respectively. A best-fit orthodox IV trace is shown in blue, while its numerical derivative is shown in light blue.

While the orthodox model describes the transport properties of these devices well over small bias ranges, at larger scales it becomes harder to achieve satisfactory fits as the assumptions within the orthodox model become less valid. Specifically in this case, the assumptions that the density of states within the electrodes and NP, and thereby the tunneling rates between them, are independent of energy, valid for metal electrodes, do not hold for graphene which has a discontinuous density of states. The consequences of this can be seen over large bias and gate voltage ranges such as those shown in Figures 4.11 and 4.12. We see that the orthodox model cannot reproduce the non-linearity of the IV curve over a larger voltage range and that the spacing and heights of the conductance peaks show small fluctuations resulting in mismatches with the orthodox model.

In Figure 4.12 we see that there are numerous discontinuities in the charge environment which make detailed analysis of the transport challenging. Many of these discontinuities occur when the bias changes direction during IV cycles. Other notable features are the fluctuations in the conductance which occur over a

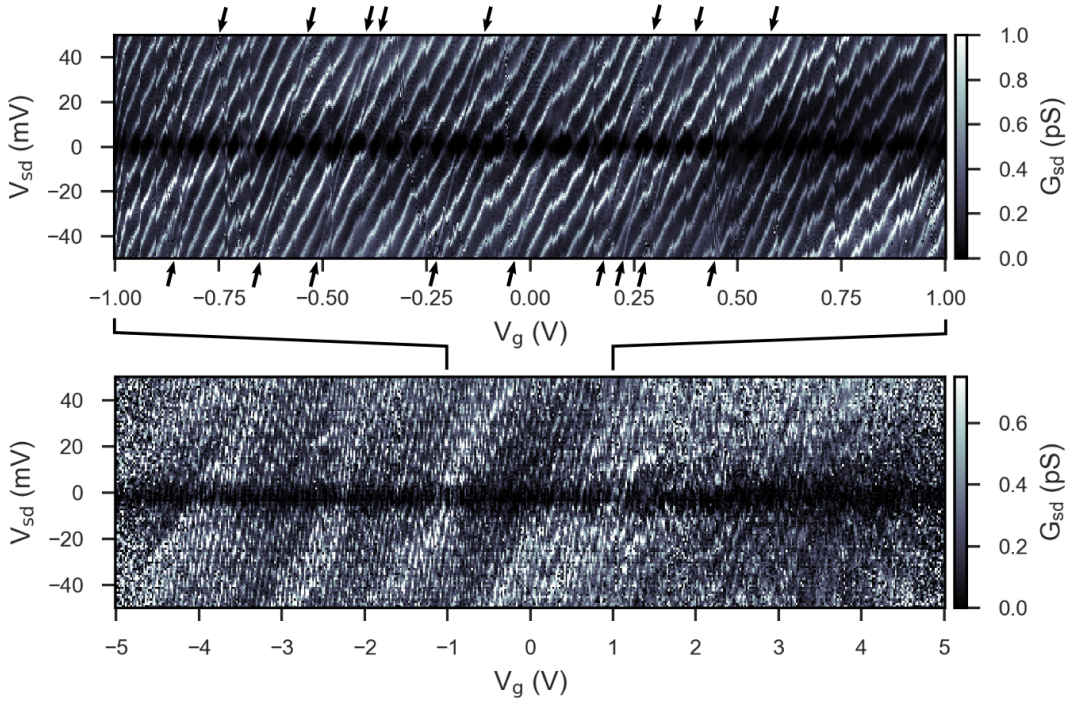


Figure 4.12: (top) A differential conductance stability diagram for device A between ±1 V. The arrows indicate the position of additional excitations which cut through the regular orthodox Coulomb blockade. We also observe modulations in the conductance with the gate voltage and the abundance of charge discontinuities which interrupt the regular blockade. (bottom) A differential conductance stability diagram taken between ±5 V for device A which exhibits further modulations in the conductance as a function of gate voltage. In this plot we resolve additional large Coulomb diamonds which likely arise from local states in the graphene electrodes or other nearby, weakly coupled NPs.

large gate voltage range and the appearance of additional lines in the stability diagram which do not run parallel to the diamond edges, creating level crossings as they pass through the diamond edges. These are likely caused by other local charge islands which couple to the transport through the NP. A likely culprit for these charge states is local disorder within the graphene or edge states near the nanogap (94, 144). Furthermore, it is likely that several devices have multiple NPs around the nanogap region and, while one NP may dominate the conduction, neighbouring NPs can strongly influence the transport adding additional Coulomb diamond features (275).

These features suggest that we are not purely in the classical orthodox regime as we first expected. According to (264) the lineshape of a Coulomb blockade resonance as a function of gate voltage is given by:

$$G/G_{max} \approx \cosh^{-2}\left(\frac{\beta e|V_g - V_0|}{Ak_BT}\right) \tag{4.11}$$

where $\beta = dE/dV_g = C_G/C$ is the lever-arm, V_G is the gate voltage and V_0 is the voltage at which the resonance is centred. The factor A is equal to 2.5 in the classical limit $\Delta E \ll k_BT \ll e^2/CE$ and 2 in the quantum regime $h\Gamma \ll k_BT \ll \Delta E$, equivalent to that given in Eq. (1.14). Figure 4.13b shows three adjacent Coulomb resonances fitted to (4.11). By fixing the temperature to the experimental temperature (2.9 K) and

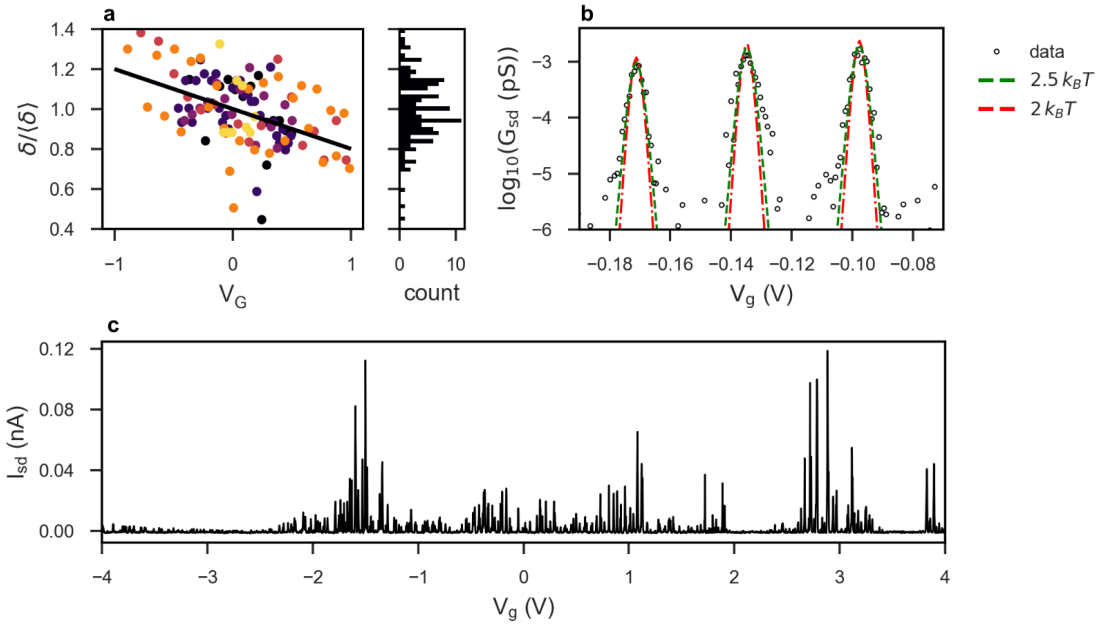


Figure 4.13: (a) Normalised peak spacing as a function of gate voltage, with an associated histogram. Each colour represents a different device. (b) A differential conductance gate trace taken from device A. Each peak is fitted to Eq. 4.11 in the classical limit with $A = 2.5k_BT$ (green) or in the quantum limit where $A = 2k_BT$ (red). (c) A gate trace taken over a large gate voltage range to show the variation in peak heights.

taking values of β as determined from the capacitances in Table 4.2 we observe a small difference between the fitted line shapes, with the classical resonance having a broader line shape that gives a slightly better fit to the data, though the distinction is small. We can further obtain an estimate for the tunnel rates $\Gamma_{L,R}$ and therefore the resonance widths $h(\Gamma_L + \Gamma_R)$ according to the relation:

$$G_{\max} = e^2 B \frac{\Gamma_L \Gamma_R}{\Gamma_L + \Gamma_R} \tag{4.12}$$

Where $B = \rho/2$ in the classical limit and $B = 1/4\hbar k_B T$ in the quantum regime. Here, ρ is the density of states within the NP: $\rho = 1/\Delta E$ (265, 277). As transport through such a system is limited by the smallest tunneling rate, we can find a lower limit on the tunneling rate by setting $\Gamma_L = \Gamma_R = \Gamma_{\text{lower}}$ such that $\Gamma_{\text{lower}} = 4G_{\max}\Delta E/e^2$. Taking the value of $\beta = 0.19$ for device A alongside an average value of $G_{\max} \simeq 0.06$ pS and our 'particle-in-a-box' estimate for ΔE, we find that $\Gamma_{\text{lower}} \approx 25.5$. This lower bound is so low that it is essentially meaningless and certainly meets the criteria of $h\Gamma \ll k_B T$. In the classical regime we would expect that the conductance peak would narrow with decreasing temperature but maintain the same height, unlike in the quantum regime where the peak height increases with decreasing temperature, however unfortunately temperature dependent data is not available for these devices. The height of classical zero-bias conductance peaks should also be independent of gate voltage at a given temperature, whereas in the quantum regime the peak height is very sensitive to the coupling between the NP and the electrodes which can vary randomly with each energy level (267). From Figure 4.13c we see that the current can vary wildly with gate voltage,

contrary to expectations. It is difficult to know whether the distribution of peak spacing is due to the influence of additional NP energy levels, a consequence of the prevalence of charge discontinuities seen in Figure 4.12, the effect of additional NPs (275, 283) or are due to density of states fluctuations in the graphene electrodes. More statistics would be needed to discern the underlying mechanism (267), and temperature dependent measurements would also shed light on the nature of the observed peaks. We do, however, observe a negative trend in the peak spacing across several devices (see Figure 4.13 a) with increasing gate voltage, indicating a gradual increase in the total capacitance as more electrons are added to the NP.

4.4 Discussion

Given that gold NPs are well known to behave in accordance with the classical orthodox model and $\Delta E \ll E_C$ at diameters greater than $\sim$ 10 nm (245, 256, 258), I believe that the deviations from the classical model that I observe most likely arise from density of states fluctuations within the graphene electrodes. My measured values for E_C are in good agreement with other values reported in studies which examined gold NPs of comparable sizes (256, 257, 284). I am confident that the observed transport behaviour is chiefly attributable to the gold NPs as all devices that exhibited conductance increases after the annealing step were found to have NPs situated over the nanogap when imaged. However, it is pertinent to consider whether the observed behaviour could instead be entirely due to local state within the graphene electrodes (123, 127–129) or to a graphene QD created during the electroburning process (92, 94, 122, 131, 285). A graphene QD with an equivalent addition energy to that which I observed would need to have a diameter on the order of 100–150 nm (126), which is approximately the width of the constriction before electroburning. Studies on lithographically defined graphene QDs of this size have observed average level-spacings ΔE on the order of 2 meV (126), which would appear as additional lines parallel to the Coulomb diamond edges, which I did not observe. Such a QD would operate within the quantum regime with $k_B T \ll \Delta E \sim E_C$ and would exhibit strong, chaotic, fluctuations in the addition energy, which I also did not observe.

However, there are clearly deviations from the orthodox model in the presented data. We might expect that any metallic NP of similar size would exhibit purely classical behaviour (245), but it is also reasonable to expect that the disorder-induced local states observed in graphene QDs and constrictions are likely to be present in our electroburned nanogaps, as shown in Chapter 2. Furthermore, bulk graphene has a discontinuous density of states and is itself affected by electrostatic gating. Together, these effects manifest as density of states fluctuations within the electrodes and localised states which interfere with the transport through the NP causing level splitting and strong modulations in the tunnel coupling (94, 130, 286, 287). We also note that NP single-electron transistors formed using gold as an electrode material produce markedly 'cleaner' and more consistent stability diagrams despite often involving organic monolayers as tunnel barriers (248, 257–259, 284), indicating further that the observed deviations from the orthodox model are due to the graphene

electrodes.

4.4.1 Limitations

Despite achieving the goal of forming single-electron transistors by integrating NPs into graphene nanogaps using the technique of dielectrophoresis, the resulting devices have some limitations. Firstly, as discussed in Chapter 3, despite the small size of the trapping zone the trapping of NPs is not exact and the capture of single NPs cannot be guaranteed. Secondly, while the devices here discussed have similar capacitance parameters, these are not themselves controllable. The influence of localised states within the electrodes, while indicating the potential for hybrid devices, is device dependent, and largely a result of the quality of the graphene, the lithographic patterning and the electroburning process. Many of devices in this study suffered from gate leakage which was likely due to defects in the dielectric or lift-off edges created during the wafer-scale fabrication causing shorts which lead to the disintegration of the graphene electrodes. These faults meant that robust measurements over long time periods were not possible for most devices, resulting in a lack of statistics on device to device variance. The abundance of charge discontinuities seen in the stability diagrams and variable spacings seen in the IV curves may in part be caused by residues of the citrate functionalisation which were not removed during annealing. Alternatively, they may be caused by charge traps located within the dielectric or exist as graphene edge states.

4.5 Conclusion

Here, I have demonstrated the directed formation of single-nanoparticle single-electron transistor devices using the technique of dielectrophoresis. Our nanometre separated electrodes are ideally placed to form electrical contact across the even the smallest nanoparticles, and the inclusion of a local gate electrode allows for tunable transport measurements. These devices are well described by the orthodox theory of Coulomb blockade at low biases but exhibit significant deviations from this model over larger scales due to the non-ideal behaviour of the graphene electrodes. This work shows that graphene nanogaps offer an attractive platform for the study of the transport properties of hybrid devices where graphene is coupled to a whole host of engineered NPs with an array of electrical properties.

Further work is needed in order to improve the reproducibility of these devices, which may be realised by reducing contamination on the electrodes and the particles. This could be achieved by changing or removing the functionalisation of the NPs or through further post processing steps to remove residues. As for reducing disorder in the graphene electrodes, these devices face the same challenges outlined in Chapter 2. Future work to build on the promising results described in this chapter might involve the exploration of whether functionalisation of the NPs could be exploited to introduce desired functionality to the devices, perhaps using them as a platform for molecular electronics. One further experiment of particular interest would be to

investigate whether these devices emit light under moderate biases, as has been observed by several other authors for gold NPs (197, 198, 227, 228, 288), and to explore the potential advantages of our graphene-based devices for plasmonic applications (228, 238, 289, 290).

Outlook

In this chapter I have described how I formed single-electron transistors from gold nanoparticles trapped using dielectrophoresis. I explored the transport properties of these devices and found them to show the expected orthodox behaviour at low biases but with deviations at higher biases due to the influence of the graphene electrodes. This work has oppened the possibility of studying charge transport through a range of other nanomaterials at single-particle resolution. The next chapter will explore transport through one other such material, magnetite nanocrystals.

Chapter 5

Magnetite nanocrystals

Overview

In this chapter we will explore the properties of devices composed of magnetite nanocrystals, formed using the dielectrophoretic method. I will discuss the unsettled question of the nature of electrical transport in magnetite at low temperatures, with a particular focus on work examining nanoscale magnetite crystals. I will demonstrate the method used to create the magnetite devices and show a range of transport observations including gate voltage, magnetic field and temperature dependence while setting my results in the context of other published work.

5.1 Introduction

Magnetite, Fe_3O_4, is an important naturally occurring mineral which has been used by humans for over 2,000 years. Today, it is principally used as an iron-ore and as a catalyst in the Haber-Bosch process, but it also has a significant cultural history as *lodestone*, used for divination and later to make the first magnetic compasses (291). Magnetite is a transition-metal oxide: a family of strongly-correlated materials which can exhibit phenomena such as magnetic ordering, high temperature superconductivity, resistive switching, and phase transitions (292). Magnetite has historically been viewed as an archetypal strongly-correlated material, and as such has been intensively studied in an attempt to further our understanding of this whole family of materials, while remaining of particular interest in itself as a material for magneto-electronic devices (293). Here, I will outline the conventional 'Verwey' model of magnetite and briefly cover some of the more contemporary observations on its structure before moving on to focus on its electronic transport properties in detail.

5.1.1 Formal Structure

Magnetite exists in a inverse spinel cubic structure AB_2O_4 where the Fe ions formally exist in a $2:1$ ratio of $Fe_3{}^+$ and $Fe_2{}^+$ charge states and sit in a lattice of closely packed $O_2{}^-$ ions (see Figure 5.1a). $1/8$ of the tetrahedral A sites are occupied by half of the $Fe_3{}^+$ ions (A3) while $1/2$ of the octahedral B sites are occupied by an equal ratio of the $Fe_2{}^+$ ions (B2) and the remaining $Fe_3{}^+$ ions (B3). The crystal field environment results in all of the octahedral and tetrahedral Fe ions existing in high spin configurations, where the $Fe_3{}^+$ ions have 5 d electrons and the $Fe_2{}^+$ ions have 6. Below its Curie temperature of 850 K magnetite is a ferrimagnet, meaning that the spins of the tetrahedral sites are anti-aligned with those of the octahedral sites, and the majority spins of each ion are locked into place by a large exchange energy, leaving only the single 6 d electrons on the B2 sites, which occupy minority spin t_{2g} orbitals ($e_{t_{2g},\downarrow}$), to be involved in bonding.

5.1.2 The Verwey Model

Magnetite's most characteristic property is that it undergoes a first-order phase transition at a critical temperature $T \approx 120$ K which manifests as a drastic and sudden decrease in the electrical conductivity, magnetisation and lattice symmetry, alongside anomalies in the specific heat and many other properties (294). A physical model for the phase transition was first proposed in 1947 by Verwey *et al.* (295) which proved so convincing that the transition has since become known as the *Verwey* transition, and the temperature at which it occurs the *Verwey* temperature T_V. In Verwey's model, this transition is of a metal-insulator type. At temperatures greater than T_V, the $e_{t_{2g},\downarrow}$ electrons are able to delocalise throughout the B sub-lattice, which enables magnetite to act as a 'bad metal'. Below T_V, the minority spin electrons become localised into discrete $Fe_2{}^+$ and $Fe_3{}^+$ ions, as in the formal structure, which are arranged in some form of long-range order throughout the lattice. This *charge-ordering* is proposed to explain the observed sudden drop in conductivity as the electrons can no longer move freely through the lattice (296).

The question of the exact nature of the charge ordering above and below T_V, the competition between mechanisms of short-range and long-range order (SRO and LRO, respectively) and how these mechanisms may relate to the changes in lattice symmetry has been the topic of intense discussion ever since. A comprehensive review of the progression of research up until 2002 is given by Walz (294), who concluded that many of the ambiguities and inconsistencies that had plagued magnetite research until at least 1979 could be attributed to inconsistent crystal quality and preparation. However, characteristic of the disputes over the nature of charge-ordering Walz concluded that there was *clear* evidence for Verwey-like charge ordering below T_V, while 2 years later García and Subías concluded in a review (297), which they later backed up with with new experimental data (298), that there was *no* experimental proof for any charge-ordering in magnetite, refuting the Verwey model entirely.

5.1.3 Crystal Structure

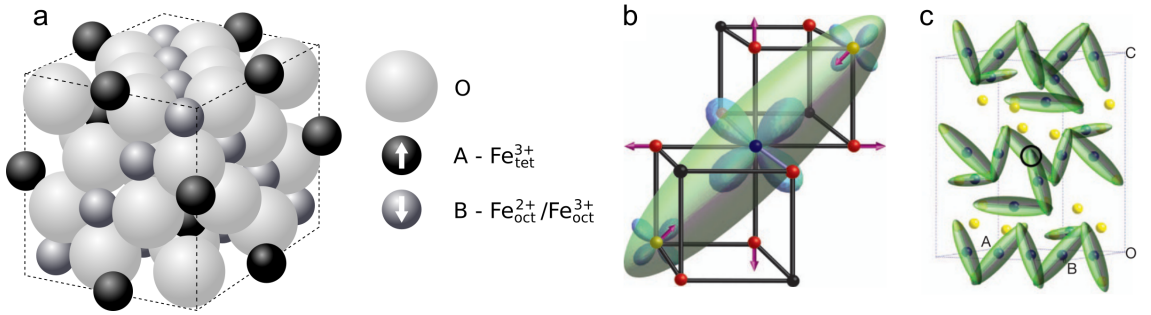


Figure 5.1: (a) The inverse spinel structure of magnetite above the Verwey temperature T_V. (b) A representation of a single trimeron between three iron sites, where the B2 site is shown in blue, two B3 sites are shown in yellow and the surrounding oxygen ions are in red. The light blue lobes represent the orbitals involved in the trimeron interaction while the purple arrows show the associated lattice distortions. (c) Distribution of trimerons throughout the low temperature magnetite lattice. Most trimerons are terminated with B3 sites, forming a complex network, but some must terminate with a B2 site, as shown by the black circle. Figures (b) and (c) are reproduced from (299).

Fierce debate continued (300) until 2012 when Senn *et al.* (299) published a seminal work using high-energy X-ray diffraction on a 40 μm near single-domain grain of magnetite. The authors found that while Verwey's model of charge ordering was correct to a first approximation, the $e_{t_{2g},\downarrow}$ electrons are in fact distributed across linearly distorted three-site units which they dubbed *trimerons*. Here, the $e_{t_{2g},\downarrow}$ electron density is shared between a donor B2 site to two adjacent acceptor sites, which are B3 in most but not all cases (see Figure 5.1b,c), forming weak Fe – Fe bonds accompanied by a small contraction of interatomic distances. Given the 1:1 ratio of $Fe_2{}^+$:$Fe_3{}^+$ ions in the B lattice there are only two sites per $e_{t_{2g},\downarrow}$ electron, meaning that trimerons must share sites (Fig5.1c). The $Fe_3{}^+$ B ions are able to participate in up to three trimerons, forming complex chains throughout the lattice. This results in the $Fe_2{}^+$ sites having a formal valence of ≈ 2.4, while the $Fe_3{}^+$ sites have formal valences between $\approx 2.6 - 2.8$ depending on the number of trimerons they participate in, with the electron density shared equally across individual trimerons. Within the trimerons the B2 and B3 sites remain distinguishable by the distribution of $e_{t_{2g},\downarrow}$ density in their orbitals, with the B3 sites sharing it equally across their t_{2g} orbitals, while the B2 sites retain their orbital order with the $e_{t_{2g},\downarrow}$ density in a single t_{2g} orbital. For the B2 sites, this orbital ordering results in tetragonal Jahn-Teller expansion in 4 surrounding Fe – O bonds which lifts the degeneracy of their t_{2g} levels. Together, these displacements can be thought of as small polarons (SPs).

Trimerons can in fact persist above T_V in the cubic phase, but they are unstable and exist in a disordered glassy network structure. At the Curie temperature they are destroyed by the loss of magnetic order which is required for the weak Fe – Fe bonding. It is these weak bonds that induce and couple to charge and orbital ordering which collectively form the trimerons. The Verwey transition is then described by a localisation of $e_{t_{2g},\downarrow}$ electrons into a 'liquid' of trimerons which coalesce and freeze into a complex ordered network below T_V (301–303). Recently, the discovery of low energy (sub 10 meV) electronic modes has been attributed to

coherent polaron tunnelling through the trimeron network (304).

5.1.4 Electronic Spectrum: Theoretical Descriptions

As briefly discussed in §5.1.3, the electronic states that exist close to the Fermi energy and contribute to conduction are the Fe $3d$ t_{2g} minority spin electrons within the B sub-lattice. The other $3d$ electrons in the B sub-lattice are locked into a high-spin configuration with a large exchange splitting. However, related to the ambiguity in the electron localisation and thereby the crystal structure, there is limited consensus on the dominant method of conduction in magnetite, or indeed the exact nature of the charge carriers involved. Many authors accept that polarons play a role, with recent observations of local correlations in the form of trimerons being a convincing candidate. Two early theoretical approaches were developed by Ihle and Lorenz (305) and Mott (306), respectively, based on differing assumptions about the nature of charge ordering and relative prominence of conduction mechanisms.

5.1.4.1 Mott

Mott proposed that at high temperatures magnetite exists as a 'Wigner glass' where electrons are localised by strong Coulomb interactions and form polarons due to strong electron-phonon interactions, but that these polarons exists in a disordered charge background. The polarons have large effective masses and are mobile within a narrow band giving a metallic conductivity. Upon passing T_V the decreasing thermal energy causes the material to transition into an insulating 'Wigner crystal', where the polarons become ordered into a LRO. The strong Coulomb interactions split the half-filled electronic bands, resulting in insulator-like behaviour at low temperature where transport can only occur via variable range hopping, which follows a $\ln(\sigma) \propto T^{-1/4}$ relation, with σ the conductivity, and polaron tunnelling is frozen out.

5.1.4.2 Ihle and Lorenz

In 1985, Ihle and Lorenz (305) proposed an alternative theory concerning small-polaron (SP) mediated conduction through inter-atomic $3d^6 \longrightarrow 3d^6$ transfers. They proposed that electron-phonon interactions create SPS while strong inter-site Coulomb interactions lead to strong SRO, together forming a *polaronic* SRO. Charge transport may occur via two mechanisms; Franck-Condon like non-diagonal transitions where an electron hops from an occupied to an unoccupied site by absorbing a phonon (without relaxation of the crystal lattice), giving a hopping conductivity σ_h, and diagonal electron tunnelling process with no change in phonon occupation numbers, giving an effective SP band, σ_b. Above T_V the large number of available phonons means polaron hopping σ_h is the dominant conduction mechanism, boosted by the existence of a small band at the Fermi level created due to the thermal destruction of SRO. Below T_V, a near perfect SRO forms, opening a polaronic bandgap and hopping conductivity σ_h is largely frozen out. The DC conductivity should then follow an activated Arrhenius behaviour $\sigma_b = \sigma_0 e^{-E_A/k_B T}$. The authors also propose that at very low temperatures σ_b is

also completely suppressed, and that σ_h, though very weak, again becomes the dominant mechanism. However, they later acknowledged that their theory is only valid for temperatures greater than $T_V/2$ as below this temperature the conductivity is extremely sensitive to impurities and variable range hopping ($\ln(\sigma) \propto T^{-1/4}$) becomes dominant.

5.1.4.3 Limitations

These models have remained popular given that Mott's theory is useful for explaining low temperature observations while Ihle and Lorenz's theory reproduces well the behaviour observed at high temperatures (294). Both agree, however, on the effect of variable range hopping at low temperatures and on the importance of small polarons to the picture, with strong electron-phonon coupling, small radii, reduced mobility and large effective mass. It has since been shown that no one phonon mode dominates the formation of trimerons or SP conduction (299, 307), complicating any simple analytical model. Neither theory addresses the question of the opening of a charge gap Δ in the density of states which has been consistently observed in many experimental works. Gasparov *et al.* (308) note that such a gap could be caused by either an activated carrier density $n = n_0 e^{-\Delta/k_B T}$ or an activated mobility $\mu = \mu_0 e^{W_H/k_B T}$, where the total conductivity $\sigma = ne\mu$, making it difficult to distinguish between these cases. An activated carrier density would suggest semiconductor-like transport through delocalised bands with bandgap Δ, whereas, in the case of magnetite, an activated mobility would be indicative of polaron hopping, with a polaron binding energy $W_H = 2\Delta$. In Mott's view of a metal-insulator transition at least, we should expect there to be no such bandgap above T_V.

5.1.4.4 Computational work

Given the complex crystal structure, large unit cell, variable electron valences and strong contributions from electron-electron and electron-phonon interactions, calculations of magnetite's band structure are particularly challenging. Several computational models have been built to explore the nature of charge-ordering and the band structure of magnetite. By their nature models must make assumptions about or neglect some of the strong electronic, magnetic and structural correlations. They also depend on using the correct crystal structure within their calculations, which has only recently been confirmed as Cc symmetry below T_V (299, 301). Leonov *et al.* (309) used the local spin density approximation with an on-site Coulomb correction (LSDA+U) to model a $P2/c$ low temperature magnetite unit cell. Despite the incorrect symmetry group, they predicted an energy gap of 180 meV which is in good agreement with experimental values. However, they did not reproduce the prominent broad 600 meV feature observed experimentally (see Table 5.1). Jeng *et al.* (310) used the generalised gradient approximation, again with a corrective Coulomb term, (GGA+U) to obtain an energy gap of 200 meV for an experimental Cc geometry. Piekarz *et al.* (300) predicted a bandgap of 330 meV using the same method. Recently, Liu and Di Valentin (311) predicted that an indirect bandgap of 200 meV should exist in the high temperature phase of magnetite due to the effects charge disproportionation and proposed

that transport above T_V occurs via electron small polaron hopping with a similar activation energy.

5.1.5 Electronic Spectrum: Experimental

Many techniques have been used to elucidate the electronic structure of magnetite and how it behaves across T_V. Here, we will concern ourselves only with those measurements which probe excitations relevant for DC conduction, that is, those that lie close to the Fermi level (at energies below 1.5 eV). This broadly limits the relevant literature to those studies which employ optical conductivity (OC), photo-emission spectroscopy (PES), Raman, IR and tunnelling spectroscopies. A list of the experimental works which will be discussed in this section, as well as their findings, is given in Table 5.1.

Date	Author	Technique	$\Delta(T < T_V)$ (meV)	$\Delta(T > T_V)$ (meV)	Excitations (meV)	Ref.
1979	Schlegel *et al.*	OC	n/a	n/a	40, 70, 200, 600	(312)
1987	Degiorgi *et al.*	OC	n/a	None	40, 70, 250, 600	(313)
1995	Chainani *et al.*	PES	70	None	500, 1500	(314)
1997	Park *et al.*	PES	150	100	500, -1000	(315)
1998	Park *et al.*	OC	140	None	600, 40, 70	(316)
2000	Gasparov *et al.*	Raman & IR	200	None	50, 70, 600	(308)
2002	Poddar *et al.*	TS	n/a	n/a	n/a	(317)
2003	Poddar *et al.*	TS	250-350	None	n/a	(318)
2005	Schrupp *et al.*	PES	100-130	50	600 [300, 650]	(319)
2006	Jordan *et al.*	TS	200	200	-450, 500, ±1000	(320)
2008	Lee *et al.*	TS	n/a	n/a	n/a	(321)
2009	Fursina *et al.*	TS	n/a	n/a	n/a	(322)
2014	Yu *et al.*	TS	300	None	600	(323)
2016	Hevroni *et al.*	TS	130-250	75-80	n/a	(324)
2017	Huang *et al.*	RIXS	n/a	n/a	90, 200	(325)
2019	Rakshit *et al.*	TS	n/a	n/a	n/a	(326)
2020	Banerjee and Pal	TS	320	70-80	n/a	(327)

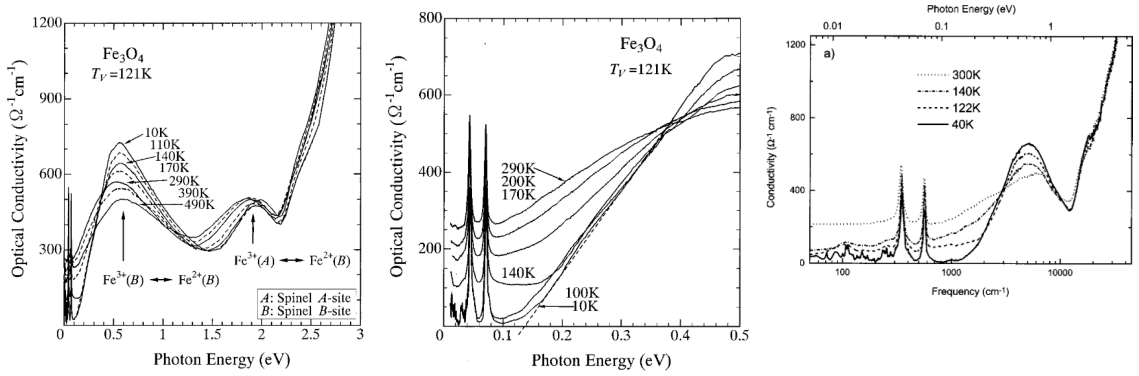
Table 5.1: Overview of relevant experimental works and their findings for the size of the bandgap Δ at temperatures above and below T_V as well as any other notable features.

5.1.5.1 Optical Conductivity

Optical conductivity (OC) is deduced from reflectivity measurements on polished samples via the Kramers-Kronig transformation. Optical conductivity is usually measured in the THz frequency range, and gives information on the energies of optically allowed transitions from one electronic band to another across the Fermi level.

Early optical conductivity measurements on bulk magnetite samples revealed features at 40, 70, 200 and 600 meV (312). The peaks below 100 meV were ascribed to infra-red active phonons, while the peak at 600 meV was attributed the lowest energy d electron interband transition $3d^6 \rightarrow 3d^5 4s$. Degiorgi *et al.* (313) used Ihle and Lorenz's theory to explain their OC data for bulk magnetite taken both above and below T_V. The authors resolved 4 low-energy phonon modes at 10, 30, 40 and 70 meV in addition to a peak near 250 meV and a transition at 600 meV. Using the SP model they interpreted the 250 meV feature as SP hopping

and the 600 meV feature as intersite $d \rightarrow s$ transitions. They also reported on how the fine structure of low-energy phonon modes changed on passing T_V (328), finding that they grew in intensity with decreasing temperatures, attributed to the splitting of modes as the lattice symmetry was lowered. In 1998, Park *et al.* (316) documented the optical conductivity for a bulk single-crystal sample of magnetite. Unlike Degiorgi *et al.* they observed no distinct peak at 200 meV, only that at 600 meV and the two strong phonon modes (Figure 5.2a). The authors attribute the 600 meV peak to intersite $3d\,t_{2g}$ transitions within the B sub-lattice. Below T_V, they noted that the low-energy conductivity (< 100 meV) ceases to be finite and a gap of ≈140 meV opens up (Figure 5.2b). In 2000, Gasparov *et al.* (308) published a similar work where they observed the 50 and 70 meV modes but instead of two distinct modes at 10 and 30 meV they found a forest of peaks in this region. The authors observed how the peaks shifted and broadened with temperature and interpreted the appearance of additional IR- and Raman-active modes across T_V as a sign of structural change. They also observed a principal polaronic peak at 600 meV, which lies at twice the polaron binding energy, and a gap-like decrease in the optical conductivity at energies below 200 meV.



(a) (b) (c)

Figure 5.2: (a,b) Temperature dependent optical conductivity measurements performed by Park *et al.* over different energy scales. Reproduced from (316). (c) Similar measurements performed by Gasparov *et al.* Reproduced from (308).

5.1.5.2 Photo-Emission Spectroscopy

Photo-emission spectroscopy (PES) and inverse photo-emission spectroscopy (IPES) techniques allow for the elucidation of spectra for emission and absorption of single electrons, respectively. In PES the sample is illuminated with a photon source and the energies of electrons emitted via the photoelectric effect are measured. This gives information about states below the Fermi level. Conversely, in IPES the sample is bombarded with a beam of collimated electrons which are absorbed and relax down to the Fermi level through the unoccupied states. The photons emitted from certain relaxations are measured, providing information on the states above the Fermi level. As such, any measured gap in PES spectra will be equal to half the total bandgap, assuming that the bandgap is symmetrical about the Fermi level. PES also importantly shows whether an energy barrier exists or not to promote electrons above the Fermi level, that is, whether the material is an insulator or a

metal, respectively.

In 1995, Chainani *et al.* observed a bandgap of 70 meV which opened upon cooling past T_V = 122 K, characteristic of a metal-semiconductor transition. They found this value to be exactly half of the activation energy measured from the electrical resistivity, E_a = 140 meV. Features were identified at 500 and 1500 meV, which were attributed to emission from majority-spin e_g and minority-spin t_{2g} states of the B sites, respectively (314). These features persist above T_V but merge into a single feature by 300 K. However, in 1997 Park *et al.* (315) performed similar experiments but observed no metal-insulator transition at T_V but instead saw that a 100 meV bandgap also existed above T_V, which then increased by 50 meV to a value of 150 meV below T_V. They proposed that above T_V while LRO is lost some SRO remains, which sustains the bandgap. They justify their conclusion over Chainani *et al.*'s based on the superior monochromaticity of their light source. They assign PES and IPES transitions at 500 meV and 1eV to B2 $d^6 \rightarrow d^5$ and B3 $d^5 \rightarrow d^6$ transitions, respectively. Together, they attribute the gap between these transitions to the effective barrier to charge fluctuations $U_{\text{eff}} = 1 - 1.5$ eV, which they claim is then broadened by orbital overlap to result in the smaller observed 100 meV bandgap.

Using high energy soft X-rays, Schrupp *et al.* (319) were able to probe deeper into their magnetite sample (~ 45 Å) in order to distinguish between bulk and surface effects. They showed that the 600 meV feature was independent of surface preparation and therefore was a bulk phenomena. By comparing their spectra with the density of states calculated by Yanase and Hamada (329), they hypothesised the 600 meV feature may be decomposed into two sub-peaks, one at 650 meV representing the B2$d^6 \rightarrow d^5$ transition and a further polaronic feature at 300 meV of the type derived by Alexandrov and Ranninger (330). Like Park *et al.*, they find that above T_V the bandgap is preserved but is reduced to 50 meV. Their measurements show that for different surface preparations the spectra can change considerably and the Verwey transition may be completely absent. Below T_V, the authors claim that ordering of the polarons forms a gap in the polaronic band and thereby decreases the conductivity. These measurements again point towards the conclusion that the Verwey transition is not of metal-insulator type but instead an insulator-insulator transition.

5.1.5.3 X-ray Scattering

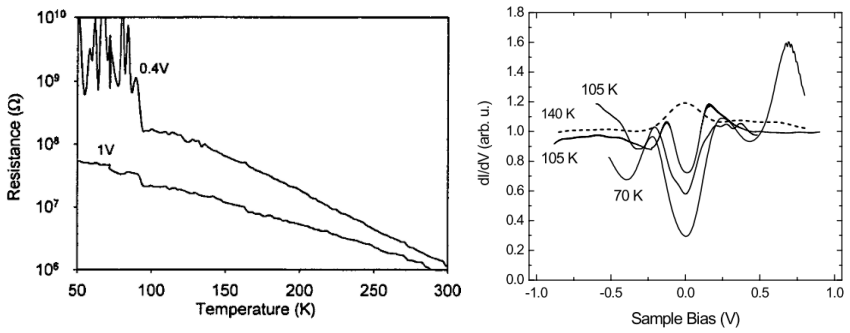
A paper published by Huang *et al.* (325) outlines a series of resonant inelastic X-ray scattering (RIXS) experiments performed across a range of temperatures and energies. They observed resonant excitations at 80 K with energies of 200 and 90 meV and used crystal-field calculations to identify the 90 meV excitation as a B3 spin-flip process, forbidden in optical spectroscopy but allowed in RIXS. They proposed that the broad 200 meV feature is from the B2 ions: formed from a combination of the 90 meV exchange energy, a Jahn-Teller splitting of the t_{2g} levels $\Delta_{t_{2g}} = -26 \pm 4$ meV and a spin-orbit coupling ζ_{3d} of 52 meV. With contributions from a local molecular field as well as Jahn-Teller polaronic distortions, the authors conclude that the observed excitations are magnetic polarons.

5.1.5.4 Tunnelling Spectroscopy

Tunnelling spectroscopy (TS) affords higher resolution of low lying electronic states than the above methods and it also offers the possibility of studying nanoscale systems. TS also provides information on both the occupied and unoccupied electronic states, unlike PES or IPES alone, and can probe optically forbidden transitions.

In 2002, Poddar *et al.* (317) reported on the electrical transport behaviour through devices formed from stacked monolayers of 5.5 nm magnetite nanocrystals sandwiched between lithographically patterned gold electrodes. The nanocrystals were coated in oleic acid in order to pacify any grain boundary or surface states. A Verwey transition was observed despite the likely off-stoichiometry at the surface due to the large surface-to-volume ratio of the particles, however it occurred at 96 K rather than the bulk value of 121 K. The authors also noted how the Verwey transition is most pronounced at low biases due to the non-linearity of the current, as shown in Figure 5.3a, and reported on the temperature dependence of the magnetoresistance at temperatures above T_V, but observed no effect below. The next year, Poddar *et al.* (318) reported scanning-tunneling microscopy measurements on single sub-10 nm magnetite nanocrystals on a gold substrate. The authors formed a highly asymmetric double-barrier tunnel junctions by retracting the scanning tip as far as possible in order to reduce single-electron charging effects. Still, 60 % of their devices displayed charging effects which masked the inherent density of states of the nanocrystals. Of the 14 devices which did not show charging effects, 11 exhibited a Verwey-like transition, with transport gaps of 250-350 meV at temperatures below T_V, significantly larger than those previously reported for bulk samples. They found that above T_V this gap closed and instead a peak formed at the Fermi level (see Figures 5.3b). The authors claim that the main features in their data were reproducible but that the background fluctuated across measurements. They found the gap to be resilient against changes in bias and current and saw no signature of equidistant peaks, which would be indicative of single-electron charging effects, suggesting that the gap was intrinsic to the nanocrystal DOS. The authors posited that broadening of the gap could be due to an unknown size effect or to voltage division inherent in the double tunnel junction configuration (331–333). They concluded that the bandgap below T_V was evidence for LRO existing in the nanocrystals despite their small size, but noted that the absence of a SRO bandgap above T_V, as reported by Park *et al.* (315) and Gasparov *et al.* (308), was puzzling.

In 2006, Jordan *et al.* (320) performed scanning-tunnelling measurements on the (001) and (111) surfaces of a single crystal of magnetite. They found that the bandgap near the Fermi level remained of a similar size across T_V, but that the shape and position of satellite occupied and unoccupied bands changed markedly. They observed a 200 meV bandgap and a shoulder-like feature at +500 meV at room temperature, and a second shoulder at -450 meV that appeared at 140 K as temperatures were lowered, prior to T_V. Overall, this gave an effective charge fluctuation barrier of $U_{\text{eff}} = 0.95 \pm 0.2$ eV, comparable to that found in (315). They showed that local disorder on the surface could drastically change the tunnelling behaviour, or even close the band gap completely. On cooling the samples below T_V they found the bandgap at the surface was unchanged, but



(a) (b)

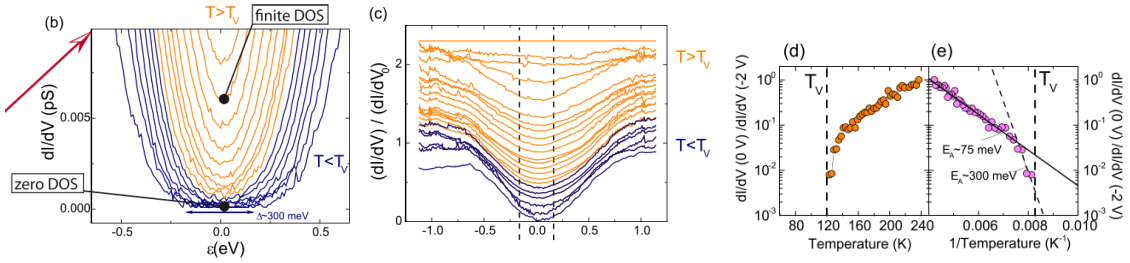
Figure 5.3: (a) Dependence of the electrical resistance on temperature and bias voltage. Reproduced from (317). (b) Evolution of conductance-voltage traces of single nanocrystals at different temperatures. Reproduced from (318).

that the satellite peaks shifted further from E_F to give a $U_{\text{eff}} = 2 \pm 0.4$ eV. This suggested that any conductivity decrease at the surface is not due to the opening of a larger band gap completely devoid of states but is instead due to the formation of a larger area of limited density of states around E_F as the d-bands shift to higher energy. The authors therefore conclude that complete charge ordering below T_V, which would inhibit electron hopping, does not occur (at least at the surface) but that instead the barrier to hopping increases.

In 2008 Lee *et al.* (321) reported the observation of resistive switching in magnetite nanocrystals and thin films below T_V induced by an electric field. The voltage at which the switching occurs is intrinsic to the sample, increasing with decreasing temperatures, and the switching power decreases with decreasing temperature, suggesting that the transition is not driven by Joule heating of the sample above T_V. The switching voltage is also dependent on the dimension of the sample, increasing for larger samples. The authors went on to show using pulsed voltage measurements that while the switching was intrinsic the observed hysteresis was not and the hysteresis was caused by Joule heating in the highly resistive state (322). No gate modulation was seen and switching characteristics were found to be independent of a perpendicular magnetic field. The authors also noted that contact resistances may play a significant role in the transport through their devices.

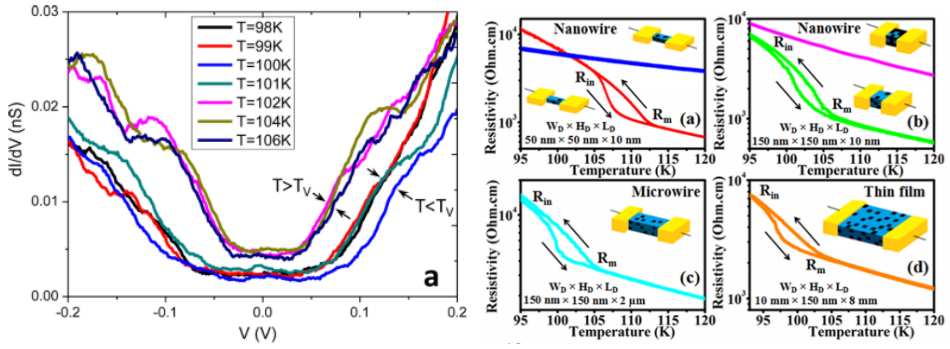
In 2014, Yu *et al.* (323) presented a paper on the tunneling spectra of a single magnetite nanocrystals trapped between gold nanogap electrodes. The authors note that if a bandgap in the density of states is observed above T_V, which has not been consistently shown in previous works, then this would support a description of magnetite as a semiconductor. While they observe a 300 meV bandgap below T_V (see Figure 5.4a) and infer a 75 meV activation energy above T_V (see Figure 5.4c), the authors do not observe a bandgap in the density of states above T_V (see Figure 5.4b) and thus conclude that the activation law is due to activated mobility from polaron hopping, in contrast to that seen by Park *et al.* (315) and Schrupp *et al.* (319). In order to describe the polaronic behaviour they use the model proposed by Lundin and McKenzie (334). However, this model considers only a single localised electronic level coupled to a single boson mode which is not appropriate in the case of magnetite which does not have a discrete density of states and where transport is achieved through polaron migration throughout the lattice. Their IV data fits poorly to the theoretical

curve produced using this model and their claim of observing a localised polaronic state at 0.6 eV, as seen by other authors, is unconvincing. The authors further claim that the bias dependence of the Verwey transition is due to the Debye screening length exceeding the dimension of the nanocrystals at temperatures below T_V, subjecting the nanocrystals to large electric fields which drive out-of-equilibrium effects. This would make the interpretation of tunnel characteristics from low temperature IV curves difficult. Interestingly, the authors observe no switching behaviour in their highly resistive devices like that seen by Lee *et al.* in their less resistive planar devices.



(a) (b) (c)

Figure 5.4: (a) Conductance as a function of bias voltage $\varepsilon = eV_b/2$, showing a finite DOS at T > T_V and zero DOS at T < T_V. (b) The same data normalised to the trace taken at 240 K to show the DOS of the magnetite. (c) Arrhenius plots of the zero bias conductance, normalised against the conductance at -2 V. Far above T_V the data fits an activation energy of 75 meV, whereas on approaching T_V this increases to 300 meV. Below T_V the conductance is lower than the noise floor of the current amplifier. Figures reproduced from (323).



(a) (b)

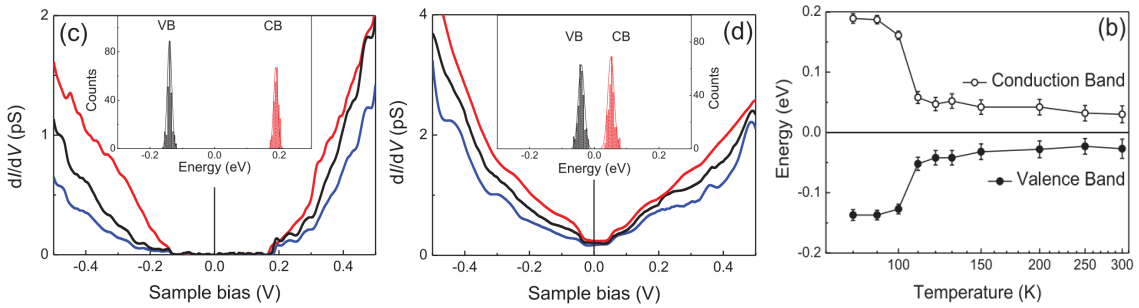
Figure 5.5: (a) Differential conductance as a function of temperature for a single magnetite nanocrystal, reproduced from (324). (b) The resisitivity of various magnetite thin film devices of different dimensions and defect concentrations, represented by the graphics in the panels, reproduced from (326).

In 2016, Hevroni *et al.* (324) published on variable temperature STM measurements on single 10 nm magnetite nanocrystals embedded in a gold film to allow for continuous measurement of the same nanocrystal. They observed a significant change in the transport at 101 K for 5 of the 15 measured nanocrystals, with a bandgap of 130-250 meV below T_V and a reduced *pseudogap* of 75-80 meV above T_V with indications of some small finite density of states within the gap as seen in Figure 5.5a. They note that these changes were not observed in topography scans at constant temperature, concluding that they are associated with the Verwey transition and not a factor of tip position. The authors employed small tunnel currents in order to maintain

large sample-tip separations to protect the tips from contamination and to create highly asymmetrical tunnel junctions. They found that when reducing the tip-sample resistance the IV curves would vary, which they attributed to additional transport modes such as hopping competing with resonant tunnelling, obscuring the nanocrystal's density of states. They attribute the range of observed bandgaps below T_V to variations in stoichiometry or defects in the nanocrystals as any LRO, dominant below T_V, would be more sensitive to surface defects than the SRO which dominates above T_V.

Rakshit *et al.* (326) published a study in 2019 on epitaxial magnetite nanowires using a novel fabrication technique. They found that the Verwey transition is preserved down to the 10 nm length scale despite the inevitable presence of defects and that the transition temperature increases again to 112 K for nanowires with volumes on the order of 10 nm^3, accompanied by a significant increase in the ratio of resistances before and after the transition (see Figure 5.5b). By confining the magnetite to length scales smaller than that of the typical average grain size they were able to effectively exclude extrinsic domain wall and grain boundary defects from some nanowire structures. They used magneto-resistance measurements to confirm that anti-phase boundaries were the dominant form of defect affecting the transport. Due to the statistical distribution of anti-phase boundaries half of their nanowire devices displayed strong Verwey transitions with large resistance ratios and smaller magneto-resistance values, whereas the other half showed no Verywey transition but larger magneto-resistance values due to the presence of multiple defects. For larger scale devices they saw little variation due to the isotropic distribution of anti-phase boundaries throughout the device. The authors attribute the observed hysteresis in the resistance-temperature measurements to intrinsic defects in the samples which oppose electronic ordering upon cooling past T_V but do not oppose disordering in reverse. Defects will create electronic states which interrupt both the conductive and insulating states through scattering and donation. The authors find that their data for low-defect nanowires fits a model for variable-range hopping and they extracted a coherence length which matches well with the size of a trimeron (299).

Most recently Banerjee and Pal (327) reported a scanning tunneling spectroscopy study on magnetite nanocrystals on a gold substrate. Specifically, the authors were attempting to answer the question of whether the conduction and valence bands shift equally during the opening of the bandgap opening at T_V. They found a T_V to be 110 K for their 6 nm diameter nanocrystals and observed a bandgap of 320 meV below T_V and a pseudogap of 70-80 meV with a finite density of states (see Figures 5.6a and 5.6b). The authors report that the valence band lies closer than the conduction band to E_F and that the conduction band edge moves further than the valence band edge through the Verwey transition (see Figure 5.6c). They attribute this to the contribution of anti-bonding Fe $3d$ and O $2p$ orbitals to the conduction band, which are more affected by the Verwey transition than the non-bonding O $2p$ orbitals in the valence band.



(a) (b) (c)

Figure 5.6: (a) Differential conductance measured at 80 K for a single magnetite nanocrystal. The blue, black and red lines represent different set-points of 40, 60 and 80 pA, respectively at 600 mV. (b) Differential conductance measured at 130 K. (c) The positions of the conduction band (positive voltage) and valence band (negative voltage) edges as a function of temperature. Figures are reproduced from (327).

5.1.6 Summary

To summarise, measurements performed over the last 50 years have provided a variety of data points on fundamental properties of magnetite. A consensus has been reached that charge ordering manifests in three-site trimerons which crystallise into a long range order at the Verwey temperature causing a change in the crystal structure. The complexity of the crystal structure and the strong correlations within the material make modelling very challenging. Below T_V, multiple experiments using an array of methods have observed an electronic bandgap around the Fermi level, but no consensus has been reached about whether this gap reduces at T_V or vanishes. It is clear from the literature that the purity and preparation of magnetite can affect its properties greatly, particularly for nanoscale particles with large surface to volume ratios. DC transport through magnetite is largely agreed to be polaronic in nature but interpretations of transport features observed in nanoscale systems remain inconclusive.

5.2 Methods

5.2.1 Nanoparticle selection

For this study we used a commercially available solution of magnetite nanocrystals (MNCs) purchased from Ocean Nanotech. The selected MNCs were 25 nm in diameter, with a monolayer oleic acid coating and were suspended in chloroform. The oleic acid coating helped to stabilise the MNC solution and prevented oxidation of the underlying magnetite. The MNCs are synthesised via a process of thermal decomposition of iron carboxylate salts (335). We chose the nominally 25 nm diameter particles based on four factors:

- the scaling of the dielectrophoretic force with particle volume,
- the uniform size distribution offered by this manufacturer (±2.5), enabling comparisons between devices where size effects may dominate,

- the limiting resolution of our SEM with which we assess the success of the experiments, and,
- the manufacturer's specification that only particles with diameters greater than 10 nm would be primarily composed of magnetite rather than $Fe_2{}^+$ deficient maghaemite ɣ-Fe_2O_3.

However, a recent study (336) characterising a range of amine functionalised magnetic nanoparticles from Ocean Nanotech found that particles of all sizes were composed of a mix of ɣ-Fe_2O_3 and Fe_3O_4. The authors also found that particles with diameters of 25 nm or greater showed a small remnant magnetisation, whereas the smaller particles were superparamagnetic, as expected. The authors did not comment on the ratio of maghaemite to magnetite and how this may affect the magnetisation, but it is possible that the particles are composed of a core of Fe_3O_4 surrounded by a shell of γ-Fe_2O_3 (337). Other studies have found that any Verwey transition is significantly suppressed in spherical MNCs as opposed to octahedral MNCs where the transition remains pronounced due to better surface coordination and therefore fewer defects (338).

5.2.2 Dielectrophoresis

The experimental methods used in this study follow those reported in detail in the previous chapter. An apparent challenge of working with magnetite MNCs was the low dielectric constant of choloform, as the dielectrophoretic force is directly proportional to the dielectric constant ε_m of the solution, which for chloroform ($\varepsilon = 4.8$) is significantly smaller than that of water. Magnetite has a dielectric constant in excess of 10^3 at room temperature (339), meaning that the Claussius-Mossotti function is equal to 1. Given that the dielectrophoretic force $F_{DEP} \propto v\varepsilon_m V^2$ and that a peak voltage (V_p) of 0.75 volts was required to trap gold nanorods of similar volume v, initial calculations suggest that voltages in excess of 2.1 V may be required to capture the selected MNCs, but such voltage levels were known to degrade the nanogaps. I considered boosting the dielectric constant of the solution with the addition of dichloromethane ($\varepsilon = 9.1$) or methanol ($\varepsilon = 33$), which is miscible with chloroform, however the impact this would have on the stability of the suspension was unknown and I lacked access to the equipment or expertise to quantify it so the solution was used without modification.

The particles were supplied at an approximate concentration of 1.4 nmol mL^{-1}. I diluted the nanoparticles 1000× in chloroform to achieve a solution of concentration 1 pmol mL^{-1}. A two-terminal chip with remote finder electrodes was prepared with electroburned graphene nanogaps. This device configuration allowed the trapping signal to be applied to all devices simultaneously as the chloroform would rapidly evaporate. The chips were wire-bonded to a suitable chip carrier and mounted into a custom break-out box which allowed the me to control which devices were exposed to the trapping voltage. A 2 μL droplet of the diluted solution was deposited onto the chip which was immediately connected to an alternating voltage of 0.75 V_p at 1 MHz, the same parameters which were optimal for the capture of gold nanoparticles. One challenge of working with chloroform is its high volatility, resulting in the solvent evaporating within a matter of seconds and all

suspended particles being deposited onto the chip surface. The result of this experiment with a 1 pmol mL^{-1} solution can be seen in Figure 5.7. Large deposits of MNCs cover the chip surface, however, MNCs do appear to have been captured at the nanogap despite the low dielectric constant of the solvent.

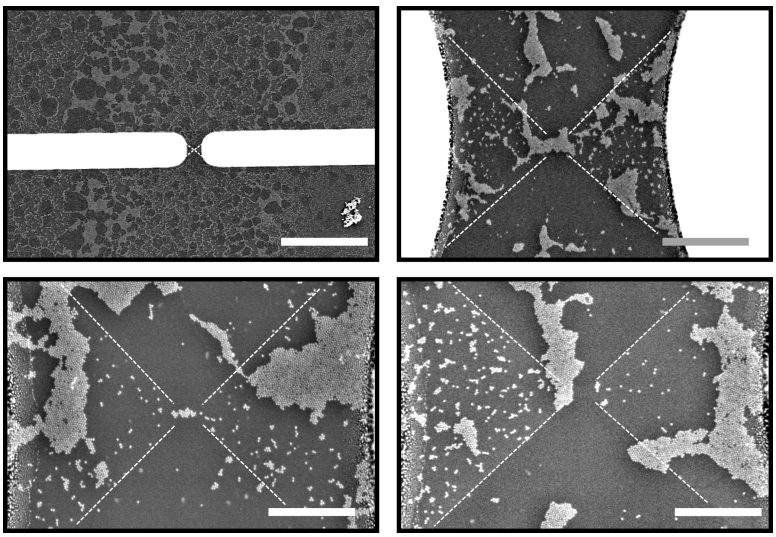


Figure 5.7: The results of depositing a 1 pmol mL^{-1} MNC solution onto patterned devices using a trapping voltage of 0.75 V_p at 1 MHz for all panels apart from the bottom right panel, where no trapping voltage was applied. The white dashed lines show the edges of the graphene electrodes. Scale bars represent 25, 2.5, 1 and 1 μm from left to right, top to bottom, respectively.

The procedure was repeated without applying any trapping voltage across the chip to check that the observed deposition was not the result of some surface interaction. As can be seen in bottom right panel of Figure 5.7, while the nanoparticles appear to have an affinity for the graphene surface and for clustering, they have not been deposited over the nanogap in the absence of an applied voltage. This suggests that diffusion and evaporation play an important part in drawing nanoparticles towards the graphene electrodes but that the dielectrophoretic force is responsible for capturing them at the nanogap.

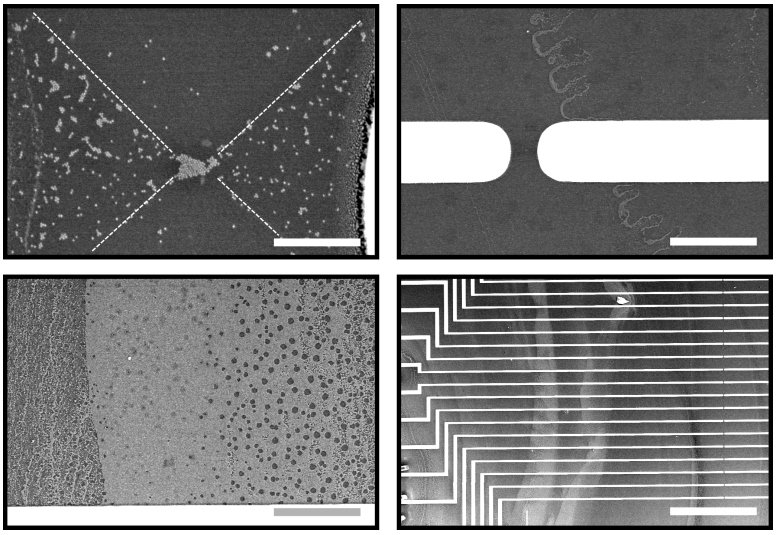


Figure 5.8: SEM images showing MNCs at 1 fmol mL^{-1} trapped at the nanogap (top left) and dispersed across the chip surface. Scale bars represent 1, 20, 20 and 500 μm from left to right, top to bottom, respectively.

The results shown in Figure 5.7 suggested that further dilution of the nanoparticles would be needed to realise capture of single nanoparticles. However, this must be carefully balanced with the evaporation behaviour of the solvent, which wicks away from the centre of the chip (where the nanogaps are located) as the solvent dries. At a concentration of 1 fmol mL^{-1}, a smaller but still sizeable cluster of nanoparticles was captured across nanogaps under the same trapping conditions, and with large deposits of nanoparticles across the wider chip (see Figure 5.8). However, further experiments with 1.4, 14 and 140 amol mL^{-1} concentrations resulted in no trapping of particles. Furthermore, on conducting further experimental runs I found that the quality of the suspensions began to degrade, and no MNCs were observed after depositing the fmol mL^{-1} solution. This suggests that the MNCs were crashing out of solution over time, however no deposits were visible in the sample tubes. As such, I decided to proceeded with the pmol mL^{-1} solution to give the best chance of particle capture, despite the risk of MNC clusters.

5.2.3 Annealing

Once deposition had been achieved, the next challenge was to establish good electrical contact between the nanoparticles and the graphene electrodes. In a 2019 paper by Song *et al.*, the authors explored the proximity-induced influence of a monolayer of Fe_3O_4 nanoparticles on a graphene electrode. After forming a nanoparticle monolayer, the authors established contact between their oleic acid-coated nanoparticles and the graphene with a rapid thermal annealing step to break down the organic coating via pyrolytic dissociation (see Figure 5.9a,b). Their annealing step consisted of a 30 minute, 300 °C anneal under a forming gas environment.

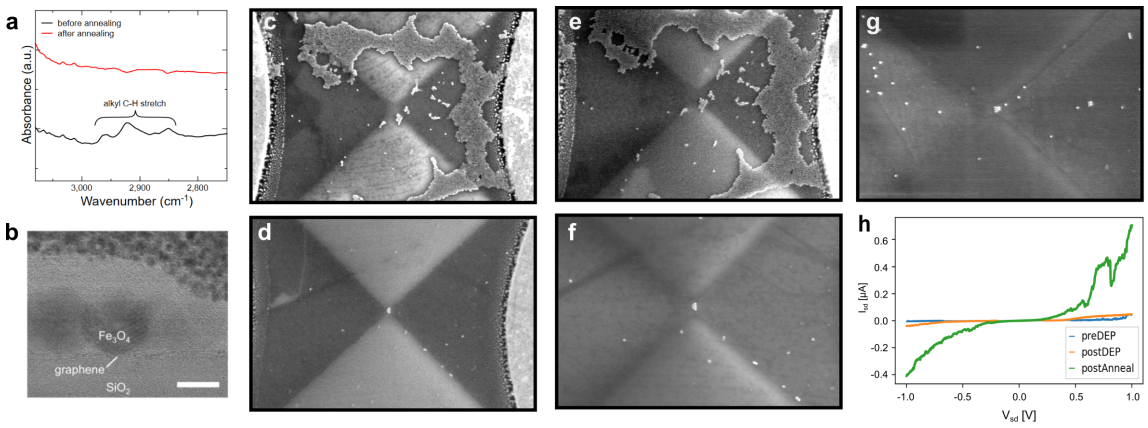


Figure 5.9: (a) Fourier transformed infrared spectroscopy measurements of MNCs before and after annealing to remove the oelic acid coating. (b) Cross sectional TEM image of annealed MNCs on graphene. Reproduced from (237). (c-f) SEM images showing MNCs captured over graphene nanogaps and annealed at 440 °C. (g) An SEM image after annealing at 300 °C. (h) IV characterisation before DEP, after DEP and after annealing at 300 °C.

Given the success of the annealing step in establishing contact between the gold nanorods and graphene electrodes described in the previous chapter, I attempted to replicate Song *et al.*'s process. Using a tube furnace, I flushed a quartz tube with 2000 SCCM of argon gas for 10 minutes to purge any oxygen. I then

turned off the argon flow and inserted a chip with deposited nanoparticles in a ceramic boat to the centre of the furnace. Argon was then flowed through the furnace for a further 10 minutes. Once the tube was purged, the gas flow was changed to a mixture of 950 SCCM of argon and 50 SCCM of H_2 to create a reductive forming gas environment. The tube furnace was initially configured to heat to 300 °C at a rate of 100 °C per minute and hold for 30 minutes once the target temperature was reached. However, this rate led to an overshoot to 440 °C and so the rate was reduced to 30 degrees/minute for subsequent runs, which resulted in a peak temperature of 321 °C. After 30 minutes the furnace was allowed to cool to room temperature. Devices used in the first test (to 440 °C) were imaged in an SEM before and after the annealing step and can be seen in 5.9c-f. As can be seen in the Figure, the nanoparticles appear unchanged in morphology after heating to 440 °C, but show improved in contrast, while the graphene itself appears cleaner. Figure 5.9g shows a typical device after annealing at 300 degrees. Figure 5.9h shows the change in electrical response of the same device. The substantial increase in conductivity after the annealing step is clearly associated with the deposition of nanoparticles across the nanogap region, in line with the findings in the previous chapter.

Magnetite will oxidise to maghaemite or hematite when exposed to oxygen, and so it was necessary to minimize the exposure of the samples to air after the annealing process. Once the furnace and samples had cooled to near room temperature the tube was flushed with 2000 SCCM of argon again for 5 minutes to remove any remnant H_2. The gasses were then switched off and the furnace was opened. The sample was removed, mounted in a puck, loaded into the cyrogenic Puck Tester which was then evacuated with a vacuum pump as quickly as possible.

5.3 Results and Discussion

In this section, I will outline the experiments performed on MNC devices and the results therein. In total, I obtained transport data for 14 devices, each of which has been assigned a letter **A**-**N** as a label. Initial electrical transport measurements were carried out at 3 K. From previous transport studies and, in particular, from the work done by Yu *et al.*, I was expecting to observe a sizeable transport gap on the order of $\Delta \sim 300$ meV (318, 320, 323, 324, 327). I was also looking out for electric field induced (Joule heating driven) switching and hysteresis, as observed by Lee *et al.* (321) in magnetite thin films.

5.3.1 IV behaviour

Figure 5.10 shows IV traces measured for each device taken at 3 and 300 K as well as SEM images of each device taken after all measurements had concluded, where available. While there is a large variance in the IV traces across the devices shown in Figure 5.10, there are several striking features which reoccur: apparent transport gaps at low bias voltages, modulation in the current with increasing biases, asymmetry of the current at positive and negative biases, and, finally, evidence of hysteresis in several devices.

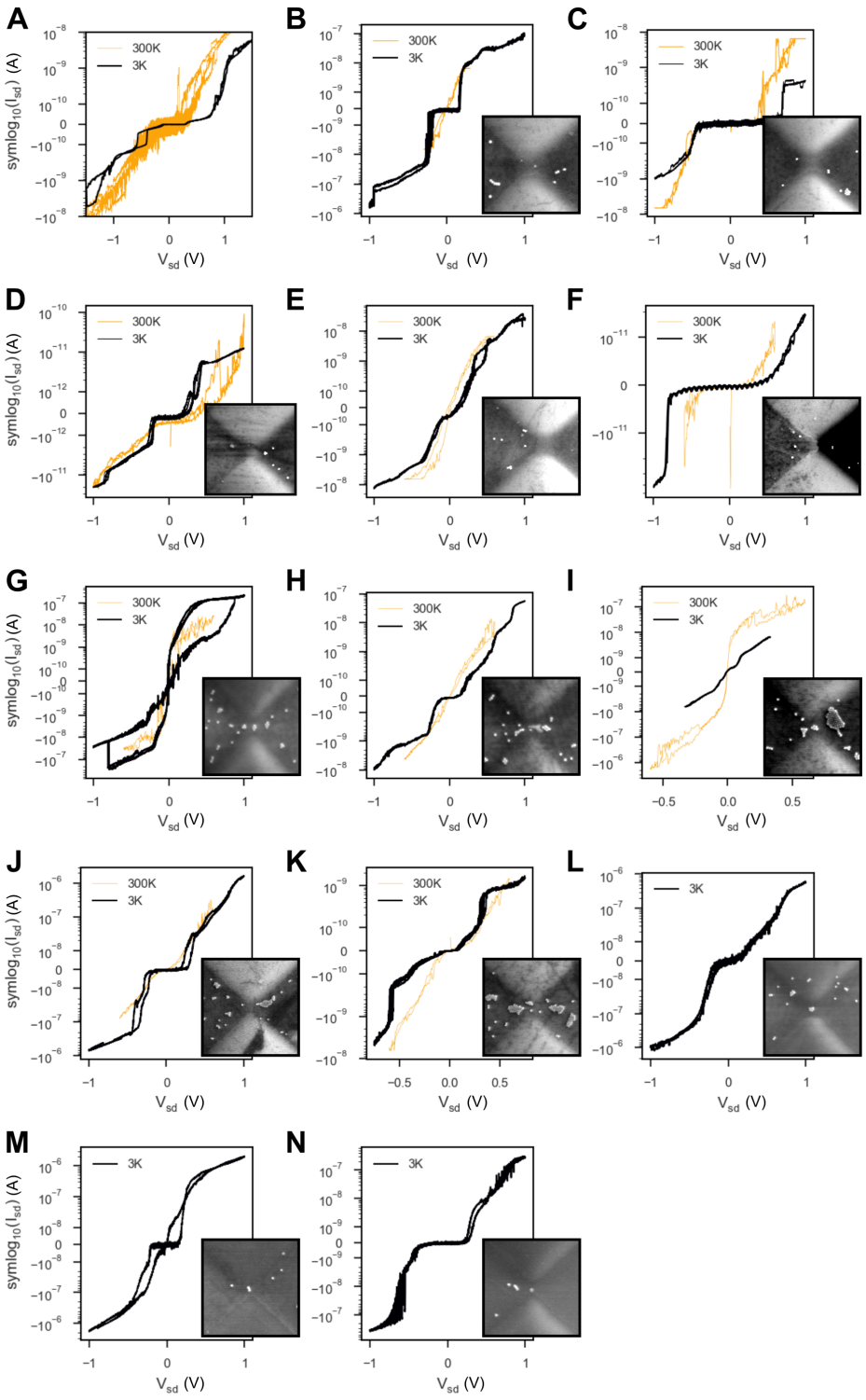


Figure 5.10: IV traces taken at 3 and 300 K, where available. The IVs are plotted on a symmetrical logarithmic scale where the centre regions around zero is linear. SEM images of each device are included with all devices bar **A**, which were taken after all electrical measurements had been completed.

I performed a series of measurements in order to first address whether the hysteresis was due to Joule heating as previously reported (321, 322). For device **A** I swept the bias at several different rates, allowing the device to relax between measurements and changes in the bias direction. I observed no hysteresis at positive biases at any rate, while for negative voltages there was no consistent difference in the hysteresis

for between different sweeo rates. For hysteresis to be driven by an electric field and maintained by Joule heating we would expect the initial transition voltage to be constant (322), irrespective of the sweep rate. The fact that this was not observed indicates that the observed hysteresis arises from a different mechanism to that observed by Lee *et al.* In order to better understand the hysteresis and the states that were being switched between I performed sequential IV traces in order to build 2D histograms of the most common IV traces. Such histograms were collected for devices **A** and **B** and are shown in Figure 5.11. For device **A** we see that at positive bias hysteresis is minimal, but that a high current pathway exists, alongside some activity within the gap region near zero bias. At negative bias, two pathways appear to exist which create two small regions of hysteresis. For device **B**, hysteresis is clearly evident at positive voltages, where the traces show similar features but are shifted in bias and current, similar to the effect of a change in background charge. At negative bias the picture is much less clear, with the current tracing a range of values spanning several orders of magnitude. Both of these histograms show that any one IV trace measured for any one nanocrystal likely represents only a sample of a range of behaviour, meaning that the allocation any given feature at a set energy will come with uncertainty.

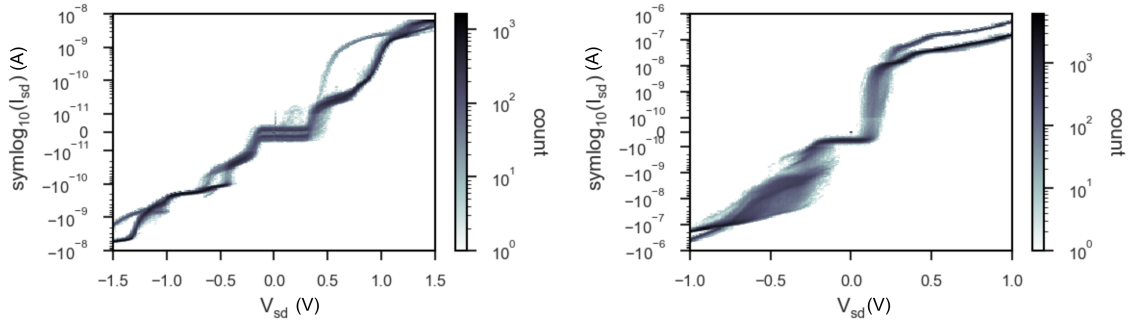


Figure 5.11: 2D Histograms of current values seen in repeated IV cycles for devices **A** (left) and **B** (right).

Measurements on another device which showed prominent hysteresis, device **N**, showed that the path that the current followed depended on the direction in which the bias was being swept. From Figure 5.12 we see that, starting from zero bias the current increased quickly before plateauing at high voltage. As the voltage changed direction the current suddenly increased dramatically before quickly decaying to zero. Passing zero bias towards negative voltages the device shows the same behaviour, where the current rises and plateaus before switching to a high conductivity state when the voltage changes direction. This series of measurements was repeated but in reverse as shown in the second panel, but now the device appeared to be 'set' into the low conductivity states at negative bias, but switched again at positive bias. The third panel of the figure shows how the device ultimately remained set in the 'high' conductivity state, with no further hysteresis being observed. This behaviour is reminiscent of resistive switching, a technology of great interest for increasing the efficiency of computing (340). We can see from the SEM images in Figure 5.10 that devices **B** and **N** are formed from single MNCs, unlike many other devices for which some have multiple MNCs at the nanogap.

This may explain why this strong hysteresis behaviour is not seen for all devices but suggests that it may be an intrinsic feature of MNCs.

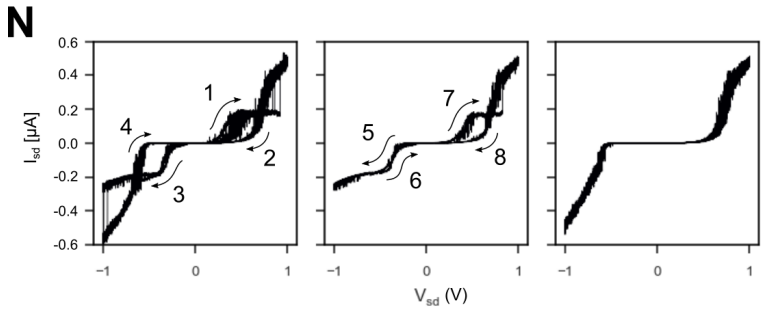


Figure 5.12: Hysteresis observed in device **N** during IV measurements. The numbers and arrows represent the order and direction of the voltage sweep.

5.3.2 Gate Dependence

Stability diagrams, such as the ones shown in Figure 5.13, are a useful tool in assigning the dominant conduction mechanism. For the devices discussed in this chapter there is no local buried gate electrode but instead devices are gated via applying a gate voltage to the backside of each chip: a global gate. However, because the oxide on which the devices sit is 300 nm thick and has a relatively low dielectric, constant much greater voltages are required to achieve the same gate effect as locally-gated devices. Large gate voltages risk gate-leakage through the oxide or even within the multi-core cables that connect the devices to the measurement instruments. Unfortunately, our 3 K measurement setup was not suited to large gate voltages without significant leakage currents and as such the stability diagrams are limited to a ±30 V or smaller window.

Figure 5.13 shows a series of stability diagrams taken for devices **A**-**F** which showed minimal gate leakage. Each diagram has been split into an increasing V_{sd} and decreasing V_{sd} component to highlight any hysteretic behaviour. We see that devices **A**, **B** and **E** show little dependence on the gate voltage, albeit across a narrow range, while devices **C**, **D** and **F** show typical Coulomb blockade behaviour. As transport through magnetite is theorised to occur through hopping or band-like tunnelling and not through a single energy level we do not expect magnetite to intrinsically display blockade behaviour. However, given the size of the MNCs and the characteristically weak coupling found in graphene nanogap devices (92) we might expect that blockade to manifest in some devices, as reported by other authors (318).

To identify the source of the Coulomb blockade it is useful to look ahead at the SEM images acquired after experiments had completed. While the graphene nanogap itself cannot be resolved in an SEM image, it is most likely to be located at the narrowest point between the two graphene electrodes: the constriction. From the SEM images shown in Figure 5.10 we see that devices **C** and **F** have no MNCs occupying the region around the constriction. Device **D** seems to have a fold in the graphene which passes directly through the constriction, indicating that the nanogap has not likely been fully formed. We can also see a trio of MNCs

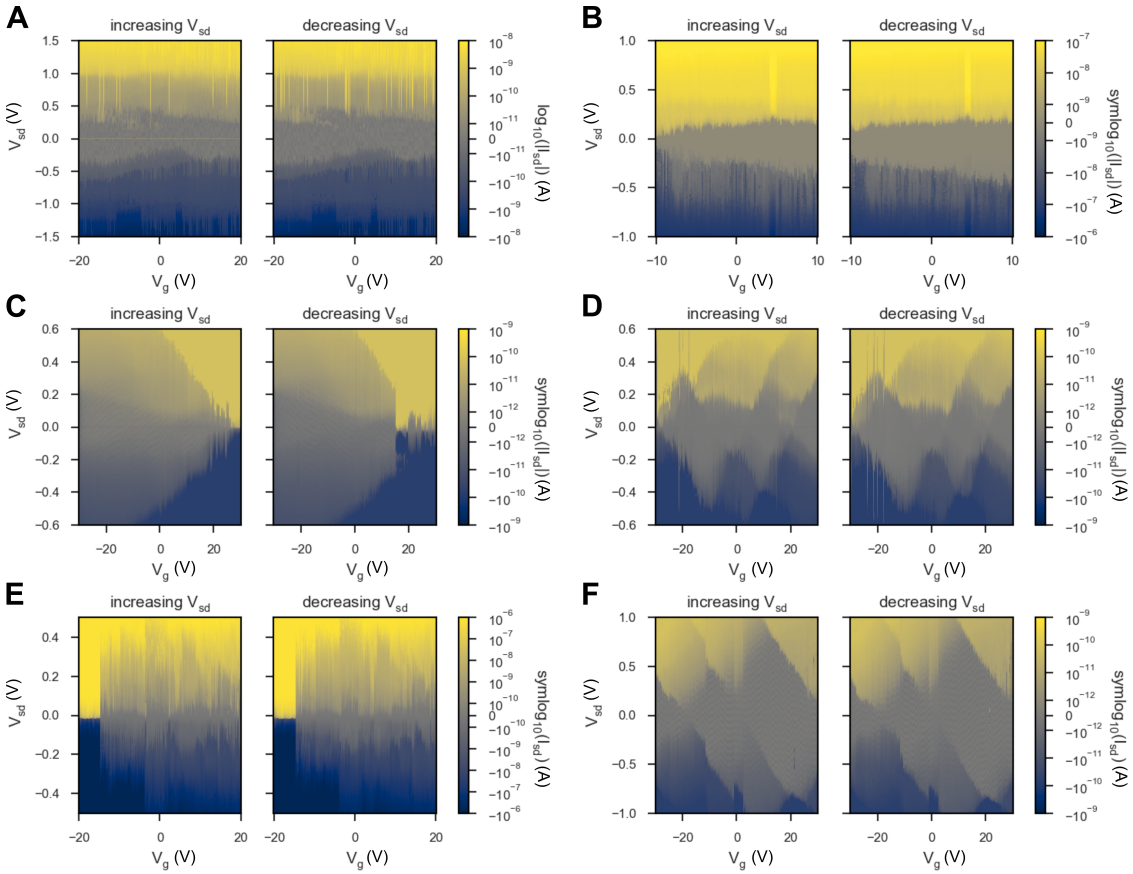


Figure 5.13: Stability diagrams for devices A-F at 3 K with the increasing and decreasing voltage sweeps separated.

sitting to the right of the constriction which may still influence the transport behaviour. Device **B** has a single MNC at the nanogap position, while for device **E** we can see that a crack in the graphene to the left of the constriction, which is likely where the nanogap formed during electroburning. At the edge of the crack at this nanogap sits a dimer of nanocrystals.

Comparing these findings to the stability diagrams it is clear that Coulomb blockade occurs in devices which do not appear to be bridged by MNCs, while for the devices which are bridged by MNCs we see little gate dependence. The three blockaded devices also all show similar currents, notably lower than those in **A**, **B** and **E**. As discussed in Chapter 2, we know that graphene constrictions themselves frequently give rise to irregular Coulomb blockade and that graphene quantum dots can be produced during the electroburning process and the behaviour seen in **C**, **D** and **F** is characteristic of such devices. Interestingly, the central resonance in device **D** appears to show bandgap-like behaviour alongside blockade, where one behaviour usually precludes the other. As observed in the SEM, the close proximity of a trio of MNCs to the graphene filament may have created a hybrid system resulting in two competing pathways, one showing single-electron tunnelling and another with a bandgap. In any case, while graphene quantum dots or single electron charging may too exist in devices **B** and **E**, their contribution to the transport is washed out by a much stronger contribution from transport through the MNCs which occupy the nanogap. As such, we exclude devices **C**, **D**

and **F** from further consideration and conclude that the MNC devices show no significant gate dependence.

5.3.3 IV comparison

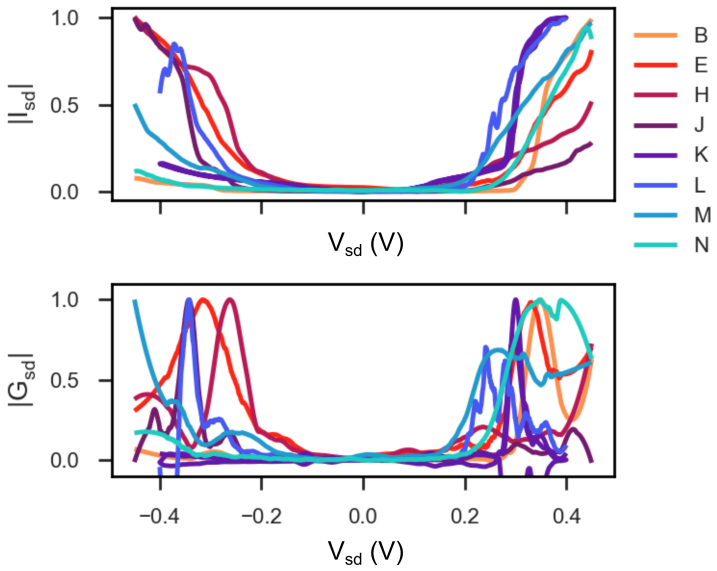


Figure 5.14: Comparison of normalised IVs and the differential conductance for devices B, E, H, J, K, L, M and N showing a bandgap of approximately 200-300 meV.

Figure 5.14 shows an overlay of normalised IVs and their numerical derivatives for a selection of devices. Despite the variability, we see that significant features exists at ±200-300 meV exist across all devices, suggestive of a bandgap of the same size. This is consistent with the most commonly reported values in the literature (see Table 5.1) and those predicted computationally. We also see evidence of smaller features within the bandgap, suggesting that this may be a pseudogap region of limited but finite density of states, which may account for why several authors have reported smaller bandgap values.

5.3.4 Magnetic Field Dependence

Spintronics is a subject of great interest and the ability to interface graphene, with it's long spin diffusion length, with spin active materials is an attractive target for the realisation of spintronic devices (204, 237, 341). Electrical transport through magnetite should, in theory, be 100% spin polarised as only the minority spins within the B sub-lattice are mobile below the Curie temperature, T_C. Below T_C, magnetite behaves as a ferrimagnet where the magnetic moments of the A and B ions, unequal in magnitude, freeze into an anti-aligned configuration leading to a net magnetisation. At the Verwey transition, the magnetic easy axis switches from the $\langle 111 \rangle$ direction to the $\langle 100 \rangle$ direction (338). The magnetisation direction of ferrimagnetic particles composed of a single magnetic domain can be flipped along the magnetic easy-axis given sufficient thermal energy $T \geq T_B$, the blocking temperature. Above this temperature magnetite behaves as a super-paramagnet. For sufficiently small particles, ($d \lesssim 10$ nm (342)), the blocking temperature reduces to below

T_V, eliminating the Verwey transition. At such sizes, the easy axis of magnetisation is strongly influenced by anisotropies within the particles and interactions with any neighbouring particles which can result in multiple possible orientations for the magnetisation to occupy above T_B (317, 343). Below T_B this flipping freezes out and the magnetic moment becomes fixed again in one orientation, restoring ferrimagnetic behaviour. The MNCs used in this study are large enough that their blocking temperature should be much greater than T_V and the particles should be ferrimagnetic (344, 345).

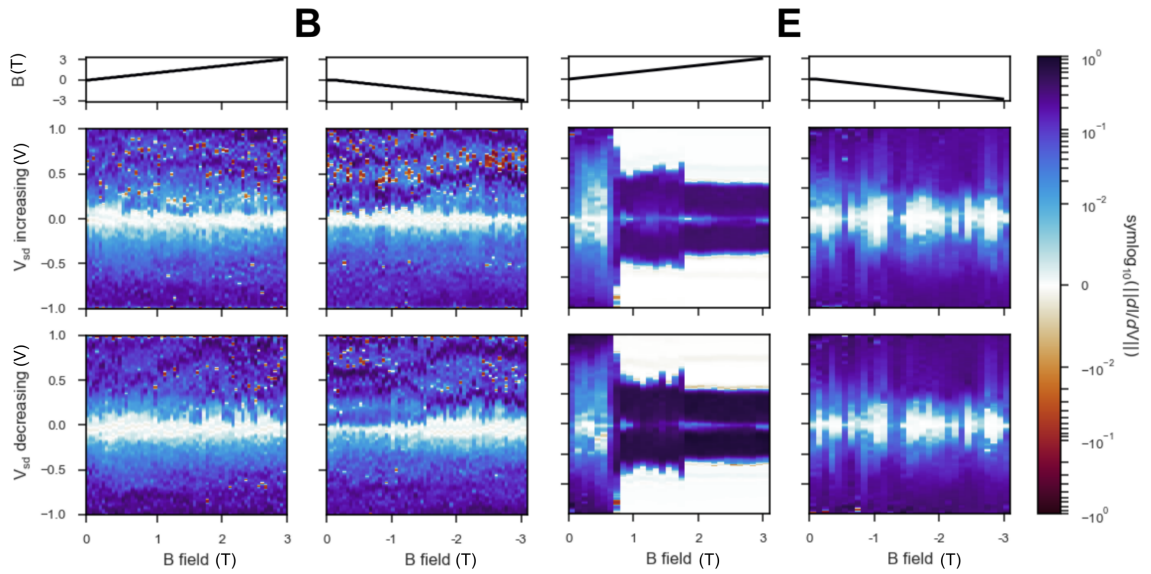


Figure 5.15: Normalised differential conductance as a function of an in-plane magnetic field for devices **B** and **E**. The magnitude and sign of the applied field is shown at the top of the plots. Both devices are plotted on the same symlog scale.

Measuring magnetic phenomena such as spin polarisation and the spin Hall-effect requires advanced geometries where at least two components within the device have large spin-orbit coupling (such as ferro and ferrimagnets) in order to create and detect any changes in spin polarisation (204, 346, 347). Such effects are therefore not realisable in our present device geometry. Magnetoresistance has been observed in tunnel junctions which contain multiple magnetic nanoparticles or a sample with more than one magnetic domain as the misalignment of their magnetic moments, which can be tuned with the application of a magnetic field, acts as a spin filter which modulates the total current (343, 348–350). However, defects such as impurities, off-stoichiometry and surface states can significantly reduce the degree of spin polarisation, and nanocrystals are particularly vulnerable to surface defects given their large surface to volume ratios making it difficult to determine the origin of observed effects (342, 345, 350, 351). While we might not expect to directly observe any spin phenomena within our devices, monitoring the effect of a magnetic field on the transport may provide some clues about the transport mechanisms involved and the quality of our MNCs.

Figure 5.15 shows normalised numerical derivatives of the current measured through devices **B** and **E** under the influence of a magnetic field. In these experiments the field, which was applied in the plane of the graphene but perpendicular to the current flow, was incremented from 0 T to 3 T and IVs were measured at

each increment. The magnet was then swept back to zero and the procedure was repeated between 0 T and -3 T. We can see for device **B** that the positions of the conductance peaks are sensitive to both the direction of the bias and the direction of the magnetic field. We can see some peaks shifting to higher energies as the field increases in magnitude, while for negative magnetic fields and reverse biases there appears to be a crossing of states. For device **E** however, no obvious dependence is apparent. Instead, the transport through this device is dominated by a switch to a state of much greater conductivity at positive magnetic fields, and switching between the these states at negative fields. We do not believe this transition is explicitly caused by the magnetic field as a similar transition was observed in the stability diagram for this device as seen in Figure 5.13. Given that only device **B** displayed any field dependence, it is difficult to comment on the universality of the observation. We note that **B** showed little dependence on an electrostatic field and no signification shifting of conductance peaks. However, in Figure 5.11 we see that, at positive biases, the device exhibits 2 discrete conductivity states, which may relate to the shifting of the conductance peaks under a magnetic field.

Figure 5.16 shows the numerical derivative of the current measured through devices **H** and **J** under the influence of a magnetic field applied in the plane of the graphene electrodes and parallel to the direction of the current. Here, we first swept the magnetic field up to 3 T, down to -3 T and back to zero in small increments to capture any changes which occur when magnetic field changed direction. Under this measurement scheme, neither device shows any significant dependence on the magnetic field as might be expected. We also measured the field dependence over a smaller range (±0.5 T) using smaller field increments but observed much the same behaviour. Unfortunately, it was not possible within the experiment to probe the dependence of a magnetic field perpendicular to the plane of the device, which would have provided more information on the nature of the conductance peaks (85). In these measurements, while we don't observe any field dependence, we do observe additional conductance peaks within the gap region of previous measurements where they were masked by the noise floor of the current amplifier. We will discuss the interpretation of these peaks in a later section.

Finally, the geometry of our devices allowed us to also explore the dual impact of a magnetic field and an electrostatic gate applied in tandem. Figure 5.17 shows stability diagrams for devices **B** and **E** measured at 3, 0 and -3 T. For device **B**, we must first note that the conductance has decreased significantly from that seen in Figure 5.13, which suggests the device has changed in some fashion. Most strikingly, all three stability diagrams look almost identical. This could perhaps be expected at 3 and -3 T from the magnetic field dependence where, in Figure 5.15, the device exhibits two conductance peaks in similar, though not identical, positions when the field reaches its maximum. However, we would expect this to deviate from the behaviour at zero field given the previously observed evolution of peak positions. These three stability diagrams now display some characteristic features of Coulomb blockade, with parallel, equally spaced conductance maxima that shift linearly with gate voltage. This may suggest that the coupling between the graphene and the magnetite has weakened to the point that a single-electron tunnelling conductance channel dominates the transport.

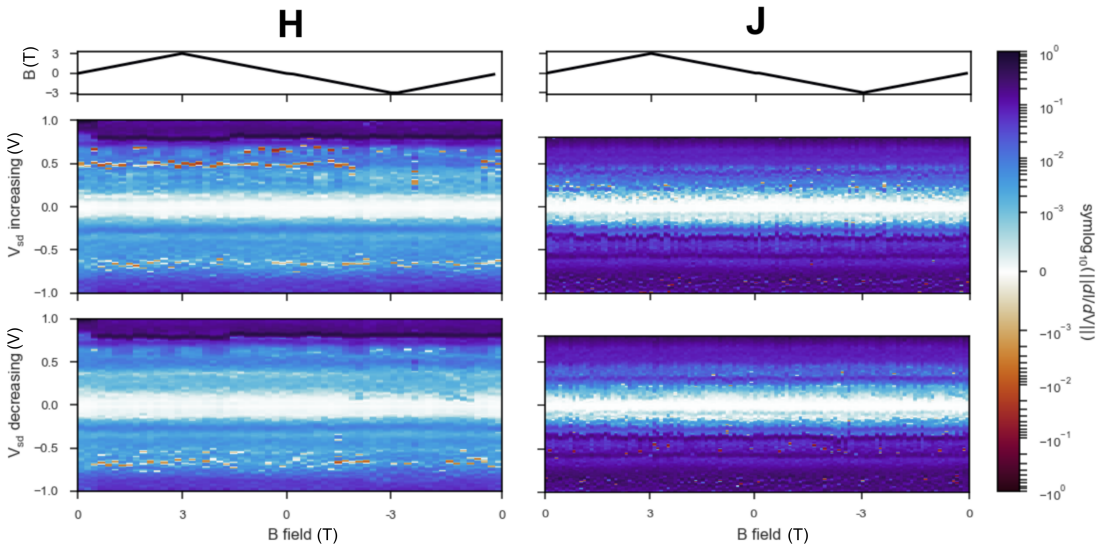


Figure 5.16: Normalised differential conductance as a function of an in-plane magnetic field for devices **H** and **J**. The magnitude and sign of the magnetic field is shown in the top plots. Both devices are plotted on the same symlog scale.

However, the absence of closed diamonds and remaining bandgap at zero bias indicates that the magnetite is still part of the conduction pathway. For device **E** the picture is less clear as the device appears to switch between a lower and higher conductivity state. At both 3 T and -3 T the transport shows significant negative differential resistance (NDR) at positive biases in the high conductivity state, which is not seen at 0 T. Referring back to the SEM image in Figure 5.10, we see that for **E** the device is formed of two MNCs in series. The oscillation between conductivity states and the observed NDR may then be due to the relative magnetic alignment of these two MNCs. Indeed, this description may help explain the observed switching between high and low conductivity. We can see that even in the low conductivity state the device is not very stable and the conductivity maxima and bandgap width can shift markedly. This could be consistent with tunnelling between two anisotropic superparamagnetic particles and, while we would expect the blocking temperature of the 25 nm diameter MNCs to be significantly larger than T_V (342), this thermal barrier may be overcome by Joule heating in a similar manner to the resistive switching observed by Lee *et al.* (321). It is also worth noting the clear signature of Coulomb blockaded transport at -3 T. Clearly there are several phenomena at work within this device and disentangling them further would be very challenging.

Having monitored the transport behaviour at low temperature and witnessed no appreciable dependence of the transport on an in-plane magnetic field or applied gate voltage, I moved on to studying the temperature dependence of the transport.

5.3.5 Temperature Dependence

Finally, I studied how the transport behaviour was influenced by temperature. A key feature I was looking to observe was the Verwey transition at around 100 K as has been reported by other authors for MNCs. The tem-

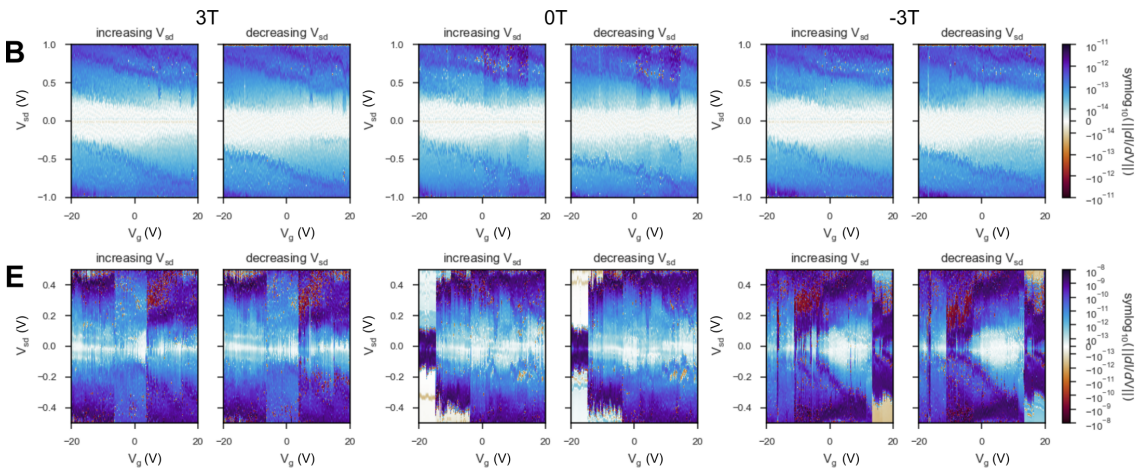


Figure 5.17: Conductance stability diagrams for devices **B** and **E** taken at 3 T (left), 0 T (centre) and -3 T (right). All stability diagrams for each device are plotted on the same symlog scale.

perature dependence of the conductivity will also give us clues about the transport mechanism and whether there exists an activation barrier. IV curves were measured for devices **H**, **L**, **M** and **N** while temperatures were ramped up to 200 K and back down to 3 K. Due to limitations of our measurement system, temperatures above 100 K could only be accessed for relatively short times which limited the amount of data which could be collected. The IV curves allowed us to monitor how features shifted with temperature, and also extract how the zero-bias conductance, $G = \Delta I/\Delta V$, evolved. Figure 5.18 shows how the zero-bias conductances of devices **L**, **M** and **N** varied with temperature, composed from two separate experimental runs.

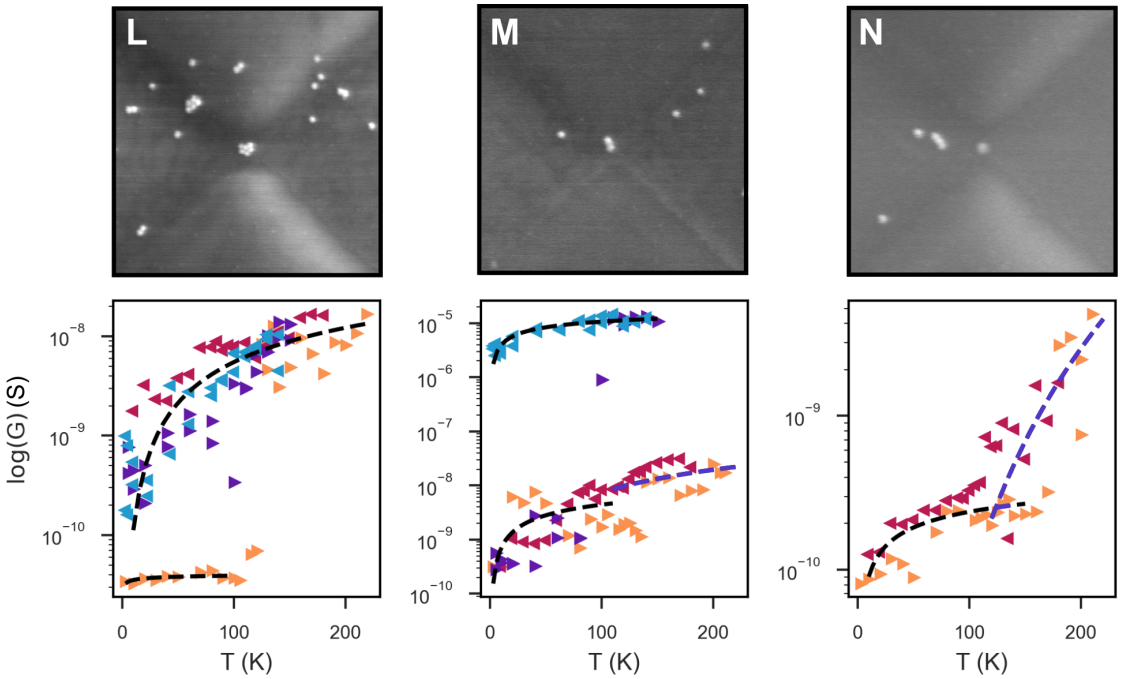


Figure 5.18: SEM images and the logarithm of the zero-bias conductance, extracted from linear fits to IV traces at ±0.05 V, as a function of temperature plotted for devices **L**, **M** and **N**. The coloured data points represent different thermal cycles with the directions of the triangles indicating the direction of the temperature change. The black dashed lines show fits to Eq. (5.1) and the purple dashed lines show fits to Eq. (5.2).

It is immediately apparent that device **L** underwent a Verwey-like transition at around $T_V \approx 110$ K while the temperature was increasing, with the conductance increasing by two orders of magnitude in line with what is observed for bulk magnetite. The device does not, however, transition back to a high resistance state once cooled back down to 3 K. Device **M** did not show a clear transition within the first experiment, despite its conductance also increasing by two orders of magnitude over the whole temperature range, but did then show a three order-of-magnitude transition upon a second temperature cycle. Again, like **L**, once it had transitioned it did not transition back even when cooled to 3 K. **N** did not show a discontinuous transition in the form of sudden a conductance increase, but instead displayed a significant change in gradient around T_V.

Unfortunately, device **N** became non-conductive after the first experimental run before further measurements could be carried out, or the switching behaviour shown previously in Figure 5.12 could be explored further. With the temperature dependent data at hand, I attempted to characterise the transport by fitting the conductance data to a thermally activated polaron hopping model of the general form (352):

$$\sigma = \sigma_0 e^{-(T_0/T)^n} \tag{5.1}$$

The value of the exponent n describes the particular hopping mechanism, where $n = 1$ indicates nearest neighbour hopping (NNH), $n = 0.25$ denotes Mott's variable range hopping (VRH), in which the density of states $\mathcal{N}(E_F)$ is assumed to be uniform (306) or $n = 0.5$ for Efros and Shklovskii's model where Coulomb interactions are explicitly considered, resulting in a parabolic energy dependence of $\mathcal{N}(E_F)$ (353). In these models, transport occurs via phonon mitigated carrier tunnelling from occupied to unoccupied localised states. At lower temperatures, VRH becomes dominant as carriers prefer to tunnel between states close in energy even if they are further away than to tunnel to nearby states at substantially different energies. A related small polaron hopping (SPH) model describes the conductivity as:

$$\sigma = \frac{\sigma_{\mathrm{SPH}}}{T} e^{-(E_a/k_B T)} \tag{5.2}$$

Where E_a is the activation energy for hopping. I fitted sections of the temperature dependent data to all four models. I split data for devices **M** and **N** into high and low temperature regimes, and high and low conductivity regimes which exhibited different temperature dependence on either side of the Verwey temperature, in line with the descriptions given by Ihle and Lorenz (305) and Mott (354). I found that the Mott model best described the low temperature data, whether in the high conductivity or low conductivity states, as the other models predicted a much too aggressive drop in conductivity. For the high temperature low conductivity sections of the data for **M** and **N**, the SPH model was chosen based on prior observations of the transport behaviour above the Verwey temperature (305, 355). Interestingly though, for device **L** the high conductivity state the transport is well described by Mott's VRH across the whole temperature range. Whether the low conductivity state would exhibit SPH above T_V is unknown. These fittings allow us to extract

Device	T_{Mott}^{LC} (K)	E_h^{LC} (meV)	R_h^{LC} (nm)	T_{Mott}^{HC} (K)	E_h^{HC} (meV)	R_h^{HC} (nm)	E_a (meV)
L	0.16	0.03	0.11	52000	0.7	2.6	n/a
M	380	0.22	0.75	270	0.2	0.69	280
N	240	0.19	0.67	n/a	n/a	n/a	90

Table 5.2: Fitting parameters from the Mott model and the SPH model at for low and high conductivity states (LC and HC, respectively) of devices **L**, **M** and **N**.

some characteristic parameters for the transport.

Within the Mott model ($\sigma_0 = \sigma_M$ and $T_0 = T_M$), the characteristic temperature T_M depends on the density of states at the Fermi level $\mathcal{N}(E_F)$ (which is considered to be uniform about the Fermi level) and the electron localisation length ζ such that $T_M = 18/k_B\mathcal{N}(E_F)\zeta^3$. Furthermore, from this we can estimate the mean hopping energy E_h and hopping distance R_h at a given temperature as (356):

$$E_h(T) = \frac{1}{4}k_B\left(T^3T_M\right)^{1/4} \tag{5.3}$$

$$R_h(T) = \frac{3}{8}\zeta\left(\frac{T_M}{T}\right)^{1/4} \tag{5.4}$$

From our fits, and taking $\zeta \approx 0.6$ nm, the approximate size of a single trimeron (299), we can calculate $\mathcal{N}(E_F)$, E_h, R_h for both the low conductivity and high conductivity regimes and estimate E_a for the low conductivity SPH region of **M** and **N** above T_V.

From these values we see that **M** and **N** have similar Mott hopping energies E_h in both high and low conductivity states at 3 K, and the mean hopping distances R_h at 3 K increase to values close to the coherence length ζ. Looking at device **L**, however, we see that these figures are quite different. In the initial low conductivity state the hopping energy is very small, and the average hopping distance is smaller than the average separation between iron sites (299). In the high conductivity state however, the value of R_h is close to the expected inter-particle spacing of 2 nm when the nanoparticles are ordered in an array (237). By reviewing the SEM images in Figure 5.18 we see that device **L** is in fact composed of a cluster of 6 MNCs. Together, these observations lends to the conclusion that for device **L** transport occurs through multiple particles. We also see that **M** is composed of a dimer of MNCs while **N** contains a single MNC at the nanogap. We can then be confident that transport through **N** is dominated by a single MNC. This suggests that the discontinuous jump in conductance observed in **L** and **M** are a result of multiple MNCs providing multiple pathways and perhaps aligning their magnetic moments at T_V rather than because of an intrinsic property of the individual MNCs. Our results do not however give a convincing answer to the bandgap of magnetite, with the two values from the SPH model being substantially different, while the Mott model does not directly give us a prediction of the bandgap. However, the high temperature activation energy of 90 meV found for device **N**, which we are confident is a single MNC device, is in agreement with the high temperature bandgaps or activation energies reported by four other studies (315, 323, 324, 327).

5.4 Conclusion

Bringing together the data gathered from multiple devices, we observe a consistent bandgap in the nanocrystals at low temperatures and additional fine structure at low energies that points to additional transport mechanisms which will require further work to identify. The question remains of whether this is an intrinsic bandgap of the MNCs or due to an extrinsic mechanism, but the lack of gate dependence suggests that it is not due to single-electron charging which was dominant for gold nanoparticle devices. We also see evidence of Verwey-like transitions occurring between 100-120 K, however, we find significant device-to-device variability which makes it challenging to draw robust conclusions. One likely source of the observed device-to-device variability is that of the unknown quality and stoichiometry of the MNCs used. Proper characterisation of the MNCs using techniques such as magnetometry and X-ray diffraction would be valuable in determining the stoichiometric composition and prevalence of defects which are known to strongly impact the transport properties of MNCs. Future experiments would need to carefully characterise the MNCs and ideally synthesise them in-house to gain control over their size, shape, stoichiometry and surface chemistry. With high-quality MNCs, further temperature-dependent measurements will be particularly valuable in building a fuller picture of the transport in these nanoparticles and distinguishing different transport mechanisms. Further work to optimise the concentration and the stability of the MNC suspension will likely boost the yield of single-particle devices. This will greatly assist the identification of intrinsic transport behaviour and will boost the efficiency of data collection.

The results in this chapter contribute towards the understanding of charge transport in magnetite at low temperatures, with implications for other highly-correlated materials. This chapter also reflects the limited consensus in the literature around the transport properties of magnetite and demonstrates the challenge of de-convoluting competing phenomena as well as the importance of sample quality, which may go some way towards explaining the variety of reported results. These experiments demonstrate that graphene nanogaps offer an advantageous platform for the study of charge transport in nanomaterials, with exciting future targets including graphene nanoribbons and spin-crossover nanoparticles.

Outlook

In this chapter we have discussed the transport physics of the strongly-correlated material magnetite and explored the electrical transport through magnetite nanocrystals using graphene nanogap devices. Dielectrophoretic capture of the magnetite nanoparticles was very effective, suggesting this technique's applicability to a whole host of nanomaterials suspended in a wide array of solvents. While the unknown quality of the nanocrystals limited our interpretation of the data, the devices discussed here nonetheless demonstrate the viability of studying transport phenomena in nanomaterials using our graphene nanogap devices. As such, this chapter opens the door to many future studies on electrical transport phenomena in tailored nanomaterials with applications in sensing and computing.

Conclusions and outlook

In this thesis I have shown how graphene nanogap electrodes may be used to probe the electrical properties of single molecules and have described their advantages over competing nanogap platforms for the exploration of charge transport through molecules owing to their low electrostatic screening and stability over large temperature ranges. I have presented promising evidence of quantum interference phenomena in anthraquinone based molecular junctions but simultaneously exposed several key challenges towards the creation of robust molecular devices: the importance of molecular design to encourage strong and stable binding to the graphene electrodes while also preventing molecular aggregation; the difficulty of creating large yields of graphene nanogaps with clean transport gaps through electroburning; and the challenge of depositing molecules across the nanogaps in a controllable manner. I found that the yield of suitable nanogaps was not substantially improved by altering the environment under which electroburning was performed and found that introducing hydrogen gas to passivate the graphene edges resulted in degradation of the silicon dioxide substrate. Further work to improve the yield of nanogaps might explore the effect of pressure or take advantage of hydrogen plasma etching techniques. Control over the deposition of target particles across the nanogap was achieved using the technique of dielectrophoresis, and trapping was demonstrated for a range of target particles. Intriguing evidence of molecular trapping was observed but could not be explored fully in the available time. A continuation of the experiments with conjugated oligomers may unveil a way to direct the assembly and significantly boost the yield of single molecule devices. The transport properties of nanogap devices bridged by single gold nanorods, formed using dielectrophoresis, were examined in detail. Their behaviour was found to closely resemble classical single-electron charging theory but to also show deviations from this theory associated with the influence of the graphene electrodes, demonstrating the ability to probe the transport properties of captured nanomaterials and the hybrid nature of these graphene-nanoparticle devices. This was demonstrated further with the study of devices formed from magnetite nanocrystals. These devices exhibited intricate transport behaviour, which while limited by device-to-device variability and the unknown quality of the nanocrystals, showed a consistent bandgap and signs of a temperature-driven phase transition characteristic of the bulk material.

Realising the promises of molecular electronics for highly efficient, chemically tunable nanoscale devices will require continued improvement of the reproducibility of nanogap architectures and the coupling between

target molecules and electrodes. Dielectrophoresis is a promising technique to bolster the integration of molecules into atomically-sharp nanogap devices, and is here demonstrated to be an excellent technique for the study of nanomaterials. The work in this thesis details a route towards the study of devices formed from a wide range of tunable, low-dimensional nanomaterials with exotic transport properties a range of exciting applications.

Acknowledgements

For each of their help and contribution towards the work in this thesis I would like to thank my supervisors and colleagues:

Dr. J.A. Mol
Prof. G.A.D. Briggs
Prof. H.L. Anderson
Dr. B. Limburg
Dr. J.O. Thomas
Dr. J.L. Swett
Dr. X. Bian
Dr. J.P. Fried
Dr. C. Evangeli
Dr. A. Harzheim
Dr. B.P. Nadappuram
Dr. P. Clément

In addition, I would like to thank the Engineering and Physical Sciences Research Council and the Clarendon Fund for funding my research as well as St. Edmund Hall for additional support in kind.

Appendices

I Chip designs

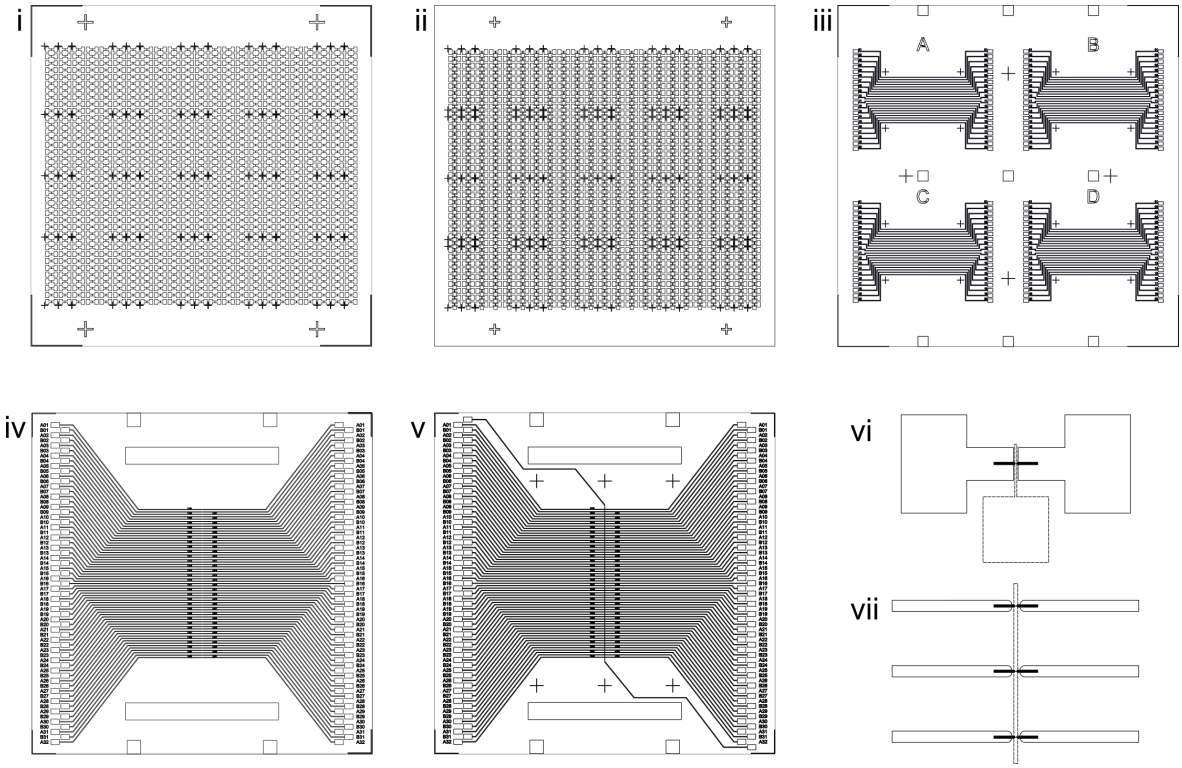


Figure 19: (i) A two-terminal (2T) device layout consisting of 23 × 38 electrode pairs. These chips were used in chapters 1 and 2. (ii) A three-terminal (3T) equivalent layout where each electrode pair has an additional third gate electrode which sits under a 10 nm layer of HfO_2. These chips were also used in chapter 1 and in chapters 3 and 4 for the gold nanoparticle devices. (iii) A remote electrode design for use in dielectrophoresis. The design allows for nanogap site to be separated from the wire-bonds so that solutions could be deposited and washed off with ease. These devices were employed for preliminary experiments in chapter 3 and then were used to make the devices in chapter 5. (iv) A chip-scale remote electrode architecture used primarily in §3.3.1 for optical experiments where spacers needed to be applied to the surface of the chip. The large bars at the top and bottom of the chip are designed to better adhere the graphene to the surface of the chip. (v) A locally-gates remote electrode device. These devices were designed for molecular dielectrophoresis experiments to give the broadest spectroscopic view of and captured molecules. (vi) A closer view of a single 3T (or 2T without the dashed local gate electrode) electrode pair, with a graphene constriction represented in the centre. The separation between the electrodes is 4 μm and the local gate electrode is 1 μm wide. (vii) A closer view of a remote electrode electrode pair, where for the architecture in (iii) the inter-electrode separation is 4 μm and the intra-electrode pair spacing is 60 μm, while for the architecture in (iv) and (v) the inter-electrode separation is 10 μm and the intra-electrode pair spacing is 56 μm. When a local gate is present (dashed), as in (v), this has a width of 4 μm.

II PCBs

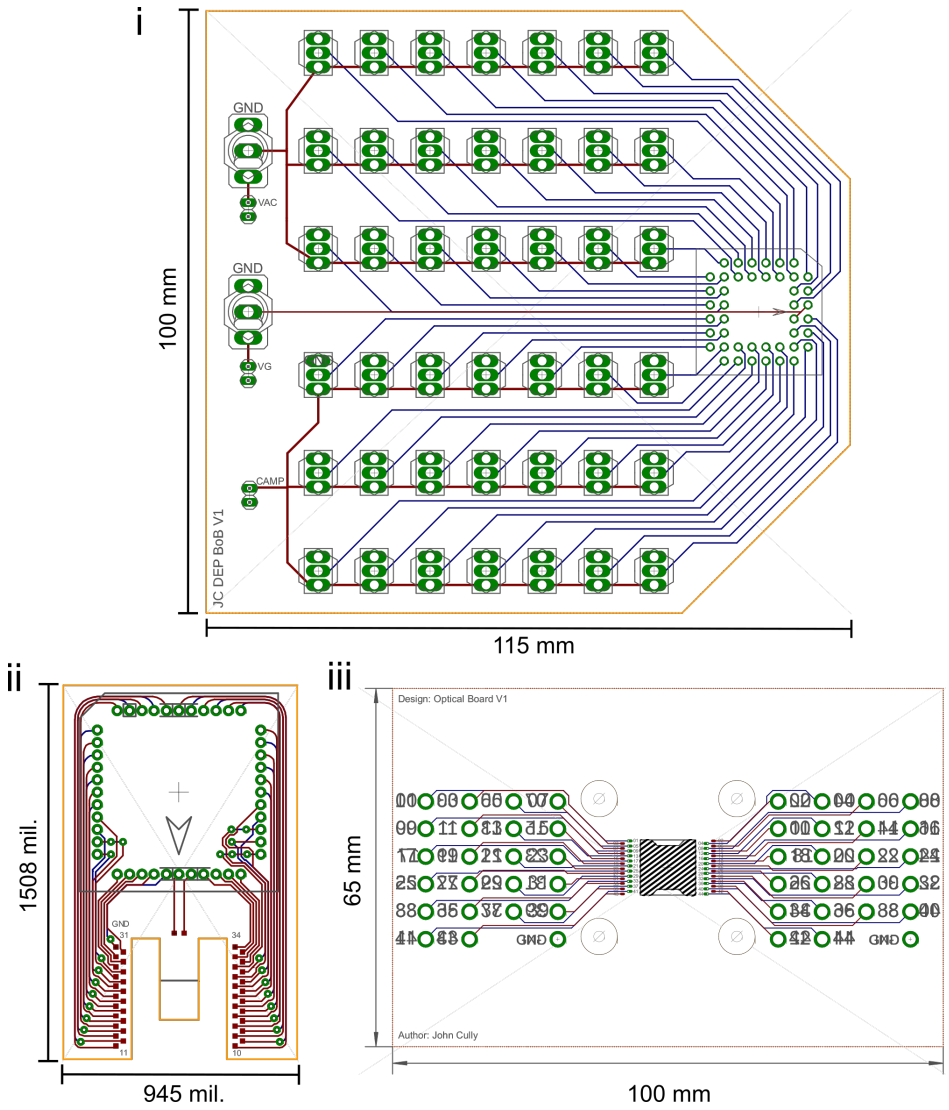


Figure 20: (i) A PCB for a custom break-out-box for dielectrophoresis experiments, where each device on a chip symmetrically wire-bonded to a 44 pin ceramic PLCC chip carrier could be individually connected or disconnected to the trapping voltage or measurement signals or grounded via an SPDT switch. The PCB was mounted in a metal enclosure with BNC outputs for source, drain and gate channels. The chips interfaced with the board through a Winslow Through Board PLCC Wire Wrap Socket (WPLCC-044-T3RC) which was mounted on the outside of the enclosure and soldered to the board. (ii) A small PCB onto which chips could be mounted for dielectrophoresis experiments when non-volatile solvents were being used or the chips required washing, for which the PLCC carriers were not suitable. These PCBs were small enough to fit into our dipstick setups so that devices did not need to be re-wirebonded after dielectrophoresis. These PCBs had a Winslow 1.27mm Pitch 44 Way PLCC Socket (W9303) mounted on the rear side, which could interface with the socket in (i) and the socket in the dipsticks (Winslow Straight Through Hole Mount 1.27 mm, 2.54 mm Pitch IC Socket Adapter, 44 Pin Female PLCC to 44 Pin Male DIP board). (iii) A PCB designed for optical microscopy experiments to fit into the microscope XY stage. The central area was removed to allow the backlight to get to the chip. Each hole was loaded with a HARWIN, H3161 PCB socket which could be interfaces with 1 mm banana plugs. A whole remote-electrode chip would be mounted in the centre and bonded to the pads. These PCBs were all finished with a 1 μm coating of gold to ensure good bonding and low resistance at the bonding pads.

III Orthodox model

The python script used to model orthodox Coulomb blockade is reproduced below. Data was fitted to the model using the `lmfit` package for python (357).

```
    import numpy as np
    def orthodoxCB(Vsds, Vg, CS, CD, CG, RS, RD, q0):

    kb = 8.617e-5  ## [eV]
t = 2.9  ## [K]

    ## With Vsds as a 1D array; Vg as a single float or 1D array;
    ## RS, RD as floats; and CS, CD, CG and q0 as floats factorised by the electron charge, e

    ########################################################
    ##                                                    ##
    ##               =ESp>         =EDm>                ##
    ##        V_S -----||----[.]----||----- V_D          ##
    ##               <ESm=    |    <EDp=                ##
    ##                        =                           ##
    ##                        |                           ##
    ##                       V_G                          ##
    ##                                                    ##
    ########################################################

    ## define range of charge states to be summed over (~= infinity)

    ns = np.arange(-20,21, 1)

    ## expand arrays of Vsds and ns in 2D arrays of shape (len(Vsds) x len(ns))

    vsds = np.repeat(Vsds[:, np.newaxis], len(ns), axis=1)
    nss = np.repeat(ns[np.newaxis, :], len(Vsds), axis=0)

    ## calculate energies for all vsds and nss

    ESp = 1 / (CS + CD + CG) * (e / 2 + (-((CD+CG)*vsds) - (CG*Vg) + ((e*nss)-q0)))
    ESm = 1 / (CS + CD + CG) * (e / 2 - (-((CD+CG)*vsds) - (CG*Vg) + ((e*nss)-q0)))
    EDp = 1 / (CS + CD + CG) * (e / 2 + ((CS*vsds) - (CG*Vg) + ((e*nss)-q0)))
    EDm = 1 / (CS + CD + CG) * (e / 2 - ((CS*vsds) - (CG*Vg) + ((e*nss)-q0)))

    ## create arrays for Gamma values

    GSp = np.zeros(np.shape(vsds))
    GDp = np.zeros(np.shape(vsds))
    GSm = np.zeros(np.shape(vsds))
    GDm = np.zeros(np.shape(vsds))

    ## for each energy value calculate Gamma, where i indexes for each voltage (axis=1), and index j for each n (axis=0)

    for i in range(len(GSp)):
        for j in range(len(GSp[i])):
            try:
                GSp[i][j] = (1 / (RS * e)) * (-ESp[i][j] / (1 - np.exp(ESp[i][j] / (kb * t))))
            except RuntimeWarning:
                GSp[i][j] = 0

    for i in range(len(EDp)):
        for j in range(len(EDp[i])):
            try:
                GDp[i][j] = (1 / (RD * e)) * (-EDp[i][j] / (1 - np.exp(EDp[i][j] / (kb * t))))
            except RuntimeWarning:
                GDp[i][j] = 0

    for i in range(len(ESm)):
        for j in range(len(ESm[i])):
            try:
                GSm[i][j] = (1 / (RS * e)) * (- ESm[i][j] / (1 - np.exp(ESm[i][j] / (kb * t))))
            except RuntimeWarning:
                GSm[i][j] = 0

    for i in range(len(EDm)):
        for j in range(len(EDm[i])):
            try:
                GDm[i][j] = (1 / (RD * e)) * (- EDm[i][j] / (1 - np.exp(EDm[i][j] / (kb * t))))
            except RuntimeWarning:
                GDm[i][j] = 0

    ## calculate sigmas values, starting at n=0 for every voltage v, which is also counted from zero

    sigmas = np.zeros(np.shape(nss))
    sorted_indices_v = np.argsort(np.abs(vsds[:,0]), axis=0)
    for i in sorted_indices_v:
        sorted_indices_n = np.argsort(np.abs(nss[i]), axis=0)
        for j in sorted_indices_n:
            if nss[i][j] == 0:
                sigmas[i][j] = 1  # define as 1 for now
            elif nss[i][j] > 0:
                try:
                    sigmas[i][j] = sigmas[i][j - 1] * (GSp[i][j - 1] + GDp[i][j - 1]) / (GSm[i][j] + GDm[i][j])
                except RuntimeWarning:
                    sigmas[i][j] = 0
            elif nss[i][j] < 0:
            try:
                    sigmas[i][j] = sigmas[i][j + 1] * (GSm[i][j + 1] + GDm[i][j + 1]) / (GSp[i][j] + GDp[i][j])
                except RuntimeWarning:
                    sigmas[i][j] = 0

    ## normalise

    sigma_sum = np.sum(sigmas[i])
    sigmas[i] *= 1 / sigma_sum

    ## calculate current
    i = sigmas * (GDm - GDp)
    I = i.sum(axis=1)
    return (I)
```

Bibliography

1. J. J. Cully, J. L. Swett, K. Willick, J. Baugh, J. A. Mol, *Nanoscale* **13**, 6513–6520 (2021).
2. T. Tamaki, T. Ogawa, *Top. Curr. Chem.* **375**, 79 (2017).
3. P. Gehring, J. M. Thijssen, H. S. J. van der Zant, *Nat. Rev. Phys.* **1**, 381–396 (2019).
4. M. Ratner, *Nat. Nanotechnol.* **8**, 378–381 (2013).
5. B. Mann, H. Kuhn, *J. Appl. Phys.* **42**, 4398–4405 (1971).
6. C. Grave, E. Tran, P. Samorì, G. M. Whitesides, M. A. Rampi, *Synth. Met.* **147**, 11–18 (2004).
7. P. Li, W. Xue, *Nanoscale Res. Lett.* **5**, 1072–1078 (2010).
8. A. Cui, H. Dong, W. Hu, *Small* **11**, 6115–6141 (2015).
9. M. L. Perrin, E. Burzurí, H. S. J. van der Zant, *Chem. Soc. Rev.* **44**, 902–919 (2015).
10. E. Delamarche, B. Michel, H. a. Biebuyck, C. Gerber, *Adv. Mater.* **8**, 719–729 (1996).
11. L. Venkataraman *et al.*, *Nano Lett.* **6**, 458–462 (2006).
12. F. Chen, J. Hihath, Z. Z. Huang, X. X. Li, N. J. Tao, *Annu. Rev. Phys. Chem.* **58**, 535–64 (2007).
13. L. A. Bumm *et al.*, *Science* **271**, 1705–1707 (1996).
14. A. Dhirani, P.-H. Lin, P. Guyot-Sionnest, R. W. Zehner, L. R. Sita, *J. Chem. Phys.* **106**, 5249–5253 (1997).
15. S. Hong *et al.*, *Superlattices Microstruct.* **28**, 289–303 (2000).
16. S. Datta *et al.*, *Phys. Rev. Lett.* **79**, 2530–2533 (1997).
17. M. Dorogi, J. Gomez, R. Osifchin, R. P. Andres, R. Reifenberger, *Phys. Rev. B* **52**, 9071–9077 (1995).
18. R. P. Andres *et al.*, *Science* **272**, 1323–1325 (1996).
19. X. D. Cui *et al.*, *Science* **294**, 571–574 (2001).
20. D. J. Wold, C. D. Frisbie, *J. Am. Chem. Soc.* **122**, 2970–2971 (2000).
21. R. J. Nichols, D. I. Gittins, D. Bethell, D. J. Schiffrin, *Nature* **408**, 67–69 (2000).
22. A. Nitzan, *Science* **300**, 1384–1389 (2003).
23. J. C. Cuevas, E. Scheer, *Molecular Electronics: An Introduction to Theory and Experiment* (WORLD SCIENTIFIC, Singapore, 2010), vol. 1.
24. B. Xu, N. J. Tao, *Science* **301**, 1221 (2003).
25. H. Ohnishi, Y. Kondo, K. Takayanagi, *Nature* **395**, 780–783 (1998).
26. V. Rodrigues, T. Fuhrer, D. Ugarte, *Phys. Rev. Lett.* **85**, 4124–4127 (2000).
27. F. Pump *et al.*, *Appl. Phys. A* **93**, 335–343 (2008).
28. R. Temirov, A. Lassise, F. B. Anders, F. S. Tautz, *Nanotechnology* **19** (2008).
29. X. Xiao, B. Xu, N. J. Tao, *Nano Lett.* **4**, 267–271 (2004).
30. N. J. Tao, *Nat. Nanotechnol.* **1**, 173–181 (2006).
31. R. J. Nichols, S. J. Higgins, *Acc. Chem. Res.* **49**, 2640–2648 (2016).
32. H. Park, A. K. L. Lim, A. P. Alivisatos, J. Park, P. L. McEuen, *Appl. Phys. Lett.* **75**, 301–303 (1999).
33. M. F. Lambert, M. F. Goffman, J. P. Bourgoin, P. Hesto, *Nanotechnology* **14**, 772–777 (2003).
34. M. L. Trouwborst, S. J. Van Der Molen, B. J. Van Wees, *J. Appl. Phys.* **99**, 114316 (2006).
35. D. E. Johnston, D. R. Strachan, A. T. C. Johnson, *Nano Lett.* **7**, 2774–2777 (2007).
36. A. A. Houck, J. Labaziewicz, E. K. Chan, J. A. Folk, I. L. Chuang, *Nano Lett.* **5**, 1685–1688 (2005).
37. Z. M. Wu *et al.*, *Appl. Phys. Lett.* **91**, 2005–2008 (2007).
38. H. Park *et al.*, *Nature* **407**, 57–60 (2000).
39. J. Park *et al.*, *Nature* **417**, 722–725 (2002).
40. W. Liang, M. P. Shores, M. Bockrath, J. R. Long, H. Park, *Nature* **417**, 725–729 (2002).
41. A. De Picciotto *et al.*, *Nanotechnology* **16**, 3110–3114 (2005).
42. H. S. J. van der Zant *et al.*, *Faraday Discuss.* **131**, 347–356 (2006).
43. D. R. Strachan *et al.*, *Appl. Phys. Lett.* **86**, 043109 (2005).
44. T. Böhler, A. Edtbauer, E. Scheer, *Phys. Rev. B - Condens. Matter Mater. Phys.* **76**, 125432 (2007).
45. O. Salata, *Curr. Nanosci.* **1**, 25–33 (2005).
46. K. O'Neill, E. A. Osorio, H. S. Van Der Zant, *Appl. Phys. Lett.* **90** (2007).
47. R. Hoffmann-Vogel, *Appl. Phys. Rev.* **4**, 031302 (2017).
48. J. Moreland, J. W. Ekin, *J. Appl. Phys.* **58**, 3888–3895 (1985).
49. C. Muller, J. van Ruitenbeek, L. de Jongh, *Phys. C Supercond.* **191**, 485–504 (1992).
50. J. M. van Ruitenbeek *et al.*, *Rev. Sci. Instrum.* **67**, 108–111 (1996).
51. M. A. Reed, C. Zhou, C. J. Muller, T. P. Burgin, J. M. Tour, *Science* **278**, 252–254 (1997).

52. M. Teresa González *et al.*, *Nano Lett.* **6**, 2238–2242 (2006).
53. R. Waitz, O. Schecker, E. Scheer, *Rev. Sci. Instrum.* **79**, 093901 (2008).
54. C. A. Martin, R. H. M. Smit, H. S. J. van der Zant, J. M. van Ruitenbeek, *Nano Lett.* **9**, 2940–2945 (2009).
55. A. R. Champagne, A. N. Pasupathy, D. C. Ralph, *Nano Lett.* **5**, 305–308 (2005).
56. C. A. Martin, J. M. Van Ruitenbeek, H. S. J. Van Der Zant, *Nanotechnology* **21** (2010).
57. S. Ballmann, H. B. Weber, *New J. Phys.* **14**, 123028 (2012).
58. S. Ghasemi, K. Moth-Poulsen, *Nanoscale* **13**, 659–671 (2021).
59. A. Bellunato, H. Arjmandi Tash, Y. Cesa, G. F. Schneider, *ChemPhysChem* **17**, 785–801 (2016).
60. P. Qi *et al.*, *J. Am. Chem. Soc.* **126**, 11774–11775 (2004).
61. P. G. Collins, M. Hersam, M. Arnold, R. Martel, P. Avouris, *Phys. Rev. Lett.* **86**, 3128–3131 (2001).
62. D. Wei *et al.*, *Nano Lett.* **8**, 1625–1630 (2008).
63. X. Guo *et al.*, *Science* **311**, 356–9 (2006).
64. C. Thiele *et al.*, *Appl. Phys. Lett.* **104**, 103102 (2014).
65. Z. R. Abrams, Z. Ioffe, A. Tsukernik, O. Cheshnovsky, Y. Hanein, *Nano Lett.* **7**, 2666–2671 (2007).
66. R. Krupke, F. Hennrich, H. Lohneysen, M. M. Kappes, *Science* **301**, 344–347 (2003).
67. R. Krupke, F. Hennrich, H. B. Weber, M. M. Kappes, H. V. Löhneysen, *Nano Lett.* **3**, 1019–1023 (2003).
68. J. Zhu *et al.*, PhD thesis, 2016, pp. 2905–2908.
69. A. H. Castro Neto, F. Guinea, N. M. R. Peres, K. S. Novoselov, A. K. Geim, *Rev. Mod. Phys.* **81**, 109–162 (2009).
70. C. Mattevi, H. Kim, M. Chhowalla, *J. Mater. Chem.* **21**, 3324–3334 (2011).
71. X. Liang *et al.*, *ACS Nano* **5**, 9144–9153 (2011).
72. J. Kang, D. Shin, S. Bae, B. H. Hong, *Nanoscale* **4**, 5527 (2012).
73. C. S. Lau, J. A. Mol, J. H. Warner, G. A. D. Briggs, *Phys. Chem. Chem. Phys.* **16**, 20398–20401 (2014).
74. J. A. Mol *et al.*, *Nanoscale* **7**, 13181–13185 (2015).
75. J. Moser, A. Bachtold, *Appl. Phys. Lett.* **95**, 2007–2010 (2009).
76. F. Prins *et al.*, *Nano Lett.* **11**, 4607–4611 (2011).
77. C. Jin, H. Lan, L. Peng, K. Suenaga, S. Iijima, *Phys. Rev. Lett.* **102**, 205501 (2009).
78. A. Barreiro, F. Börrnert, M. H. Rümmeli, B. Büchner, L. M. K. Vandersypen, *Nano Lett.* **12**, 1873–1878 (2012).
79. S. G. Sarwat *et al.*, *Nano Lett.* **17**, 3688–3693 (2017).
80. M. El Abbassi *et al.*, *Nanoscale* **9**, 17312–17317 (2017).
81. Y. Cao *et al.*, *Angew. Chemie - Int. Ed.* **51**, 12228–12232 (2012).
82. C. Gu, D. Su, C. Jia, S. Ren, X. Guo, *RSC Adv.* **8**, 6814–6819 (2018).
83. A. Bellunato *et al.*, *Nano Lett.* **18**, 2505–2510 (2018).
84. S. Caneva *et al.*, *Nat. Nanotechnol.* **13**, 1126–1131 (2018).
85. P. Gehring *et al.*, *ACS Nano* **11**, 5325–5331 (2017).
86. J. O. Island *et al.*, *J. Phys. Condens. Matter* **26**, 474205 (2014).
87. J. C. Cuevas *et al.*, *Nanotechnology* **14**, R29–R38 (2003).
88. S. Datta, *Quantum Transport: Atom to Transistor* (Cambridge University Press, Cambridge, 2005).
89. J. G. Simmons, *J. Appl. Phys.* **34**, 1793–1803 (1963).
90. S. Datta, *Electronic Transport in Mesoscopic Systems* (Cambridge University Press, 1995), p. 393.
91. C. J. Lambert, *Chem. Soc. Rev.* **44**, 875–888 (2015).
92. B. Limburg *et al.*, *Adv. Funct. Mater.* **28**, 1803629 (2018).
93. U. Fano, *Phys. Rev.* **124**, 1866–1878 (1961).
94. P. Gehring *et al.*, *Nano Lett.* **16**, 4210–4216 (2016).
95. C. M. Finch, V. M. García-Suárez, C. J. Lambert, *Phys. Rev. B* **79**, 033405 (2009).
96. T. A. Papadopoulos, I. M. Grace, C. J. Lambert, *Phys. Rev. B* **74**, 193306 (2006).
97. A. Grigoriev, J. Sköldberg, G. Wendin, Ž. Crljen, *Phys. Rev. B - Condens. Matter Mater. Phys.* **74**, 045401 (2006).
98. E. H. Van Dijk, D. J. Myles, M. H. Van Der Veen, J. C. Hummelen, *Org. Lett.* **8**, 2333–2336 (2006).
99. C. M. Guédon *et al.*, *Nat. Nanotechnol.* **7**, 305–309 (2012).
100. M. Koole, J. M. Thijssen, H. Valkenier, J. C. Hummelen, H. S. J. van der Zant, *Nano Lett.* **15**, 5569–5573 (2015).
101. T. Markussen, J. Schiötz, K. S. Thygesen, *J. Chem. Phys.* **132** (2010).
102. A. K. Ismael, I. Grace, C. J. Lambert, *Phys. Chem. Chem. Phys.* **19**, 6416–6421 (2017).
103. M. Mayor *et al.*, *Angew. Chemie - Int. Ed.* **42**, 5834–5838 (2003).
104. W. Hong *et al.*, *Beilstein J. Nanotechnol.* **2**, 699–713 (2011).
105. V. Kaliginedi *et al.*, *J. Am. Chem. Soc.* **134**, 5262–5275 (2012).
106. H. Valkenier *et al.*, *Phys. Chem. Chem. Phys.* **16**, 653–662 (2014).
107. J. Alqahtani, H. Sadeghi, S. Sangtarash, C. J. Lambert, *Angew. Chemie - Int. Ed.* **57**, 15065–15069 (2018).
108. Y. Li *et al.*, *Nat. Mater.* **18**, 357–363 (2019).
109. Allresist GmbH, *E-Beam Resist AR-N 7500 series.*
110. JEOL Ltd., "JBX-5500series Operation Guide", tech. rep.
111. JEOL Ltd., "JBX-5500series Operation (Software)", tech. rep.

112. J. Alqahtani, H. Sadeghi, S. Sangtarash, C. J. Lambert, *Angew. Chemie Int. Ed.*, 15065–15069 (2018).

113. K. G. L. Pedersen *et al.*, *Phys. Rev. B* **90**, 125413 (2014).

114. S. Lumetti, L. Martini, A. Candini, *Semicond. Sci. Technol.* **32**, 024002 (2017).

115. H. Sun *et al.*, *ChemPhysChem* **19**, 2258–2265 (2018).

116. A. Salazar *et al.*, *Microsystems Nanoeng.* **6**, 9 (2020).

117. E. Pop, V. Varshney, A. K. Roy, *MRS Bull.* **37**, 1273–1281 (2012).

118. A. Barreiro, F. Börrnert, M. H. Rümmeli, B. Büchner, L. M. K. Vandersypen, *Nano Lett.* **12**, 1873–1878 (2012).

119. Z. J. Qi *et al.*, *ACS Nano* **9**, 3510–3520 (2015).

120. J. K. Lee *et al.*, *ACS Nano* **13**, 2379–2388 (2019).

121. C. Nef *et al.*, *Nanoscale* **6**, 7249–7254 (2014).

122. J.-i. Lee, S. Jang, S. Cho, E. Kim, *Curr. Appl. Phys.* **16**, 731–737 (2016).

123. J. Güttinger *et al.*, *Phys. Rev. Lett.* **103**, 046810 (2009).

124. C. Stampfer *et al.*, *Phys. Rev. Lett.* **102**, 056403 (2009).

125. F. Molitor *et al.*, *Semicond. Sci. Technol.* **25**, 034002 (2010).

126. J. Güttinger *et al.*, *Reports Prog. Phys.* **75**, 126502 (2012).

127. L. A. Ponomarenko *et al.*, *Science* **320**, 356–358 (2008).

128. P. Gallagher, K. Todd, D. Goldhaber-Gordon, *Phys. Rev. B - Condens. Matter Mater. Phys.* **81**, 115409 (2010).

129. X. Wang *et al.*, *Nat. Nanotechnol.* **6**, 563–567 (2011).

130. D. Bischoff *et al.*, *Appl. Phys. Rev.* **2**, 031301 (2015).

131. A. Barreiro, H. S. J. van der Zant, L. M. K. Vandersypen, *Nano Lett.* **12**, 6096–6100 (2012).

132. C. Evangeli *et al.*, *Carbon N. Y.* **178**, 632–639 (2021).

133. C. Evangeli *et al.*, "Statistical signature of electroburning in graphene nano-junctions", 2021.

134. I. Meric *et al.*, *Nat. Nanotechnol.* **3**, 654–659 (2008).

135. J. Moser, A. Barreiro, A. Bachtold, *Appl. Phys. Lett.* **91**, 163513 (2007).

136. M. Ring *et al.*, *Nano Lett.* **20**, 5773–5778 (2020).

137. H. Sadeghi *et al.*, *Proc. Natl. Acad. Sci. U.S.A.* **112**, 2658–2663 (2015).

138. Y. Gao, D. Xu, T. Cui, D. Li, *Phys. Chem. Chem. Phys.* **23**, 13261–13266 (2021).

139. Y. H. Lu *et al.*, *Appl. Phys. Lett.* **94**, 122111 (2009).

140. H. Jippo, M. Ohfuchi, *J. Appl. Phys.* **113**, 183715 (2013).

141. H. Gonzalez-Herrero *et al.*, *Science* **352**, 437–441 (2016).

142. V. M. García-Suárez *et al.*, *Nanoscale* **10**, 18169–18177 (2018).

143. H. Sadeghi, S. Sangtarash, C. Lambert, *Nano Lett.* **17**, 4611–4618 (2017).

144. J. P. Fried *et al.*, *Nanoscale* **12**, 871–876 (2020).

145. A. Yadav *et al.*, *Chem. Sci.*, 936–942 (2019).

146. F. Schedin *et al.*, *Nat. Mater.* **6**, 652–655 (2007).

147. B. Standley *et al.*, *Nano Lett.* **8**, 3345–3349 (2008).

148. H. Zhang *et al.*, *Nano Lett.* **12**, 1772–1775 (2012).

149. T. Kahn, C. Brandon, *step_detect.py*, 2016.

150. Y. Wimmer, A.-M. El-Sayed, W. Gös, T. Grasser, A. L. Shluger, *Proc. R. Soc. A Math. Phys. Eng. Sci.* **472**, 20160009 (2016).

151. S. A. Sheikholeslam, H. Manzano, C. Grecu, A. Ivanov, *J. Mater. Chem. C* **4**, 8104–8110 (2016).

152. L. Pósa *et al.*, *Nano Lett.* **17**, 6783–6789 (2017).

153. L. Xie, L. Jiao, H. Dai, *J. Am. Chem. Soc.* **132**, 14751–14753 (2010).

154. S. Xie, N. Jiao, S. Tung, L. Liu, *Micromachines* **6**, 1317–1330 (2015).

155. X. Wang, H. Dai, *Nat. Chem.* **2**, 661–665 (2010).

156. Z. Shi *et al.*, *Adv. Mater.* **23**, 3061–3065 (2011).

157. D. Hug *et al.*, *npj 2D Mater. Appl.*, 21 (2017).

158. B. Ma, S. Ren, P. Wang, C. Jia, X. Guo, *Nano Res.* **12**, 137–142 (2019).

159. J. Berthelot *et al.*, *Nat. Nanotechnol.* **9**, 295–299 (2014).

160. D. G. Kotsifaki, V. G. Truong, S. N. Chormaic, *Nano Lett.* **20**, 3388–3395 (2020).

161. D. G. Kotsifaki, S. N. Chormaic, *Nanophotonics* **8**, 1227–1245 (2019).

162. A. Castellanos-Gomez *et al.*, *2D Mater.* **1**, 011002 (2014).

163. S. Decossas, F. Mazen, T. Baron, G. Brémond, A. Souifi, *Nanotechnology* **14**, 1272–1278 (2003).

164. D. Engstrom, B. Porter, M. Pacios, H. Bhaskaran, *J. Mater. Res.* **29**, 1792–1816 (2014).

165. J. Zhu, M. C. Hersam, *Adv. Mater.* **29**, 1603895 (2017).

166. A. Kaliyaraj Selva Kumar, Y. Zhang, D. Li, R. G. Compton, *Electrochem. commun.* **121**, 106867 (2020).

167. M. El Abbassi *et al.*, *Nat. Nanotechnol.* **14**, 957–961 (2019).

168. J. O. Thomas *et al.*, *Chem. Sci.* **12**, 11121–11129 (2021).

169. A. Bezryadin, C. Dekker, G. Schmid, *Appl. Phys. Lett.* **71**, 1273–1275 (1997).

170. I. Amlani, A. M. Rawlett, L. A. Nagahara, R. K. Tsui, *Appl. Phys. Lett.* **80**, 2761–2763 (2002).

171. S. H. Hong *et al.*, *J. Vac. Sci. Technol. B Microelectron. Nanom. Struct.* **24**, 136–138 (2006).

172. R. J. Barsotti *et al.*, *Small* **3**, 488–499 (2007).

173. S. Kumar, S.-H. Yoon, G.-H. Kim, *Curr. Appl. Phys.* **9**, 101–103 (2009).

174. S. Raychaudhuri, S. A. Dayeh, D. Wang, E. T. Yu, *Nano Lett.* **9**, 2260–2266 (2009).

175. D. Cheon, S. Kumar, G.-H. Kim, *Appl. Phys. Lett.* **96**, 013101 (2010).

176. S. I. Khondaker, K. Luo, Z. Yao, *Nanotechnology* **21**, 095204 (2010).

177. C. W. Marquardt *et al.*, *Nat. Nanotechnol.* **5**, 863–867 (2010).

178. M. Manheller, S. Karthäuser, R. Waser, K. Blech, U. Simon, *J. Phys. Chem. C* **116**, 20657–20665 (2012).

179. Y. Vardi, A. Guttman, I. Bar-Joseph, *Nano Lett.* **14**, 2794–2799 (2014).

180. D. Montemurro *et al.*, *Nanotechnology* **26**, 385302 (2015).

181. M. Sam, N. Moghimian, R. B. Bhiladvala, *Nanoscale* **8**, 889–900 (2016).

182. K. Tapio *et al.*, *Nano Lett.* **16**, 6780–6786 (2016).

183. A. Holovchenko *et al.*, *Adv. Mater.* **28**, 7228–7233 (2016).

184. E. Burzurí *et al.*, *Nanoscale* **10**, 7966–7970 (2018).

185. M. Engel *et al.*, *Nat. Commun.* **9**, 4095 (2018).

186. L. Liu, K. Chen, N. Xiang, Z. Ni, *Electrophoresis* **40**, 873–889 (2019).

187. R. Hölzel, N. Calander, Z. Chiragwandi, M. Willander, F. F. Bier, *Phys. Rev. Lett.* **95**, 128102 (2005).

188. A. Barik *et al.*, *Nat. Commun.* **8**, 1867 (2017).

189. E.-M. Laux, C. Wenger, F. F. Bier, R. Hölzel, *Anal. Bioanal. Chem.* **412**, 3859–3870 (2020).

190. L. Soffer, A. Rendos, A. L. Zosuls, B. M. Walsh, K. A. Brown, *Appl. Phys. Lett.* **116**, 084101 (2020).

191. B. P. Nadappuram *et al.*, *Nat. Nanotechnol.* **14**, 80–88 (2019).

192. H. Morgan, N. G. Green, *AC Electrokinetics: Colloids and Nanoparticles* (Research Studies Press, Philadelphia, 2003).

193. R. Pethig, *Biomicrofluidics* **4**, 022811 (2010).

194. B. R. Burg, V. Bianco, J. Schneider, D. Poulikakos, *J. Appl. Phys.* **107**, 124308 (2010).

195. A. Ramos, P. García-Sánchez, H. Morgan, *Curr. Opin. Colloid Interface Sci.* **24**, 79–90 (2016).

196. A. Castellanos, A. Ramos, A. González, N. G. Green, H. Morgan, *J. Phys. D. Appl. Phys.* **36**, 2584–2597 (2003).

197. X. He *et al.*, *ACS Nano* **13**, 14041–14047 (2019).

198. R. Kullock, M. Ochs, P. Grimm, M. Emmerling, B. Hecht, *Nat. Commun.* **11**, 115 (2020).

199. A. Barik, X. Chen, S.-H. Oh, *Nano Lett.* **16**, 6317–6324 (2016).

200. X. Knigge, C. Wenger, F. F. Bier, R. Hölzel, *J. Phys. D. Appl. Phys.* **51**, 065308 (2018).

201. E.-S. Yu *et al.*, *Nat. Commun.* **11**, 2804 (2020).

202. Shuangxi Xie, N. Jiao, Lianqing Liu, S. Tung, presented at the 10th IEEE Int. Conf. Nano/Micro Eng. Mol. Syst. Pp. 314–317.

203. S. Xiao, X. Zhu, B.-H. Li, N. A. Mortensen, *Front. Phys.* **11**, 117801 (2016).

204. W. Han, R. K. Kawakami, M. Gmitra, J. Fabian, *Nat. Nanotechnol.* **9**, 794–807 (2014).

205. D. Rodrigo *et al.*, *Science* **349**, 165–168 (2015).

206. A. Avsar *et al.*, *Rev. Mod. Phys.* **92**, 021003 (2020).

207. B. Lee, T. Moon, T.-G. Kim, D.-K. Choi, B. Park, *Appl. Phys. Lett.* **87**, 012901 (2005).

208. Y. Wu *et al.*, *Appl. Phys. Lett.* **101**, 99–102 (2012).

209. K. Bolotin *et al.*, *Solid State Commun.* **146**, 351–355 (2008).

210. R. Kim, X. Wang, M. Lundstrom, *Notes on Fermi-Dirac Integrals*, 2019.

211. X. Wang, M. Lundstrom, *Fermi-Dirac integral using a table method in MATLAB*, 2019.

212. C. Kittel, *Introduction to Solid State Physics* (Wiley, New York, 7th, 1996), p. 150.

213. K. J. Freedman *et al.*, *Nat. Commun.* **7**, 10217 (2016).

214. B. C. Gierhart, D. G. Howitt, S. J. Chen, R. L. Smith, S. D. Collins, *Langmuir* **23**, 12450–12456 (2007).

215. W. Ahmed, E. S. Kooij, A. van Silfhout, B. Poelsema, *Nano Lett.* **9**, 3786–3794 (2009).

216. L. von Diezmann, Y. Shechtman, W. E. Moerner, *Chem. Rev.* **117**, 7244–7275 (2017).

217. L. Gross, *Nat. Chem.* **3**, 273–278 (2011).

218. E. Leary *et al.*, *J. Am. Chem. Soc.* **140**, 12877–12883 (2018).

219. S. Tuukkanen, PhD thesis, University of Jyväskylä, 2006.

220. A. Kuzyk, B. Yurke, J. J. Toppari, V. Linko, P. Törmä, *Small* **4**, 447–450 (2008).

221. A. Narita, Z. Chen, Q. Chen, K. Müllen, *Chem. Sci.* **10**, 964–975 (2019).

222. T. Chowdhury *et al.*, *Nat. Nanotechnol.* **15**, 29–34 (2020).

223. J. Cui *et al.*, *Nat. Commun.* **10**, 5401 (2019).

224. B. C. Steimle, J. L. Fenton, R. E. Schaak, *Science* **367**, 418–424 (2020).

225. M. S. Gudiksen, K. N. Maher, L. Ouyang, H. Park, *Nano Lett.* **5**, 2257–2261 (2005).

226. S. J. Kress *et al.*, *Nano Lett.* **15**, 6267–6275 (2015).

227. Y. Vardi, E. Cohen-Hoshen, G. Shalem, I. Bar-Joseph, *Nano Lett.* **16**, 748–752 (2016).

228. S. Namgung *et al.*, *ACS Nano* **12**, 2780–2788 (2018).

229. C. U. Hail *et al.*, *Nat. Commun.* **10**, 1880 (2019).

230. H. L. Thi N'Goc *et al.*, *Adv. Mater.* **29**, 1604745 (2017).

231. H. Al-Bustami *et al.*, *Small* **14**, 1801249 (2018).

232. L. Lesser-Rojas *et al.*, *Nano Lett.* **14**, 2242–2250 (2014).

233. C. T. Ertsgaard *et al.*, *Nano Lett.* **18**, 5946–5953 (2018).

234. Y. Li *et al.*, *Nat. Nanotechnol.* **13**, 1167–1173 (2018).

235. X. Xu *et al.*, *Nano Lett.* **18**, 4130–4135 (2018).

236. J. Dugay *et al.*, *Nano Lett.* **17**, 186–193 (2017).

237. G. Song, M. Ranjbar, D. R. Daughton, R. A. Kiehl, *Nano Lett.* **19**, 7112–7118 (2019).

238. H. Wang *et al.*, *Nanoscale* **12**, 8095–8108 (2020).

239. M. Faraday, *Philos. Trans. R. Soc. London* **147**, 145–181 (1857).

240. K. Maeda *et al.*, *ACS Nano* **6**, 2798–2803 (2012).

241. L. Wang, M. Hasanzadeh Kafshgari, M. Meunier, *Adv. Funct. Mater.* **30**, 2005400 (2020).

242. Y. Yan, S. C. Warren, P. Fuller, B. A. Grzybowski, *Nat. Nanotechnol.* **11**, 603–608 (2016).

243. S. Kim *et al.*, *Sci. Adv.* **6**, eabb3348 (2020).

244. P. Singh *et al.*, *Int. J. Mol. Sci.* **19**, 1979 (2018).

245. J. von Delft, D. Ralph, *Phys. Rep.* **345**, 61–173 (2001).

246. Y. Azuma *et al.*, *Appl. Phys. Lett.* **99**, 073109 (2011).

247. S. Kano *et al.*, *J. Appl. Phys.* **114**, 223717 (2013).

248. Y. Azuma, Y. Onuma, M. Sakamoto, T. Teranishi, Y. Majima, *Nanoscale* **8**, 4720–4726 (2016).

249. O. Bitton, D. B. Gutman, R. Berkovits, A. Frydman, *Nat. Commun.* **8**, 402 (2017).

250. A. M. Rawlett *et al.*, *Nanotechnology* **14**, 377–384 (2003).

251. L. Zheng, S. Li, J. P. Brody, P. J. Burke, *Langmuir* **20**, 8612–8619 (2004).

252. M. Kumar, R. Avriller, A. L. Yeyati, J. M. Van Ruitenbeek, *Phys. Rev. Lett.* **108**, 146602 (2012).

253. A. Guttman, D. Mahalu, J. Sperling, E. Cohen-Hoshen, I. Bar-Joseph, *Appl. Phys. Lett.* **99**, 063113 (2011).

254. T. Dadosh *et al.*, *Nature* **436**, 677–680 (2005).

255. J. Eklöf-Österberg, T. Gschneidtner, B. Tebikachew, S. Lara-Avila, K. Moth-Poulsen, *Small* **14**, 1803471 (2018).

256. B. Wang *et al.*, *Phys. Rev. B* **63**, 035403 (2000).

257. K. I. Bolotin, F. Kuemmeth, A. N. Pasupathy, D. C. Ralph, *Appl. Phys. Lett.* **84**, 3154–3156 (2004).

258. F. Kuemmeth, K. I. Bolotin, S.-f. Shi, D. C. Ralph, *Nano Lett.* **8**, 4506–4512 (2008).

259. S. Kano *et al.*, *ACS Nano* **6**, 9972–9977 (2012).

260. D. V. Averin, A. N. Korotkov, *Zh. Eksp. Teor. Fiz.* **97**, 1661–1673 (1990).

261. I. O. Kulik, I. Shekhter, *Zh. Eksp. Teor. Fiz.* **68**, 623–640 (1975).

262. D. Averin, K. Likharev, in *Mesoscopic Phenom. Solids*, ed. by B. Altshuler, P. Lee, R. Webb (Elsevier, New York, 1991), chap. 6, pp. 173–271.

263. D. V. Averin, A. N. Korotkov, K. K. Likharev, *Phys. Rev. B* **44**, 6199–6211 (1991).

264. C. W. Beenakker, *Phys. Rev. B* **44**, 1646–1656 (1991).

265. H. van Houten, C. W. J. Beenakker, A. A. M. Staring, *Single Charge Tunneling*, ed. by H. Grabert, M. H. Devoret (Springer US, Boston, MA, 1992), vol. 294, pp. 442–445.

266. E. B. Foxman *et al.*, *Phys. Rev. B* **47**, 10020–10023 (1993).

267. L. P. Kouwenhoven *et al.*, in *Mesoscopic Electron Transp.* (Springer Netherlands, Dordrecht, 1997), pp. 105–214.

268. M. Amman, R. Wilkins, E. Ben-Jacob, P. D. Maker, R. C. Jaklevic, *Phys. Rev. B* **43**, 1146–1149 (1991).

269. A. E. Hanna, M. Tinkham, *Phys. Rev. B* **44**, 5919–5922 (1991).

270. M. El Abbassi *et al.*, *Nanoscale* **9**, 17312–17317 (2017).

271. A. García-Miranda Ferrari, D. A. C. Brownson, C. E. Banks, *Sci. Rep.* **9**, 15961 (2019).

272. G. Zhang, M. Walker, P. R. Unwin, *Langmuir* **32**, 7476–7484 (2016).

273. Y.-C. Lin *et al.*, *Nano Lett.* **12**, 414–419 (2012).

274. A. B. Taylor, A. M. Siddiquee, J. W. M. Chon, *ACS Nano* **8**, 12071–12079 (2014).

275. A. V. Danilov, D. S. Golubev, S. E. Kubatkin, *Phys. Rev. B* **65**, 125312 (2002).

276. D. Davidović, M. Tinkham, *Appl. Phys. Lett.* **73**, 3959–3961 (1998).

277. W. P. Halperin, *Rev. Mod. Phys.* **58**, 533–606 (1986).

278. G. V. Kraniotis, G. K. Leontaris, *Closed form solution for the surface area, the capacitance and the demagnetizing factors of the ellipsoid*, 2013.

279. P. Seneor, A. Bernand-Mantel, F. Petroff, *J. Phys. Condens. Matter* **19**, 165222 (2007).

280. Y. Matsuda, W. Q. Deng, W. A. Goddard, *J. Phys. Chem. C* **111**, 11113–11116 (2007).

281. B. Ma *et al.*, *J. Appl. Phys.* **115**, 183708 (2014).

282. T. Cusati *et al.*, *Sci. Rep.* **7**, 5109 (2017).

283. F. Godel *et al.*, *Adv. Mater.* **29**, 1604837 (2017).

284. K. S. Makarenko *et al.*, *Adv. Mater.* **29**, 1702920 (2017).

285. J. Moser, A. Bachtold, *Appl. Phys. Lett.* **95**, 173506 (2009).

286. T. Schmidt *et al.*, *Europhys. Lett.* **36**, 61–66 (1996).

287. C. Stampfer *et al.*, *Appl. Phys. Lett.* **92**, 012102 (2008).

288. J. I. Gonzalez, T.-H. Lee, M. D. Barnes, Y. Antoku, R. M. Dickson, *Phys. Rev. Lett.* **93**, 147402 (2004).

289. B. Du *et al.*, *Laser Photon. Rev.* **11**, 1600148 (2017).

290. M. Weinhold, S. Chatterjee, P. J. Klar, *Commun. Phys.* **2**, 18 (2019).

291. A. A. Mills, *Ann. Sci.* **61**, 273–319 (2004).

292. C. N. R. Rao, *Annu. Rev. Phys. Chem.* **40**, 291–326 (1989).

293. J. Coey, C. Chien, *MRS Bull.* **28**, 720–724 (2003).

294. F. Walz, *J. Phys. Condens. Matter* **14**, R285–R340 (2002).

295. E. J. Verwey, P. W. Haayman, F. C. Romeijn, *J. Chem. Phys.* **15**, 181–187 (1947).

296. E. Verwey, P. Haayman, *Physica* **8**, 979–987 (1941).

297. J. García, G. Subías, *J. Phys. Condens. Matter* **16**, R145–R178 (2004).

298. G. Subías *et al.*, *Phys. Rev. Lett.* **93**, 156408 (2004).

299. M. S. Senn, J. P. Wright, J. P. Attfield, *Nature* **481**, 173–176 (2012).

300. P. Piekarz, K. Parlinski, A. M. Oleś, *Physical Review B* **76** (2007).

301. M. S. Senn, J. P. Wright, J. Cumby, J. P. Attfield, *Phys. Rev. B* **92**, 024104 (2015).

302. S. Borroni *et al.*, *New J. Phys.* **19**, 103013 (2017).

303. G. Perversi *et al.*, *Nat. Commun.* **10**, 2857 (2019).

304. E. Baldini *et al.*, *Nat. Phys.* **16**, 541–545 (2020).

305. D. Ihle, B. Lorenz, *J. Phys. C Solid State Phys.* **19**, 5239–5251 (1986).

306. N. F. Mott, *Metal-insulator transitions* (Taylor & Francis, London, 2nd), p. 286.

307. S. Borroni *et al.*, *Phys. Rev. B* **98**, 184301 (2018).

308. L. V. Gasparov *et al.*, *Phys. Rev. B* **62**, 7939–7944 (2000).

309. I. Leonov, A. N. Yaresko, V. N. Antonov, V. I. Anisimov, *Phys. Rev. B* **74**, 165117 (2006).

310. H.-T. Jeng, G. Y. Guo, D. J. Huang, *Phys. Rev. B* **74**, 195115 (2006).

311. H. Liu, C. Di Valentin, *J. Phys. Chem. C* **121**, 25736–25742 (2017).

312. A. Schlegel, S. F. Alvarado, P. Wachter, *J. Phys. C Solid State Phys.* **12**, 1157–1164 (1979).

313. L. Degiorgi, P. Wachter, D. Ihle, *Phys. Rev. B* **35**, 9259–9264 (1987).

314. A. Chainani, T. Yokoya, T. Morimoto, T. Takahashi, S. Todo, *Phys. Rev. B* **51**, 17976–17979 (1995).

315. J.-H. Park, L. H. Tjeng, J. W. Allen, P. Metcalf, C. T. Chen, *Phys. Rev. B* **55**, 12813–12817 (1997).

316. S. K. Park, T. Ishikawa, Y. Tokura, *Phys. Rev. B* **58**, 3717–3720 (1998).

317. P. Poddar, T. Fried, G. Markovich, *Phys. Rev. B* **65**, 172405 (2002).

318. P. Poddar *et al.*, *Europhys. Lett.* **64**, 98–103 (2003).

319. D. Schrupp *et al.*, *Europhys. Lett.* **70**, 789–795 (2005).

320. K. Jordan *et al.*, *Phys. Rev. B* **74**, 085416 (2006).

321. S. Lee *et al.*, *Nat. Mater.* **7**, 130–133 (2008).

322. A. A. Fursina, R. G. S. Sofin, I. V. Shvets, D. Natelson, *Phys. Rev. B* **79**, 245131 (2009).

323. Q. Yu *et al.*, *Phys. Rev. B* **90**, 075122 (2014).

324. A. Hevroni, M. Bapna, S. Piotrowski, S. A. Majetich, G. Markovich, *J. Phys. Chem. Lett.* **7**, 1661–1666 (2016).

325. H. Y. Huang *et al.*, *Nat. Commun.* **8**, 15929 (2017).

326. R. Rakshit *et al.*, *Nano Lett.* **19**, 5003–5010 (2019).

327. A. Banerjee, A. J. Pal, *J. Phys. Condens. Matter* **32**, 055701 (2020).

328. L. Degiorgi, I. Blatter-Mörke, P. Wachter, *Phys. Rev. B* **35**, 5421–5424 (1987).

329. A. Yanase, N. Hamada, *J. Phys. Soc. Japan* **68**, 1607–1613 (1999).

330. A. S. Alexandrov, J. Ranninger, *Phys. Rev. B* **45**, 13109–13112 (1992).

331. E. P. A. M. Bakkers, D. Vanmaekelbergh, *Phys. Rev. B* **62**, R7743–R7746 (2000).

332. E. P. A. M. Bakkers *et al.*, *Nano Lett.* **1**, 551–556 (2001).

333. D. Katz, O. Millo, S.-H. Kan, U. Banin, *Appl. Phys. Lett.* **79**, 117–119 (2001).

334. U. Lundin, R. H. McKenzie, *Phys. Rev. B* **66**, 075303 (2002).

335. W. W. Yu, J. C. Falkner, C. T. Yavuz, V. L. Colvin, *Chem. Commun.*, 2306 (2004).

336. K. Wu *et al.*, *ACS Omega* **6**, 6274–6283 (2021).

337. R. Frison *et al.*, *Chem. Mater.* **25**, 4820–4827 (2013).

338. A. Mitra, J. Mohapatra, S. S. Meena, C. V. Tomy, M. Aslam, *J. Phys. Chem. C* **118**, 19356–19362 (2014).

339. F. Schrettle, S. Krohns, P. Lunkenheimer, V. A. M. Brabers, A. Loidl, *Phys. Rev. B* **83**, 195109 (2011).

340. Z. Wang *et al.*, *Nat. Rev. Mater.* **5**, 173–195 (2020).

341. Z. Kovács-Krausz *et al.*, *Nano Letters* **20**, PMID: 32511931, 4782–4791 (2020).

342. J. Lee, S. G. Kwon, J.-G. Park, T. Hyeon, *Nano Lett.* **15**, 4337–4342 (2015).

343. S. K. Piotrowski, M. F. Matty, S. A. Majetich, *IEEE Trans. Magn.* **50**, 2303704 (2014).

344. C.-R. Lin, R.-K. Chiang, J.-S. Wang, T.-W. Sung, *J. Appl. Phys.* **99**, 08N710 (2006).

345. G. V. Williams, T. Prakash, J. Kennedy, S. V. Chong, S. Rubanov, *J. Magn. Magn. Mater.* **460**, 229–233 (2018).

346. J. Balakrishnan *et al.*, *Nat. Commun.* **5**, 4748 (2014).

347. C. K. Safeer *et al.*, *Nano Lett.* **19**, 1074–1082 (2019).

348. E. Tirosh, B. Tsukerman, N. Taub, S. A. Majetich, G. Markovich, *Phys. Rev. B* **80**, 224427 (2009).

349. S. Usmani *et al.*, *Phys. Rev. B* **98**, 104433 (2018).

350. A. Mitra, J. Mohapatra, H. Sharma, S. S. Meena, M. Aslam, *J. Phys. D. Appl. Phys.* **51**, 085002 (2018).

351. S. Jang, W. Kong, H. Zeng, *Phys. Rev. B* **76**, 212403 (2007).

352. I. Austin, N. Mott, *Adv. Phys.* **18**, 41–102 (1969).

353. A. L. Efros, B. I. Shklovskii, *J. Phys. C Solid State Phys.* **8**, L49–L51 (1975).

354. N. F. Mott, *Philos. Mag. B* **42**, 327–335 (1980).

355. A. Bhargava *et al.*, *Adv. Mater.* **32**, 2004490 (2020).

356. W. Khan, A. H. Naqvi, M. Gupta, S. Husain, R. Kumar, *J. Chem. Phys.* **135**, 054501 (2011).

357. M. Newville, T. Stensitzki, D. B. Allen, A. Ingargiola, *LMFIT: Non-Linear Least-Square Minimization and Curve-Fitting for Python*, version 0.8.0, 2014.